Determination of the Tau Pair Production Cross Section $\sigma(e^+e^- \to \tau^+\tau^-)$ at the Z^0 Resonance

THE UNIVERSITY
of MANCHESTER

High Energy Physics Group
Department of Physics and Astronomy

Robert J. Akers

July 1995

A thesis submitted to The University of Manchester for the degree of Doctor of Philosophy in the Faculty of Science and Engineering.

For my Mom,

for all her love and support when it was needed most.

Contents

List of Figures

List of Tables

"Well, I mean, YES idealism, YES the dignity of pure research, YES the pursuit of truth in all its forms, but there comes a point I'm afraid where you begin to suspect that if there's a REAL truth, it's that the entire multi-dimensional infinity of the Universe is almost certainly being run by a bunch of maniacs. And if it comes to a choice between spending yet another 10 million years finding that out, and on the other hand just taking the money and running, then I for one could do with the exercise."

Douglas Adams, HHGG

"While I'm still confused and uncertain, it's on a much higher plane, d'you see, and at least I know I'm bewildered about the really fundamental and important facts of the universe." Treatle nodded. "I hadn't looked at it like that," he said, "But you're absolutely right. He's really pushed back the boundaries of ignorance."

Terry Pratchett, Equal Rites

"I would like to live in Manchester, England. The transition between Manchester and death would be unnoticeable."

Mark Twain

Abstract

We present a measurement of the cross section for the process $e^+e^- \rightarrow \tau^+\tau^-$ at energies on and around the Z^0 resonance using data collected by the OPAL detector at the LEP collider in the years 1992 and 1993. Careful studies of the event selection cuts, Monte Carlo background simulation and cosmic ray background were carried out in order to produce a well understood precision result. The 1992 peak data at an energy of 91.299 ± 0.018 GeV produced a cross section of 1.479 ± 0.009(stat) $\pm$ 0.011(syst), the 1993 pre-scan data at an energy of (91.319 ± 0.005) GeV produced a cross section of 1.483 ± 0.021(stat) $\pm$ 0.007(syst) $\pm$ 0.009(lumi syst) and the 1993 scan-peak data at an energy of (91.208 ± 0.005) GeV produced a cross section of 1.480 ± 0.018(stat) $\pm$ 0.008(syst) $\pm$ 0.003(lumi syst). The ± 2 GeV data sets in 1993 produced cross sections of 0.681 ± 0.009(stat) $\pm$ 0.008(syst) $\pm$ 0.001(lumi syst) and 0.499 ± 0.006(stat) $\pm$ 0.009(syst) $\pm$ 0.001(lumi syst) for the peak+2 and peak$-$2 points respectively. All results are in agreement with the Minimal Standard Model predictions and the cross section results so far published by the other LEP experiments.

Declaration

No portion of the work referred to in this thesis has been submitted in support of an application for another degree or qualification of this or any other university or other institute of learning.

The author was educated at Oldbury Wells School, Bridgnorth, between 1980 and 1988. In 1991 he obtained a 1st class BSc.(Hons) in Physics at the University of Manchester. The work presented in this thesis was conducted at the University of Manchester and the European Centre for Particle Physics, CERN, Genève.

Chapter 1

Introduction

In this thesis we present a measurement of the taupair production cross section $\sigma(e^+e^- \to \tau^+\tau^-)$ at energies on and around the Z^0 resonance using data collected in the 1992 and 1993 LEP running periods utilising the OPAL detector. Chapter 2 gives a brief overview of the Minimal Standard Model, paying particular attention to the Electroweak sector. Chapter 3 briefly describes the tau lepton and outlines how the mechanics of the Minimal Standard Model outlined in Chapter 2 are exploited in order to calculate a theoretical prediction for the taupair cross section, paying particular attention to energies close to the pole. Chapter 4 briefly describes the OPAL detector and the LEP accelerator together with the OPAL trigger system, pre-trigger, filter and OPAL software suite. Chapter 5 describes the taupair pre-selection, detector and trigger status cuts, track and cluster quality cuts and the cuts used to isolate taupair events from other final states. A brief description of the luminosity determination and LEP energy calibration is also given. Chapter 6 is concerned with the choice of Monte Carlo tau branching ratios and how they affect the measurement. Chapter 7 describes the application of photon conversion and split track joining algorithms used to reduce the final selection cut systematic error. Chapter 8 briefly describes a multitude of systematic enhancement checks used to examine the Monte Carlo simulation of signal and background and Chapter 9 describes the determination of the cosmic ray and beam gas background. Chapter 10 summarises the 1992 and 1993 measurements together with the improvements that can be made by combining event samples.

Chapter 2

The Standard Model

The Standard Model [1] attempts to describe the interactions between the three known families of matter particles comprising the quarks and leptons, these being shown in table 2.1 listed horizontally in generations. All particles have been experimentally observed with the exception of the tau neutrino, experimental evidence for the top quark recently having been released by CDF [2] and D0 [3]. In the model, all matter is composed of spin-$\frac{1}{2}$ point-like fermions, the 'fermionic matter fields' and the interactions between them take place via the propagation of spin-1 gauge bosons, the 'gauge fields'. The Standard Model is a relativistic quantum field theory based upon a series of 'local gauge symmetries', comprising Quantum Chromodynamics (QCD) [4] and 'Electroweak Theory' [5][6][7][8][9]. QCD is the sector which justifies the existence of three quark hadronic 'baryon' states such as the proton and two quark 'meson' states such as the pion. It also introduces 8 massless gluon fields and predicts such effects as 'quark confinement'. Electroweak Theory combines Quantum Electrodynamics (QED) with the 'weak' interaction responsible for nuclear β-decay and generates the charged $W^{\pm}$ gauge bosons and the neutral Z^0 and photon fields. By the introduction of the 'Higgs field' [1], the $W^{\pm}$ and Z^0 bosons acquire mass and the photon remains massless in a way that does not destroy the gauge symmetry and renormalizability of the model. Indeed, the Higgs particle is necessary to guarantee the renormalizability of the theory even if it is not introduced to generate the heavy gauge boson masses [10]. As yet there is no direct evidence for the existence of the

Higgs [11] but this in no way limits the predictive power of the Standard Model. No attempt is made in the Minimal Standard Model (MSM) to include the effects of gravity due to its extremely small coupling. Even attempts to embed the Standard Model symmetry group inside a larger single group (grand unification [12]) can be made without taking the gravitational force into account.

2.1 Quantum Electrodynamics

Quantum Electrodynamics (QED) [13] is the quantum field theory that describes the electromagnetic interaction between charged particles. The premise of 'local gauge invariance' of the QED Lagrangian under unitary phase transformations necessitates the introduction of a vector field (the photon). The addition of mass terms to the Lagrangian breaks the $U(1)$ symmetry, hence the photon must be massless.

Name	Spin[1]	Baryon Number B	Lepton Number[2] L	Charge Q
Quarks				
u c t	$\frac{1}{2}$	$\frac{1}{3}$	0	$\frac{2}{3}$
d s b	$\frac{1}{2}$	$\frac{1}{3}$	0	$-\frac{1}{3}$
Leptons				
e μ τ	$\frac{1}{2}$	0	1	-1
ν_e ν_μ ν_τ	$\frac{1}{2}$	0	1	0
Gauge bosons				
γ	1	0	0	0
$W^{\pm}$,Z^0	1	0	0	$\pm$1,0
$g_i(i=1,\cdots,8)$	1	0	0	0

Table 2.1: *The elementary matter and gauge particles of the Standard Model. For the matter fields, their corresponding antiparticles are not listed - these have B, L and Q quantum numbers of opposite sign.*

[1]Spin is given in units of $\hbar$.

[2]There is a separate lepton number for each generation ie. the electron number, muon number and tau number.

2.2 Electroweak Theory

The weak force was first postulated in 1935 by Fermi [14] to explain the phenomenology of β-decay. He suggested the existence of a four fermion pointlike interaction of coupling strength G_F which proved to be satisfactory for first order calculations and $q^2 \ll (100\,\mathrm{GeV})^2$. It was the combined effort of Glashow, Salam and Weinberg [5][6][7][8][9] however that provided us with a respectable (ie. renormalizable) theory capable of describing the high energy regime. It is centred around the existence of massive gauge bosons ($W^{\pm}$,Z^0) and the discovery of 'spontaneously broken non-Abelian gauge symmetries'.

The first step is to attempt to form a symmetry group of weak interactions (that is the charged and neutral weak currents) in the same way that the electromagnetic interaction obeys a $U(1)$ local gauge symmetry. The charged weak currents are observed to have a $V-A$ structure, that is they must be constructed from vector and axial-vector bilinear covariants in the form:

$$\begin{aligned} j_\mu^+ &= \overline{\psi}_{\nu_e}\gamma_\mu\frac{1}{2}\left(1-\gamma^5\right)\psi_{e^-}, \\ j_\mu^- &= \overline{\psi}_{e^-}\gamma_\mu\frac{1}{2}\left(1-\gamma^5\right)\psi_{\nu_e}. \end{aligned}$$

This means that the charged weak currents are purely left handed (maximal violation of parity). The observed weak-neutral current however must have a right as well as a left handed component, seemingly destroying all hope of finding an appropriate symmetry group. The observation however that the electromagnetic current contains right as well as left handed components provides us with a way in which to introduce a weak interaction symmetry group.

For the weak current interaction we use the group $SU(2)_L$ where the L is used to indicate the fact that only left handed particles couple to the weak fields. The generators of the $SU(2)_L$ group are the 'weak isospin' generators which obey the $SU(2)$ group algebra:

$$\left[T^i, T^j\right] = i\epsilon_{ijk}T^k.$$

The Standard Model fermionic matter fields thus consist of left handed isospin doublets and right handed isospin singlets (see table 2.2).

The combined 'electroweak' symmetry group is given by $SU(2)_L \otimes U(1)_Y$. Y, the 'weak hypercharge' is defined by the Gell-Mann-Nishijima relation:

$$Q = T^3 + \frac{Y}{2}$$

where Q (the charge operator) is the generator of the $U(1)_{em}$ symmetry group, T^3 is the third weak isospin generator and Y is the generator of the symmetry group $U(1)_Y$. Forcing the Lagrangian to be locally gauge invariant creates an isotriplet of vector fields $W^i (i = 1, 2, 3)$ which obey the $SU(2)_L$ group algebra and a B^0 isosinglet vector particle. Terms appear in the Lagrangian which describe the interactions between fermions and the boson fields, the kinetic energy of the B_μ and W_μ fields and the W_μ field self interaction due to the non-Abelian nature of the $SU(2)$ group. Since we have a product of symmetry groups, the generator Y must commute with the generators T^i, the consequence of which being that members of an isospin multiplet must have the same value of weak hypercharge. Table 2.2 shows the weak isospin and weak hypercharge assignments for the first generation of Standard Model isospin multiplets, second and third generations having the same structure.

Lepton	T	T^3	Q	Y
ν_e	$\frac{1}{2}$	$\frac{1}{2}$	0	-1
e^-_L	$\frac{1}{2}$	$-\frac{1}{2}$	-1	-1
e^-_R	0	0	-1	-2

Quark	T	T^3	Q	Y
u_L	$\frac{1}{2}$	$\frac{1}{2}$	$\frac{2}{3}$	$\frac{1}{3}$
d_L	$\frac{1}{2}$	$-\frac{1}{2}$	$-\frac{1}{3}$	$\frac{1}{3}$
u_R	0	0	$\frac{2}{3}$	$\frac{4}{3}$
d_R	0	0	$-\frac{1}{3}$	$-\frac{2}{3}$

Table 2.2: *Weak isospin and weak hypercharge quantum numbers of the first generation of leptons and quarks.*

The massless ν_e and the left handed electron can be seen to form the upper and lower member of a $T=\frac{1}{2}$ doublet whereas the e_R^- is an isospin singlet. Similarly u and d quarks form a doublet, the difference this time being that we introduce a right handed u_R singlet due to the u-quark's finite mass. Care should be taken here however as the quark weak isospin eigenstates listed in table 2.2 are not the quark 'mass eigenstates' but instead mixtures of them, this mixing being described by the 'CKM Mechanism' [15]. This introduces flavour changing charged currents between generations.

By forming two orthogonal combinations of the electromagnetic and weak-neutral currents we have formed two new currents; one combination completes the weak isospin triplet and the other 'hypercharge current' forms an isospin singlet which remains unchanged by $SU(2)_L$ transformations - in a sense we have 'unified' the weak and electromagnetic sectors, however rather than a single unified symmetry group, we have two groups, each with an independent coupling strength. The basic electroweak interaction is therefore:

$$-ig(j^i)^\mu W_\mu^i - i\frac{g'}{2}(j^Y)^\mu B_\mu \tag{2.1}$$

ie. the isotriplet vector fields are coupled to the weak isospin current with strength g and the isosinglet vector field is coupled to the weak hypercharge current with strength conventionally taken as $g'/2$. The charged weak $W^\pm$ fields are related to the W_μ^i fields by:

$$W_\mu^\pm = \sqrt{\frac{1}{2}}\left(W_\mu^1 \mp iW_\mu^2\right).$$

We must now extract the electromagnetic and weak-neutral currents from equation 2.1. We shall describe in section 2.3 the process by which the observable weak fields acquire mass leading to a mixing of the W_μ^3 and B_μ fields to produce the massless electromagnetic (A_μ) and massive weak-neutral (Z_μ) fields:

$$A_\mu = B_\mu \cos\theta_W + W_\mu^3 \sin\theta_W, \tag{2.2}$$

$$Z_\mu = -B_\mu \sin\theta_W + W_\mu^3 \cos\theta_W. \tag{2.3}$$

Substituting 2.2 and 2.3 into 2.1, the electroweak-neutral current interaction becomes:

$$\begin{aligned} -igj^3_\mu (W^3)^\mu - i\frac{g'}{2} j^Y_\mu B^\mu &= -i\left(g\sin\theta_W j^3_\mu + g'\cos\theta_W \frac{j^Y_\mu}{2}\right) A^\mu \\ &\quad -i\left(g\cos\theta_W j^3_\mu - g'\sin\theta_W \frac{j^Y_\mu}{2}\right) Z^\mu \end{aligned} \tag{2.4}$$

The first term in brackets is the electromagnetic interaction - combining this with the Gell-Mann-Nishijima form of the electromagnetic current ie.

$$ej^{em}_\mu \equiv e\left(j^3_\mu + \frac{1}{2} j^Y_\mu\right), \tag{2.5}$$

we find

$$g\sin\theta_W = g'\cos\theta_W = e, \tag{2.6}$$

that is we can re-express the couplings g and g' in terms of the electromagnetic coupling and the weak mixing angle θ_W. Combining the second term of 2.4 with 2.5 and 2.6 we find that the weak-neutral current interaction is given by:

$$-i\frac{g}{\cos\theta_W}\left(j^3_\mu - \sin^2\theta_W j^{em}_\mu\right) Z^\mu \equiv -i\frac{g}{\cos\theta_W} j^{NC}_\mu Z^\mu$$

where we have defined the weak-neutral current to be:

$$j^{NC}_\mu \equiv j^3_\mu - \sin^2\theta_W j^{em}_\mu.$$

Inserting the $V-A$ form of j^3_μ and the electromagnetic current j^{em}_μ gives:

$$\begin{aligned} -i\frac{g}{\cos\theta_W}\left(j^3_\mu - \sin^2\theta_W j^{em}_\mu\right) Z^\mu &= \\ -i\frac{g}{\cos\theta_W}\overline{\psi}_f \gamma^\mu \left[\frac{1}{2}\left(1-\gamma^5\right) T^3 - \sin^2\theta_W Q\right]\psi_f Z_\mu. \end{aligned}$$

It is conventional to group the vector and axial-vector terms together and to define vector and axial-vector couplings c_V and c_A such that the weak-neutral current vertex factor is written:

$$-i\frac{g}{\cos\theta_W}\gamma^\mu \frac{1}{2}\left(c^f_V - c^f_A \gamma^5\right)$$

and

$$c_V^f = T_f^3 \quad -2\sin^2\theta_W Q_f,$$
$$c_A^f = T_f^3.$$

The vector and axial-vector couplings for the 'Minimal' Standard Model (MSM) fermionic matter particles are now completely specified and shown in table 2.3.

f	Q_f	c_A^f	c_V^f
ν_e,ν_μ,ν_τ	0	$\frac{1}{2}$	$\frac{1}{2}$
e^-,μ^-,τ^-	-1	$-\frac{1}{2}$	$-\frac{1}{2}+2\sin^2\theta_W$
u,c,t	$\frac{2}{3}$	$\frac{1}{2}$	$\frac{1}{2}-\frac{4}{3}\sin^2\theta_W$
d,s,b	$-\frac{1}{3}$	$-\frac{1}{2}$	$-\frac{1}{2}+\frac{2}{3}\sin^2\theta_W$

Table 2.3: *Charge, axial-vector and vector couplings of the MSM matter particles.*

The vertex factors for the electromagnetic, charged-weak and neutral-weak currents are summarised in figure 2.1.

In the next section we shall discuss the proposed mechanism by which the $W^\pm$ and Z^0 gauge fields obtain mass whilst leaving the photon massless and defining the mixing in equations 2.2 and 2.3.

2.3 The Higgs Mechanism

So far, we have constructed a theory which contains two charged $W^\pm$ vector gauge bosons, a neutral Z^0 gauge boson and the QED photon, all of which are so far massless. To ensure the short range force of the $W^\pm$ in order to model nuclear β-decay we must somehow introduce masses for the $W^\pm$ and Z^0 whilst leaving the photon massless. Simply adding mass terms to the Lagrangian breaks the group symmetry and renormalizability of the model, obliterating its predictive power. Instead, it is proposed that mass is introduced by the process of 'spontaneous symmetry breaking'.

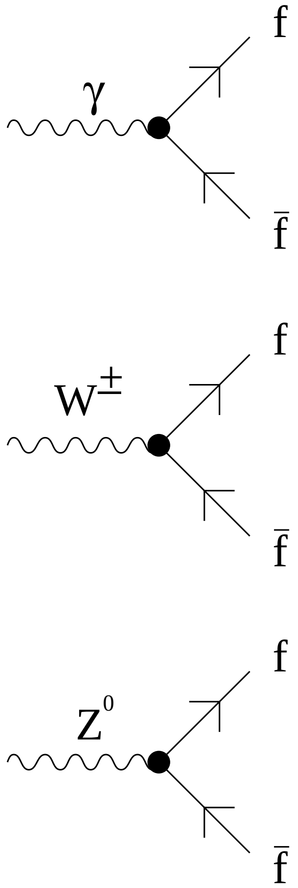

$$ie\gamma^{\mu}$$
(charge $-e$)

$$-i\frac{g}{\sqrt{2}}\gamma^{\mu}\frac{1}{2}\left(1-\gamma^{5}\right)$$

$$-\frac{ig}{\cos\theta_W}\gamma^{\mu}\frac{1}{2}\left(c_V^f - c_A^f\gamma^{5}\right)$$

Figure 2.1: *The vertex factors of the Standard Model Electroweak sector, namely the QED photon vertex and the charged and neutral weak current vertices.*

We add to the Lagrangian:

$$\mathcal{L}_{\mathrm{HIGGS}} = \left|\left(i\partial_\mu - gT.W_\mu - g'\frac{Y}{2}B_\mu\right)\phi\right|^2 - V\left(\phi\right)$$

where the ϕ_i belong to $SU(2)\otimes U(1)$ multiplets. The simplest choice is to arrange the fields in an isospin doublet of weak hypercharge $Y=1$:

$$\phi = \begin{pmatrix} \phi^{+} \\ \phi^{0} \end{pmatrix}$$

with

$$\begin{aligned}\phi^+ &\equiv (\phi_1 + i\phi_2)/\sqrt{2}, \\ \phi^0 &\equiv (\phi_3 + i\phi_4)/\sqrt{2}.\end{aligned}$$

This is the choice proposed by Weinberg in 1967 and completes the Minimal Standard Model of electroweak interactions.

To generate masses for the $W^\pm$ and Z^0, we introduce the 'Higgs potential' $V(\phi)$:

$$V(\phi) = \mu^2\phi^\dagger\phi + \lambda(\phi^\dagger\phi)^2$$

and choose $\mu^2 < 0$ and $\lambda > 0$. We then introduce a 'non zero vacuum expectation value' ϕ_0:

$$\phi_0 = \sqrt{\frac{1}{2}}\begin{pmatrix} 0 \\ v \end{pmatrix}.$$

ie. we have chosen a ground state where:

$$\phi_1 = \phi_2 = \phi_4 = 0, \quad \phi_3^2 = -\tfrac{\mu^2}{\lambda} \equiv v^2,$$

thus 'breaking' the symmetry of the Lagrangian. Vacuum fluctuations have to be calculated using perturbation theory around this minimum rather than the unstable zero point, these fluctuations creating three massless 'Goldstone bosons' which get re-interpreted as terms in the Lagrangian which describe the longitudinal polarizations of the now massive gauge fields. Terms also now appear corresponding to the masses of the gauge bosons, the mass of the single neutral 'Higgs boson' and interaction terms. The masses of the charged $W_\mu^\pm$, the neutral Z_μ and the neutral photon A_μ fields are given by:

$$\begin{aligned}M_W &= \tfrac{1}{2}vg, \\ M_Z &= \tfrac{1}{2}v\sqrt{g^2 + g'^2}, \\ M_A &= 0\end{aligned}$$

and by re-writing the couplings in the form

$$\frac{g'}{g} = \tan\theta_W,$$

we arrive at the equations for the Z_μ and A_μ fields (equations 2.2 and 2.3) in terms of the weak mixing angle and the W^3_μ and B_μ $SU(2)_L \otimes U(1)_Y$ gauge invariant fields. We can see therefore that the weak mixing angle not only relates the electroweak couplings, but also the ratio of the $W^\pm$ and Z^0 masses:

$$\frac{M_W}{M_Z} = \cos\theta_W,$$

a prediction which can be tested. The same Higgs model also provides masses for the lepton and quark matter fields. Unfortunately, the masses are free parameters and similarly, the mass of the Higgs itself is not predicted. The model does predict however that the Higgs will couple to the matter fields proportionally to their mass, a prediction which can be tested if and when the Higgs is discovered. The fact that the most readily experimentally accessible particles are the light fermions (with the exception of the Z^0 of course) has meant that up until now, the Higgs has eluded detection [11]. The discovery of the Higgs thus remains an important experimental goal.

2.4 Quantum Chromodynamics

The Standard Model is completed by expanding the interaction symmetry group to $SU(3) \otimes SU(2)_L \otimes U(1)_Y$ where the SU(3) group is used to generate the 8 gluon fields and explains such phenomena as 'confinement'. The interested reader is directed towards such texts as [1],[4] and [16].

Chapter 3

τ-pair Production

3.1 e^+e^- annihilation

In order to test the predictions of the MSM, it is necessary to choose suitable measurable observables which are strongly dependent upon the MSM parameters. This thesis is concerned with measurement of the taupair production ($e^+e^- \rightarrow \tau^+\tau^-$) cross section σ_τ at the Z^0 resonance using the OPAL experiment at LEP, a measurement which when combined with the other LEP observables yields the vector and axial-vector couplings of the τ and other leptons and thus tests of lepton universality and the predictions given in table 2.3. Performing the combined multi-parameter fit is in itself a highly complex analysis, requiring careful consideration of the correlations between parameters introduced by such things as the LEP beam energy calibration and the luminosity measurement. The main aim of this thesis is to provide an accurate value of σ_τ to be used by the OPAL [17] and LEP [18] combined fit and to provide greater insight into the OPAL taupair signal. We shall discuss some aspects of tau physics which have relevance to the measurement of σ_τ and briefly outline the theoretical prediction of σ_τ.

e^+e^- colliders are ideally suited to probing the electroweak interaction. The initial state is very clean with pointlike particles (experimentally $r < 10^{-18}$m) and the initial state particles completely annihilate. All fermion pairs with $m_f < \frac{E_{\rm CM}}{2}$ are produced in the final state allowing tests of lepton universality and at LEP, where

$E_{\rm CM} \approx M_Z$, taupairs are produced in large numbers due to the Z^0 resonance thus providing the high statistics suitable for precision measurements. The fact that γ and Z^0 exchange diagrams interfere also provides us with interesting, testable predictions.

3.2 Properties of the τ lepton and its decays

The τ lepton was discovered between the years 1975-1978 [19] using the SPEAR storage ring at SLAC and the DORIS ring at DESY during which time its leptonic nature was confirmed. The τ lepton has a mass of $1777.1^{+0.4}_{-0.5}$ MeV [20] and thus can readily undergo weak decay through a large number of modes, the more dominant of these being listed in table 6.1. This makes the τ lepton an ideal testing ground for weak interaction decay theory [21], precision measurements of the τ branching ratios determined at LEP [22] showing strong agreement with the charged current $V-A$ structure of the Minimal Standard Model.

Due to the fact that τ decays are accompanied by neutrinos, one of the most notable signatures of a taupair event is that of missing energy. The decay track multiplicity of a τ lepton is either 1, 3 or 5 in the absence of photon conversions, thus providing a means by which final states containing quark pairs can be separated. Jets in a taupair event at LEP are almost back-to-back due to the large boost provided by the 45 GeV beam energy, a degree of acolinearity[1] being introduced however by initial state radiation or by the missing energy.

The τ lepton can decay leptonically into either an electron or muon or, because it is sufficiently massive, it can decay into hadronic final states providing a means by which the strong coupling constant α_s can be measured. It is these hadronic states that provide the decays with track multiplicity in excess of one.

The average polarisation of the final state taupairs has a geometrical behavior defined by the MSM, this being revealed in the momentum distributions of the decay particles thus providing further tests of the MSM. The interested reader is directed towards [23] for further reading.

[1]acolinearity = 180° minus the angle between the two jet axes.

3.2.1 τ-pair production in e^+e^- annihilation

Taupair events ($e^+e^- \rightarrow \tau^+\tau^-$) are produced in e^+e^- colliders by the 1st order annihilation (s-channel) processes shown in figure 3.1.

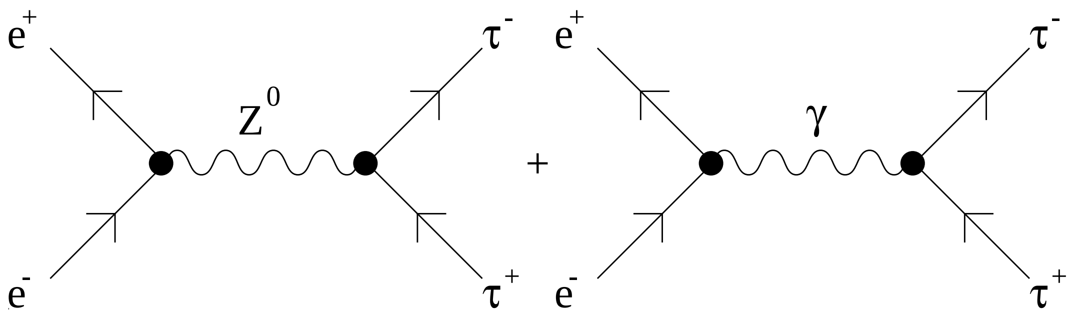

Figure 3.1: *First order diagrams for the production of taupair events in an e^+e^- collision.*

All considerations here will be restricted to the case where both initial state particles have equal and opposite momenta (the laboratory frame is the barycentric frame) and are unpolarised. The appropriate form of the differential cross section is given by:

$$\frac{d\sigma_\tau}{d\Omega} = \frac{\alpha^2(\hbar c)^2}{4s}\left(f_{\gamma\gamma} + f_{\gamma Z} + f_{ZZ}\right) \tag{3.1}$$

where $f_{\gamma\gamma}$ is the pure photon exchange term, f_{ZZ} is the pure Z^0 exchange term and $f_{\gamma Z}$ is the $\gamma - Z^0$ interference term. We shall now discuss the behavior of the taupair production cross section with centre of mass energy and pay particular attention to the behavior around the Z^0 resonance.

3.2.2 From threshold to 10 GeV

For centre of mass energies below 10 GeV, the direct Z^0 and $\gamma - Z^0$ interference terms of equation 3.1 can be neglected. The differential cross section for a spin-$\frac{1}{2}$ tau particle to first order due to direct photon exchange is then given by:

$$\frac{d\sigma_\tau}{d\Omega} = \frac{\alpha^2(\hbar c)^2}{4s}\beta(2-\beta^2\sin^2\theta) \tag{3.2}$$

and the total cross section by:

$$\sigma_\tau = \frac{4\pi\alpha^2(\hbar c)^2\beta}{3s}.\frac{(3-\beta^2)}{2} \tag{3.3}$$

where β is the speed of the final state particles divided by c and θ is the angle between the final state particles and the beam axis. Equation 3.3 should be modified at threshold [24] by a multiplicative factor:

$$F_c = \frac{\pi\alpha/\beta}{1-\exp(-\pi\alpha/\beta)}$$

to account for the attractive coulomb force between the τ^+ and the τ^-. This means that rather than σ_τ being zero at threshold where $s = 4m_\tau^2$ and $\beta = 0$, the threshold cross section in the absence of radiative corrections is given by:

$$\frac{\pi^2\alpha^3(\hbar c)^2}{2m_\tau^2} = 0.23\,\text{nb} .$$

A general discussion of the higher order corrections that need to be applied to equations 3.2 and 3.3 in order to perform precise comparison of measurement and theory in the low energy regime of taupair production is given in [25] and [26]. Study of the behavior of the taupair production cross section at threshold has resulted in precise measurements of the τ lepton mass and confirmation of its fermionic nature. Figure 3.2 shows the rise in the total taupair production cross section from approximately 0.23 nb at threshold to a maximum of $\sim$3.5 nb at $\sim$4.2 GeV.

3.2.3 From 10 GeV to M_Z

The energy region between 10 GeV and 70 GeV was studied in detail by experiments at the PETRA [27], PEP [28][29] and TRISTAN [30][31] e^+e^- storage rings. Here, the taupair production cross section is still dominated by direct photon exchange and hence predominantly decreases as $1/s$. As the energy increases towards the Z^0 resonance however, the $f_{\gamma Z}$ interference term starts to become observable [32]. This provided the first opportunities to study the τ–Z^0–τ vertex [33]. Various models were used to parametrise deviations from the predictions of conventional electroweak theory [34][35][36] however no such deviations were observed.

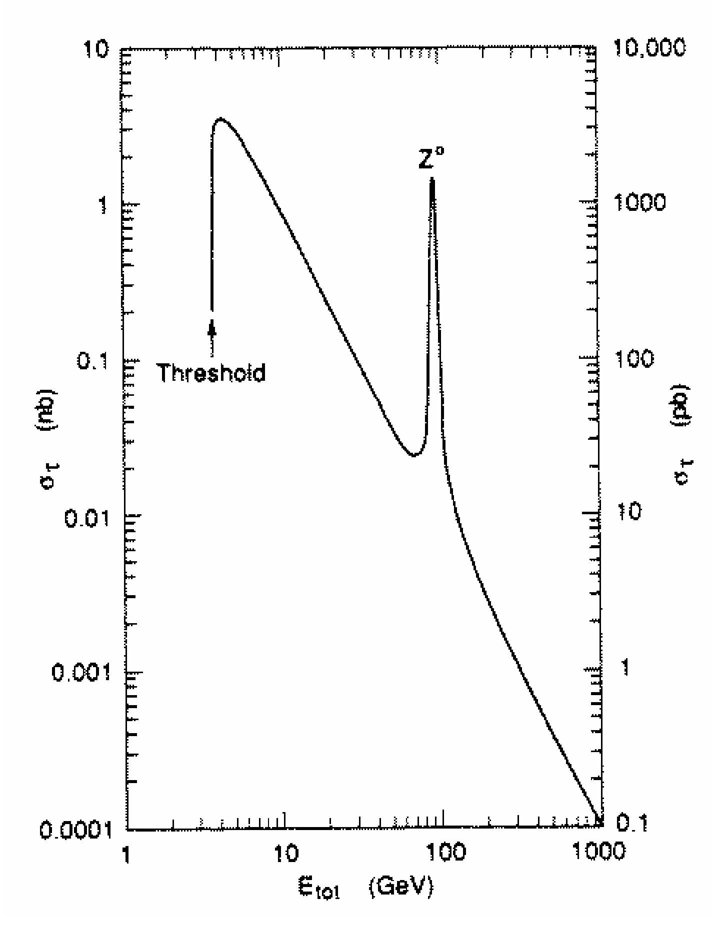

Figure 3.2: *The first order behavior of σ_τ as a function of E_{cm} from threshold to 1 TeV. Above 96 GeV, the curve is based upon conventional Electroweak theory since as yet no measurements of σ_τ above 96 GeV exist.*

3.2.4 Taupair production at the Z^0 resonance

Close to the Z^0 resonance, all three parts of equation 3.1 are important. The 1st order cross section or 'Born level' cross section is constructed using equation 3.1, the Feynman rules and the vertex factors listed in figure 2.1 with appropriate massive and massless propagator factors (see for instance [37]). The factors are given by:

$$
\begin{aligned}
f_{\gamma\gamma} &= 1+\cos^2\theta, \\
f_{\gamma Z} &= 8\left[c_V^e c_V^\tau \left(1+\cos^2\theta\right) + 2c_A^e c_A^\tau \cos\theta\right] \Re e(\chi), \\
f_{ZZ} &= 4\left[\left({c_V^e}^2+{c_A^e}^2\right)\left({c_V^\tau}^2+{c_A^\tau}^2\right)\left(1+\cos^2\theta\right) + 8c_V^e c_V^\tau c_A^e c_A^\tau \cos\theta\right] |\chi|^2 .
\end{aligned}
$$

The χ term describes the resonant shape of the cross section about the mass of the Z^0 and is given by:

$$\chi = \frac{G_F}{8\sqrt{2}\pi\alpha}\left(\frac{s{M_Z}^2}{s-{M_Z}^2+iM_Z\Gamma}\right). \tag{3.4}$$

It can be seen that in the absence of radiative corrections, the resonance is symmetric about $\sqrt{s}=M_Z$ and the $\gamma - Z^0$ interference term $f_{\gamma Z}$ vanishes at the pole. It is convenient to reparametrise the differential cross section as:

$$\frac{d\sigma}{d\Omega} = \frac{\alpha^2(\hbar c)^2}{4s}\left[A_{\rm sym}\left(1+\cos^2\theta\right) + A_{\rm asym}\cos\theta\right], \tag{3.5}$$

that is in terms symmetric and antisymmetric in $\cos\theta$:

$$A_{\rm sym} = 1 + 8c_V^e c_V^\tau \Re e\left(\chi\right) + 4\left({c_V^e}^2+{c_A^e}^2\right)\left({c_V^\tau}^2+{c_A^\tau}^2\right)|\chi|^2, \tag{3.6}$$

$$A_{\rm asym} = 16\left(c_A^e c_A^\tau \Re e\left(\chi\right) + 8c_V^e c_V^\tau c_A^e c_A^\tau |\chi|^2\right). \tag{3.7}$$

Integrating 3.5 over the full solid angle demonstrates that there is no contribution to the total cross section from the asymmetric part of the differential cross section:

$$\sigma_\tau = \frac{4\pi\alpha^2(\hbar c)^2}{3s}A_{\rm sym}.$$

At $\sqrt{s}=M_Z$, the resonance function is such that:

$$\Re e\,(\chi) \;=\; 0 \;\text{ and}$$

$$|\chi| = \frac{G_F}{2\sqrt{2}\pi\alpha}.\frac{M_Z^3}{\Gamma_Z} \approx 53.6\ . \tag{3.8}$$

The pole cross section without radiative corrections is then given by:

$$\sigma_\tau(\sqrt{s}=M_Z) = \frac{4\pi\alpha^2\,(\hbar c)^2}{3M_Z^2}\left[1+\left({c_V^e}^2+{c_A^e}^2\right)\left({c_V^\tau}^2+{c_A^\tau}^2\right)\left(\frac{G_F}{2\sqrt{2}\pi\alpha}.\frac{M_Z^3}{\Gamma_Z}\right)^2\right]. \tag{3.9}$$

Substituting equation 3.8 into equation 3.9 together with $c_A^e=-\frac{1}{2}$, $c_A^\tau=-\frac{1}{2}$ and the approximations that $c_V^e\simeq 0$ and $c_V^\tau\simeq 0$ shows the second term of equation 3.9 due to Z^0 exchange to dominate the first term due to the pointlike QED interaction by approximately 180 times. This gives a pole cross section of:

$$\sigma_\tau\left(\sqrt{s}=M_Z,\text{no rad. corr.}\right)\approx 1.9\,\text{nb}\ . \tag{3.10}$$

Further, the pole cross section can be written in terms of the Z^0 partial decay widths:

$$\sigma_\tau = \frac{12\pi}{M_Z^2}.\frac{\Gamma_{ee}\Gamma_{\tau\overline{\tau}}}{\Gamma_Z^2} \tag{3.11}$$

where:

$$\Gamma_{f\overline{f}} = \frac{G_F M_Z^3}{6\pi\sqrt{2}}\left[{c_V^f}^2+{c_A^f}^2\right] \tag{3.12}$$

for fermion species f [39] thus relating the partial widths.

3.3 Radiative corrections

Radiative corrections add to the series of amplitudes shown in figure 3.1. There are three classes, namely photonic corrections, non-photonic corrections and QCD corrections, only the first two of these being important for leptonic final states.

3.3.1 Photonic corrections

Photonic corrections are due to the addition of diagrams with real or virtual photons to the Born level diagrams of figure 3.1, some of which are shown in figure 3.3. They are large $\mathcal{O}(30\%)$ and depend upon experimental cuts, the dominant contribution coming from the first diagram ie. initial state radiation (ISR) where a real photon is radiated off the initial state, hence reducing the centre of mass energy of the collision. This seriously modifies the line-shape close to the Z^0 resonance. These corrections are taken into account by convoluting the cross section for the hard scattering process by a radiator function [23]. Theoretical accuracy is estimated to be at the level of 0.1% ie. well within the statistical and systematic uncertainty of current measurements.

3.3.2 Non-photonic corrections

Non-photonic corrections constitute the electroweak complement of the photonic corrections, some of which are shown in figure 3.4. The first diagram represents the vacuum polarization of the photon which results in an s-dependent correction to the electromagnetic coupling constant. The dominant uncertainty of $\alpha(M_Z^2)$ is due to the contribution of light quarks to the vacuum polarization of the photon [40].

The second diagram shows a similar correction for Z^0-exchange and the third a correction for $W^\pm$ exchange between final state neutrinos. A startling consequence of the broken electroweak symmetry is that unlike in QED, radiative corrections involving heavy virtual particles affect observables measured at much lower energy scales, hence providing a window with which to probe the complete particle spectrum without direct observation. Measurement of LEP observables hence allow mass limits to be placed on the top quark and the elusive Higgs boson. Non-photonic corrections require modifications to the Born description of the hard scattering process which can be handled to a very good approximation by the following:

- exchanging c_V^f and c_A^f with 'effective' vector and axial vector couplings $\hat{g}_V$ and $\hat{g}_A$ whose s-dependence is negligible in the vicinity of the peak,

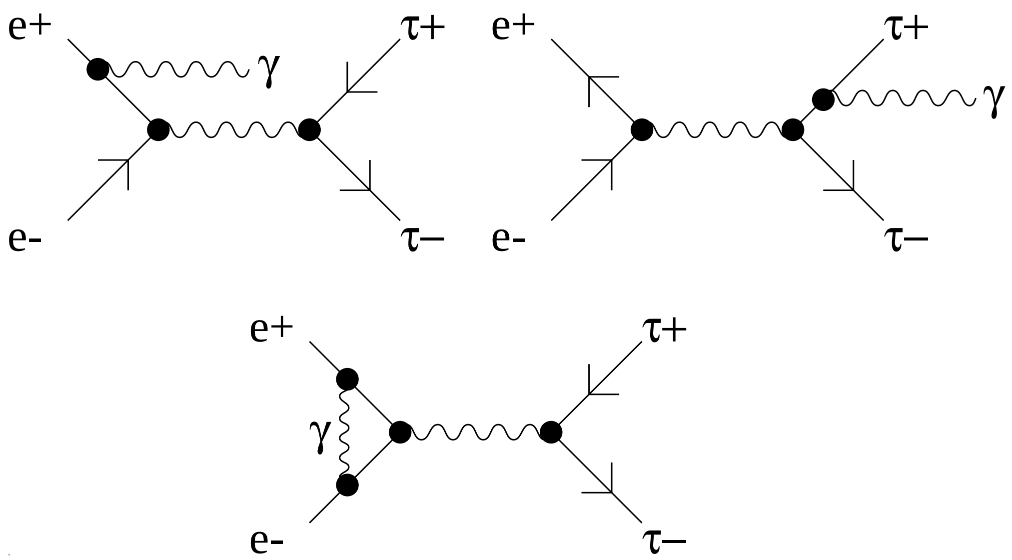

Figure 3.3: *Typical photonic corrections for the production of taupair events mediated by intermediate Z^0 or photon propagators. The first process comprises initial state radiation (ISR), the second final state radiation (FSR) and the third a vertex correction.*

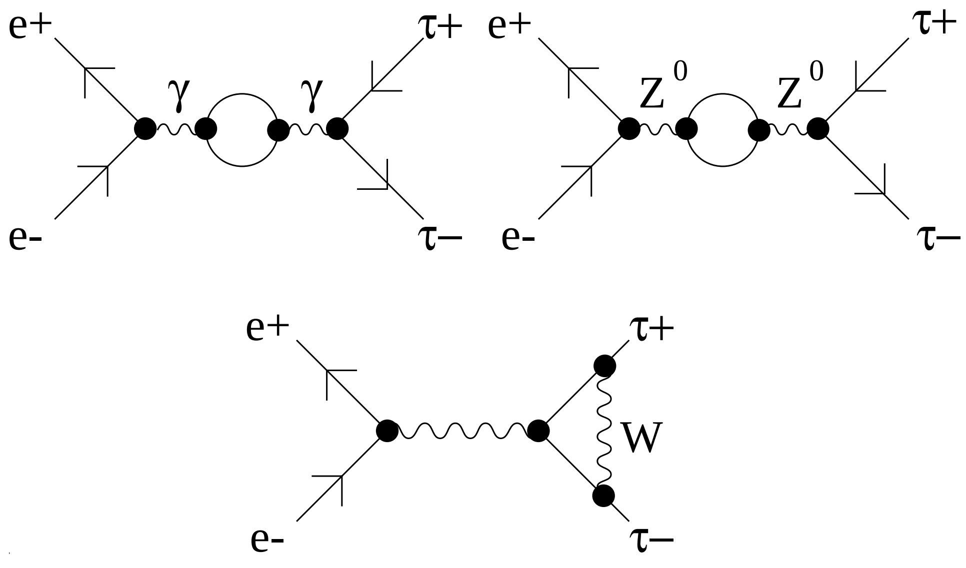

Figure 3.4: *Typical non-photonic corrections for the production of taupair events mediated by intermediate Z^0 or photon propagators. The first two represent loop corrections and the third a vertex correction.*

- an s-dependent vacuum polarization correction $\Delta\alpha(s)$ ie. choosing the electromagnetic coupling constant appropriate at the LEP energy scale and lastly
- by choosing an s-dependent Z^0 total width ie. $\Gamma \to \Gamma(s) = (s/M_Z^2).\Gamma(s = M_Z^2)$ in equation 3.4.

This is known as the 'Improved Born Approximation'. Precise calculation of the radiative corrections within the MSM to multiple orders demonstrates the difference between the full MSM calculation and the Improved Born Approximation (when appropriate values for $\hat{g}_A$ and $\hat{g}_V$ have been inserted) to be much smaller than the present experimental accuracy. The fitting procedure and extraction of $\hat{g}_V$ and $\hat{g}_A$ are standardly carried out inside the framework of ZFITTER.

3.3.3 Background channels

Background to the taupair signal occurs due to other electroweak channels having a similar energy deposition or topology to that of taupairs, predominantly in the tails of the taupair selection cut distributions. The dominant background signals are direct mupairs (two μ leptons in the final state), multihadronic events (two quarks in the final state), Bhabha events (two electrons in the final state) and two-photon events comprising muons or electrons in the final state produced by the hard scattering of two initial state virtual photons ($\gamma\gamma e^+e^-$ or $\gamma\gamma\mu^+\mu^-$). All these backgrounds are discussed in chapter 8 together with appropriate systematic checks. Further to these, a Monte Carlo determination of the 4-fermion background (predominantly four leptons in the final state) was carried out (section 8.5) and a detailed study of the cosmic ray background undertaken (chapter 9).

Chapter 4

The OPAL Detector and LEP

The Large Electron Positron (LEP) collider at CERN is a circular synchrotron [38] having a radius of approximately 26.7 Km, situated 100 m below the Franco-Swiss border. It collides electrons and positrons at four interaction points with beam spot dimensions of approximately 1.4 cm along the beam line, 100 μm radially out of LEP and 10 μm vertically at centre of mass energies on and around the Z^0 resonance. In 1992, a LEP fill consisted of four electron bunches and four counter-rotating positron bunches providing luminosities at the four interaction points such that the four LEP collaborations recorded a total of 4.7×10^6 hadronic Z^0 decays. The bunch number was doubled in 1993 with the implementation of a pretzel beam orbit mechanism [41] to increase the absolute luminosity, luminosities of $\sim1.5\times10^{31}\,\mathrm{cm}^{-2}\mathrm{s}^{-1}$ being reached for many fills. The introduction of a 'bunch train' mechanism is also hoped to double the absolute luminosity in 1995.

4.1 The Injection System and LEP

To produce the 45 GeV electron and positron bunches required to carry out precision electroweak studies, electrons are first thermionically produced and accelerated up to 200 MeV by the LEP Injector Linac (LIL). A fraction of the beam is then deflected onto a tungsten target whence it rapidly decelerates producing e^+e^- pairs. The positrons are magnetically extracted and accelerated up to 600 MeV by a second linac together with the remainder of the electron beam, and subsequently fed into the Electron Positron Accumulator (EPA). When the EPA beam luminosities have become sufficiently large, the beams are injected into the Proton Synchrotron (PS) and finally the Super Proton Synchrotron (SPS) for further acceleration up to 20 GeV. Finally, bunches are fed into LEP where they are steered by 3368 dipole bending magnets and raised to 45 GeV by LEP's niobium RF cavities which also replenish lost energy due to synchrotron radiation. The LEP beam pipe is evacuated to a pressure of less than 3×10^{-9} torr to minimise luminosity losses due to collisions with gas particles. Beam orbit corrections and focusing are carried out using LEP's 808 quadrupole and sextupole magnets, the end result being stable high luminosity bunches with an energy resolution of approximately 20 MeV and orbital lifetimes of approximately 12 hours.

4.2 The OPAL detector

OPAL [42] is one of the multipurpose composite detectors situated at each of the LEP interaction points (the other three being ALEPH [43], DELPHI [44] and L3 [45]). Its active area encloses a solid angle of almost 4π steradians and was designed to unambiguously identify all possible decay signatures occurring at the Z^0 resonance by accurately reconstructing particle momenta, decay vertices and by identifying decay particles.

OPAL's geometry can be subdivided into two sections. The 'Barrel' comprises a set of concentric cylindrical subdetectors enclosing the beam pipe, centred on the beam spot and can be separated into two 'C's to gain access to the inner subdetectors. The acceptance is completed at either end by the 'Endcap' subdetectors. The coordinate system adopted by OPAL is one of right handed cartesian coordinates with the z-axis pointing along the beam pipe in the e^- direction, the y-axis pointing approximately to the vertical[1] and the x-axis pointing approximately to the center of LEP. Spherical polar coordinates are defined by taking ϕ to be the angle between $\vec{r}$

[1] the y-axis lies at an angle to the direct vertical due to the 13.9mrad slope of the LEP ring.

and the x-axis in the x–y plane and θ to be the angle between $\vec{r}$ and the z-axis. Figure 4.1 shows an $r-\phi$ view and figure 4.2 a three dimensional exploded representation of the detector.

The central region of OPAL consists of a set of tracking chambers immersed inside a warm solenoidal magnetic field of 0.435T allowing the reconstruction of track momenta. A precision silicon microvertex detector (SI) surrounding the inner beryllium beam pipe is used to accurately deduce primary and secondary vertices, and particle momenta are determined from the track sagita resulting from fits to hit points found by the Central Vertex detector (CV), the Central Jet chamber (CJ) and a set of Z-chambers (CZ) which help to improve the momentum resolution in z. These detectors comprise the OPAL central tracking (CT) system and tracks constructed by these detectors are known as 'CT tracks'. CJ also provides a degree of particle identification by measuring the ionization loss with distance of particles. Outside CZ after the pressure vessel and magnetic coil lie a set of time of flight counters (TB), used to reject cosmic ray events as well as providing a fast trigger. Next are situated the barrel (EB) and endcap (EE) electromagnetic calorimeters (collectively known as the ECAL) which are used to detect hard photons and electrons by total absorption due to electromagnetic showering. Preceding the ECAL are electromagnetic presamplers which in theory can be used to correct ECAL cluster energy when showering has commenced prior to the ECAL. Outside the ECAL lie the barrel (HB), endcap (HE) and poletip (HP) hadron calorimeters (collectively labelled the HCAL), used to detect both neutral and charged hadronic particles by total absorption as well as acting as a return yoke for the magnetic field. Outside the HCAL are situated a set of barrel (MB) and endcap (ME) muon chambers which detect the presence of highly penetrating muons. Lastly a pair of luminosity monitors (FD/SiW) are fitted at either end of OPAL in the far forward region which measure the luminosity using the QED process of extremely low angle Bhabha scattering. There follows a brief description of each of subdetector, a short description of the OPAL trigger and data acquisition system and a brief description of the OPAL software suite.

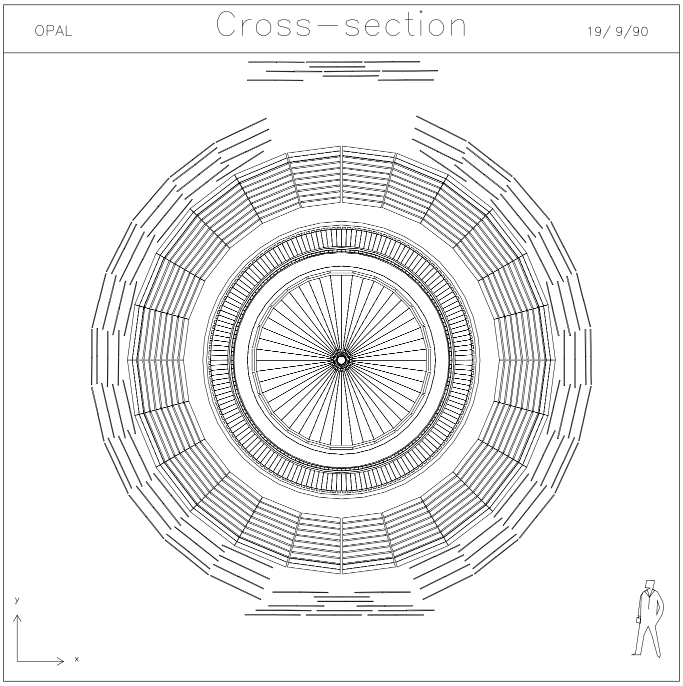

Figure 4.1: *Head-on view of the OPAL detector*

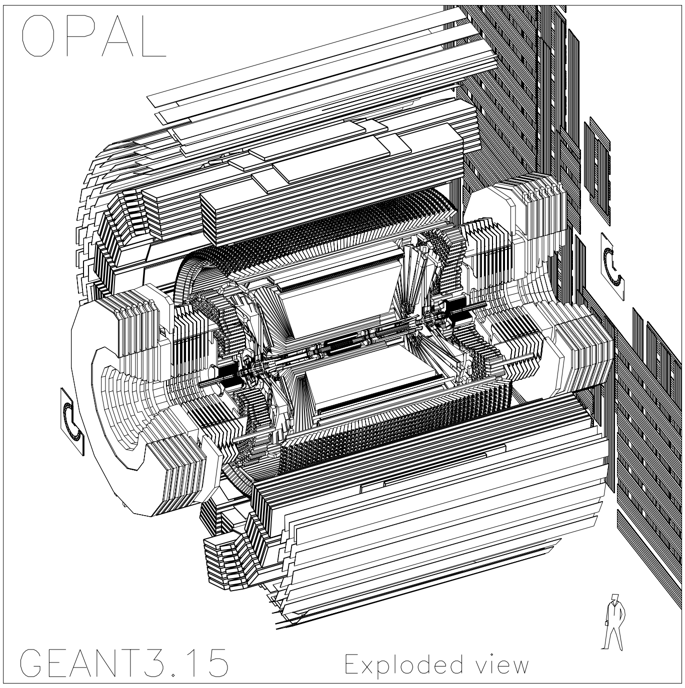

Figure 4.2: *Exploded view of the OPAL detector*

4.2.1 Central Tracking

CV,CJ and CZ all use the same gas mixture: 88.2% argon, 9.8% methane and 2.0% isobutane at a pressure of 4 bar whereas SI is housed inside an envelope of dry nitrogen at a little over atmospheric pressure. All four detectors are immersed in a warm solenoidal field of 0.435T.

The Silicon Microvertex Detector (SI) [46] is situated between the inner and outer beam pipe and comprises two cylinders of single sided microstrip detectors. The inner layer at a radius of 6 cm consists of 11 ladders and the outer radius at 7.5 cm has 14 ladders. Each ladder is 18 cm long and comprises three detectors chained together. Each detector has 629 strips of pitch 25 μm and every other strip is read out at 50 μm pitch. The positional resolution of SI has been measured to be approximately 5 μm in $r-\phi$ and 13 μm in z.

The Central Vertex detector (CV) [47] consists of a cylindrical drift chamber, 1 m long in z and 470 mm in radius surrounding the outer beam pipe. It comprises an inner layer of 36 cells, each containing 12 axial anode wires staggered by $\pm 41\,\mu$m to resolve the left right ambiguity and an outer layer of 36 stereo cells each containing 6 sense wires inclined at an angle of 4° to the beam pipe. Axial wires cover an angular range of $|\cos\theta| < 0.95$ and axial and stereo wires combined the range $|\cos\theta| < 0.92$. Axial chambers provide a spacial resolution of $\sigma_{r\phi} \approx 55\,\mu$m from the drift time and a coarse z resolution of $\sigma_z \approx 4$ cm from the time differential at the ends of the wires. Stereo wires provide a z resolution of $\sigma_z \approx 700\,\mu$m.

The Jet Chamber (CJ) [48] is situated directly after CV and consists of a cylindrical drift chamber having a length of 4 m, an inner radius of 0.5 m and an outer radius of 3.7 m. CJ comprises 24 sectors each containing 159 sense wires running parallel to z, each sector being separated by radial cathode wire planes. Left right ambiguities are resolved due to a $\pm 100\,\mu$m nominal stagger to the sense wires which increases to approximately 170 μm when CJ is at full voltage and the magnetic field turned on.

The hit point resolution in $r-\phi$ is $\sigma_{r\phi}\approx 135\,\mu$m and in z $\sigma_z\approx 6$ cm. For well measured tracks the momentum resolution of the chamber, σ_p/p^2 is $2.2\times 10^{-3}\,(\mathrm{GeV/c})^{-1}$. Limited particle identification can be achieved by measurement of the charge collected at the sense wires, thus providing a $\mathrm{d}E/\mathrm{d}x$ measurement [49].

The Z-Chambers (CZ) [42] comprise a cylinder of 24 drift chambers surrounding CJ, each 4 m long, 50 cm wide and 59 mm thick, each containing 8 cells. They cover the angular region $|\cos\theta| < 0.72$, and 94% of azimuth. Each cell contains 6 anode wires running perpendicular to the beam axis providing a z resolution of approximately 150 μm. Charge division is also used to determine ϕ with a spatial resolution of 15 mm.

4.2.2 The Time of Flight System (TB)

The time-of-flight system (TB) [42] comprises 160 scintillation counters at a radius of 2.36 m covering the angular range $|\cos\theta| < 0.82$. It is useful in providing a fast trigger and for cosmic ray rejection as described in chapter 9. The time resolution of TB has been determined to be 460 ps and the z resolution $\sigma_z \approx 5.5$ cm.

4.2.3 The Electromagnetic Calorimeter (ECAL)

The Presampler Barrel (PB) [42] consists of a 6.62 m long cylinder of radius 2.39 m surrounding the magnet return coil. It comprises 16 limited streamer mode chambers, each containing two tubes with axial anode wires and two sets of cathode strips, each 1 cm wide orientated at $\pm 45^\circ$ to the wire direction. This geometry provides a spacial resolution of approximately 2 mm for minimum ionizing particles.

The Presampler Endcap (PE) [42] covers the region $0.83 < |\cos\theta| < 0.95$ and is situated after the pressure vessel. It comprises 16 sectors, each sector containing one small chamber parallel to the $r-\phi$ plane and one large chamber inclined at 18° with respect to the $r-\phi$ plane in order to follow the shape of the pressure bell.

A resolution of 2–4 mm is obtained from the readout of groups of four wires and strips.

The Barrel Lead Glass Calorimeter (EB) [42] is a cylindrical assembly of 9440 lead glass blocks located after PB at a radius of 2.46 m in a non-pointing geometry. Each block has an absorption length of $24\,X_0$ and is approximately $10 \times 10\,\mathrm{cm}^2$ in cross section. The whole array covers the range $|\cos\theta| < 0.82$ and provides an energy resolution of $\sigma_E/E \approx 0.2\% + (6.3\%/\sqrt{E})$ where E is in units of GeV, however the material in the magnet return coil degrades this value by approximately 50% (for a particle of 6 GeV).

The Endcap Lead Glass Calorimeter (EE) [42] consists of two assemblies of 1132 lead glass blocks, each $9.2 \times 9.2\,\mathrm{cm}^2$ in cross section positioned directly after PE. EE covers the geometrical region $0.81 < |\cos\theta| < 0.98$ and provides an energy resolution of approximately $5\%/\sqrt{E}$, subject to degradation due to the amount of material preceding it.

4.2.4 The Hadron Calorimeter (HCAL)

The Barrel (HB) and Endcap (HE) Hadron Calorimeters [42] are sampling calorimeters constructed by positioning detectors between layers of the magnet return yoke. HB comprises 9 layers of chambers sandwiching 8 layers of 10 cm thick iron and provides a hadronic energy resolution of $\sigma_E/E \approx 120\%/\sqrt{E}$. Similarly HE comprises 8 layers of chambers sandwiching 7 layers of iron. Chambers consist of limited streamer devices made up of anode wires separated by 1 cm in a gas mixture of isobutane (75%) and argon (25%).

The Hadron Pole-Tip Calorimeters (HP) [42] extend the coverage of the hadron calorimeter from $|\cos\theta| = 0.91$ down to 0.99. They comprise 0.7 cm thick multiwire proportional chambers containing a gas mixture of CO_2 (55%) and n-pentane (45%) instrumented with anode wires at a spacing of 0.2 cm.

Collectively, the HCAL presents at least 4 interaction lengths of material to incident particles and covers a solid angle of $97\% \times 4\pi$ steradians.

4.2.5 The Muon Chambers

The Muon Barrel (MB) [50] consists of 110 large area drift chambers arranged in four staggered layers covering the region $|\cos\theta| < 0.7$. Chambers are 1.2 m wide, 90 mm deep and 10.4 m long except for chambers which are necessarily shorter at 8.4 m or 6 m in order to accommodate the OPAL support legs, gas supply pipes and electronics cables. Each chamber contains two drift cells with a central anode wire and is filled with a mixture of 90% argon and 10% ethane. $r-\phi$ coordinates are measured from the drift time with a resolution of 2 mm and z-coordinates from charge division and a set of diamond shaped cathode pads running along the drift plane under the anode wires. The z coordinate is measured using a three stage process. A 'coarse z' measurement is obtained from charge division on the wire, a 'medium z' measurement is found from diamond pads of wavelength 1710 mm and then a 'fine z' found using cathode pads of wavelength 171 mm. A z resolution of approximately 2 mm is obtained by combining these measurements.

The Muon Endcaps (ME) consist of two endcap detectors, each comprising eight $6 \times 6\,\mathrm{m}^2$ quadrant chambers and four $3 \times 2.5\,\mathrm{m}^2$ patch chambers. Each chamber has two layers of streamer tubes [51] along the x and y directions with cells spaced every 10 mm. The resolution of ME is between 1 mm and 3 mm depending upon the position of the readout strips .

4.2.6 The Forward Luminometers

The Forward Detector (FD) [42] consists of two highly forward detectors which detect particles between 47 mrad and 120 mrad to the beam pipe. Each comprises four separate detectors - a calorimeter, tube chambers, a gamma catcher and a far forward monitor. The forward calorimeter consists of 35 sampling layers of lead scintillator sandwich divided into a presampler of 4 radiation lengths and the main calorimeter of 20 radiation lengths. Tube chambers consist of three layers of proportional tube chambers positioned between the presampler and the main sections of the calorimeter. Their position is known to ± 0.05 cm and they can give the position of the shower centroid to ± 0.3 cm. The Gamma Gatcher is a ring of lead scintillator sandwich sections of 7 radiation lengths thickness. It completes the acceptance between the edge of EE and the start of the forward calorimeter. The Far Forward Monitor counters are small lead-scintillator modules of 20 radiation lengths thickness mounted either side of the beam pipe, 7.85 m from the intersection region. They detect electrons scattered in the range 5-10mrad that are deflected outwards by the LEP quadrupoles.

The Silicon Tungsten Luminometer (SiW) [52] was installed in 1993. It comprises two finely segmented position sensitive small angle SiW calorimeters placed just infront of the FD units. The fiducial acceptance of SiW is approximately 80 nb (about two times the multihadron cross section at the Z^0 peak and about 2.8 times that of the FD fiducial acceptance.) This fact together with the high level of calorimeter segmentation both radially and logitudinally, the systematic metrology of each detector and a stable mechanical structure have improved the OPAL luminosity determination considerably. We shall discuss this in section 10.1.2.

4.2.7 The Trigger

The central trigger processor [53] receives signals from five subdetectors, the input being mapped to a '$\theta - \phi$ matrix' (TP) of overlapping bins in order to detect spacial coincidences. A high degree of redundancy is obtained by combining the inputs from several subdetectors, the appropriate input trigger signals being listed in table 4.1. These signals are combined by the trigger map to form composite triggers which can individually trigger the process of event recording. In such a case, data are read out from the subdetectors and processed locally before being sent to the 'event builder' which concatenates the information. This 'event record' is then fed to the 'filter' [54]. The overall trigger efficiency for taupair selection has recently been studied in detail in [55] and determined to be 100% efficient to within 0.01%

Abbreviation	Trigger Description
TT	Track trigger
TO	Time of flight trigger
EM	Electromagnetic calorimeter trigger
HA	Hadron calorimeter trigger
MU	Muon trigger (barrel or endcap)
MB	Muon Barrel trigger
ME	Muon Endcap trigger
TM1,TM3	Track Multiplicity trigger of 1 or 3
MEL,MER	Muon Endcap in left or right side
MELR	Triggers in both muon endcaps
TPAABB	Trigger AA in same θ, ϕ bin as BB
TPAACL	Back-to-back AA trigger (collinear)
TOFOR	One or more TB triggers

Table 4.1: *Trigger terminology. AA and BB refer to any of the standalone triggers listed in the first seven rows of the table.*

4.2.8 The Filter

Approximately 35% of the events reaching the filter are noise, hence necessitating a set of filter cuts [54]. The filter rejects events that do not satisfy any of the following criteria:

- The sum of all electromagnetic clusters is greater than 2 GeV,
- back-to-back electromagnetic clusters exist in the barrel region, both of energy greater than 200 MeV,
- two clusters exist in opposite endcaps with energy in excess of 200 MeV,
- the highest energy recorded track has an energy in excess of 400 MeV,
- the second highest energy track has an energy in excess of 250 MeV,

- the summed tracking energy exceeds 700 MeV or
- a muon endcap segment points towards the event vertex.

The filter also performs the task of 'packing' the data and checking the trigger logic. Finally, the data are processed by the OPAL reconstruction software which is described briefly in section 4.3.

4.2.9 Pre-trigger

In 1993, '8 on 8' running necessitated the introduction of a 'pre-trigger' [56] at the trigger front end due to the decrease in the inter-bunch crossing time from $\sim$22.2 μs to $\sim$11.1 μs. The pre-trigger is essentially a simplified version of the trigger, making decisions based upon stand-alone signals and 12 ϕ bins. The maximum time it takes for a subdetector signal to reach the pre-trigger logic is $\sim$5.3 μs compared with $\sim$14.5 μs for the trigger (ie. well within the inter-bunch crossing time.)

4.3 OPAL Software

There follows a brief description of the major software packages utilised by the presented analysis.

4.3.1 ROPE

The **r**econstruction of **OP**AL **e**vents is carried out by the ROPE processor [57]. ROPE reconstructs drift times, energy deposits etc. into tracks and clusters using the **OP**AL **cal**ibration database (OPCAL) and knowledge of the detector geometry. This summary is then written to permanent storage together with the packed raw data (raw data being kept so that as knowledge of the detector and reconstruction software improves, the last stage of processing can be repeated). ROPE is also used to reaccess event information for physics analysis, the OD processor [58] (**O**PAL **D**ST[2]) providing useful access routines.

[2]DST = Data Summary Tape.

4.3.2 GOPAL

Simulated events produced by Monte Carlo generators are passed through the OPAL detector simulation program GOPAL [59] which utilises the GEANT package [60] (**G**EANT at **OPAL**). Monte Carlo events are generated in the form of sets of 4-vectors and are converted into simulated hits and energy deposits by tracking particles through the OPAL subdetectors, events then being written to tape in exactly the same format as for real data together with TREE information containing the history of the event generation.

4.3.3 LL

Taupair events are classified by cuts imposed inside the framework of the LL processor [62], these being described in chapter 5. LL is an analysis package produced by the OPAL lepton pair working groups to provides a common platform under which mupairs, taupairs and Bhabha events may be analysed in a mutually exclusive way.

Chapter 5

$e^+e^- \to \tau^+\tau^-$ Identification

The identification of taupair events is a two stage process consisting of 'preselection' and 'taupair classification'. Classification also involves a cosmic ray and beam gas veto which is discussed in chapter 9. There follows a brief description of the preselection and classification cuts used in the identification of taupair events together with detector and trigger status requirements and track and cluster quality cuts.

5.1 Event Preselection

The general 'preselection' of events is designed to reject noise events and select with 100% efficiency and a high degree of redundancy the large multiplicity of interesting events at the Z^0 resonance, with the exception of luminosity events in FD or SiW and single photon events [64] which require specialised event preselections. Events satisfy the general preselection if they satisfy any one of the following conditions:

- The event contains a track with $P_T > 0.7\,\mathrm{GeV}$, $|d_0| < 1\mathrm{cm}$, $|z_0| < 50\mathrm{cm}$ and at least 20 CT points [1],

[1] P_T is the track momentum at the beamspot transverse to the beam pipe and d_0 is the distance of closest approach of the track extrapolation to the beam spot in the $r-\phi$ plane. z_0 is the distance of closest approach in z.

- a track exists in ME which projects back to the $z = 0$ plane within 20cm of the beam spot (only endcaps containing 4 or less segments are considered),
- at least two electromagnetic clusters exist with $P_T > 6\,\mathrm{GeV}$ or
- two electromagnetic clusters exist with a back-to-back topology (acolinearity of less than 25°) one of which has a $P_T > 2\,\mathrm{GeV}$.

The first selection uses the central detector to identify events, the second condition provides a selection for mupair events independent of CT and the third and fourth selections use calorimetry to identify event signatures, thus providing a high degree of redundancy.

5.1.1 Detector Status and Trigger Status requirements

Tables 5.1 and 5.2 show the detector and trigger status requirements for various subdetectors used in the determination of the taupair cross section. Status 3 indicates that the subdetector was operating optimally, status 2 occurs when the subdetector was operating at reduced voltage, status 1 means that the subdetector was turned off and status 0 indicates that the state of the subdetector was unknown. A given status value passes all events of that status and higher.

Detector Status							
Detector	CV	CJ	CZ	TB	EB	EE	FD
Detector Status	2	2	0	3	3	3	3

Table 5.1: *Detector status required for cross section measurement.*

Trigger Status							
Detector	CV	CJ	CZ	TB	EB	EE	FD
Trigger Status	0	2	0	3	2	3	0

Table 5.2: *Trigger status required for cross section measurement.*

For the measurement of the taupair production cross section, precise knowledge of the acceptance is vital necessitating tight detector status cuts on tracking and calorimetry subdetectors. TB detector status was required to be 3 to ensure the efficient removal of cosmic ray events and the forward luminometer detector status was required to be 3 to ensure a luminosity measurement for the taupair sample. Similarly, a tight set of trigger status requirements was required for the most important subdetectors comprising the taupair trigger so as to maintain a full understanding of the taupair acceptance.

5.1.2 LL track and cluster quality cuts

To remove noise from events, track and cluster quality cuts were applied. This is particularly important as Monte Carlo events are generally much 'cleaner', hence noise can be the cause of severe systematic effects. CT tracks were used in the reconstruction of taupair events if they satisfied the 'normal' set of track quality cuts listed in table 5.3, tracks were considered for mupair candidature if they satisfied the 'high P_T' cuts and tracks were subjected to the cosmic ray tagging algorithm if they satisfied the 'cosmic' track quality cuts. N_{hits} is the number of hits associated to the CT track and R_f is the radius of the first associated hit in $r-\phi$.

Track Quality Cuts					
	N_{hits}	$\lvert d_0\rvert$ (cm)	$\lvert z_0\rvert$ (cm)	R_f (cm)	P_T (GeV)
Normal	20	1.0	40.0	75.0	0.1
High P_T	20	1.0	50.0	999.0	0.7
Cosmic	20	20.0	500.0	999.0	2.0

Table 5.3: *Track quality cuts used in taupair reconstruction (normal), mupair reconstruction (high P_T) and by the cosmic ray tagging algorithm (cosmic).*

After the removal of 'garbage' clusters and 'hot blocks', ECAL clusters were subjected to a set of 'normal' quality cuts. EB clusters were not used in the reconstruction of taupair candidates if they had a raw energy of less than 100 MeV and EE clusters were not used if they contained a raw energy of less than 200 MeV, they contained less than 2 blocks or if the fraction of the energy contained by the most energetic block was greater than 99%.

5.2 Background Subtraction

$e^+e^- \to \tau^+\tau^-$ events leave a highly characteristic signature inside the OPAL detector, a typical example in the $r-\phi$ plane being shown in figure 5.1 where one of the tau leptons has decayed muonically and the other has decayed into three charged pions. To separate $e^+e^- \to \tau^+\tau^-$ events from the other electroweak and non-resonant events that have passed the preselection, information from central tracking and the electromagnetic calorimeter was used. Additional information from the outer muon chambers and hadron calorimeter was used to reject mupair events and timing information from the TB counters to reject cosmic rays. Taupair events were required to consist of two back-to-back highly collimated low multiplicity hemispheres to reject highly acolinear (non back-to-back topology) two-photon events or multihadronic events exhibiting a widely spread event topology. To reconstruct the event, charged tracks and electromagnetic clusters were treated separately and combined by first taking the highest energy track or cluster and defining a 35° half angle cone around the momentum vector at the vertex. The next highest energy track or cluster inside the cone was extracted, the momenta of the two particles added together and the direction of the sum used to define a new cone axis inside which the next highest energy track or cluster was searched for. This procedure was repeated until no further tracks could be assigned to the cone. The remaining tracks and clusters were then used to initiate a new cone starting from the highest energy track or cluster remaining. The whole process was repeated until all tracks and clusters were assigned to cones. Each cone was then required to have at least one charged track and to carry more than 1% of the beam energy. Taupair events were required to have exactly two such cones. The direction of each tau cone was approximated by the vectoral sum of tracks and clusters assigned to it, and an event axis $(\theta_{\rm avr}, \phi_{\rm avr})$ defined by the vectoral difference of the two jets ie.

$$|\cos\theta_{\rm avr}| = \frac{|R_z^1 - R_z^2|}{|\vec{R}^1 - \vec{R}^2|} \qquad \text{and} \qquad \tan\phi_{\rm avr} = \frac{R_y^1 - R_y^2}{R_x^1 - R_x^2},$$

where $\vec{R}^1$ and $\vec{R}^2$ are the summed CT and ECAL vectors of each jet. Multiplicity

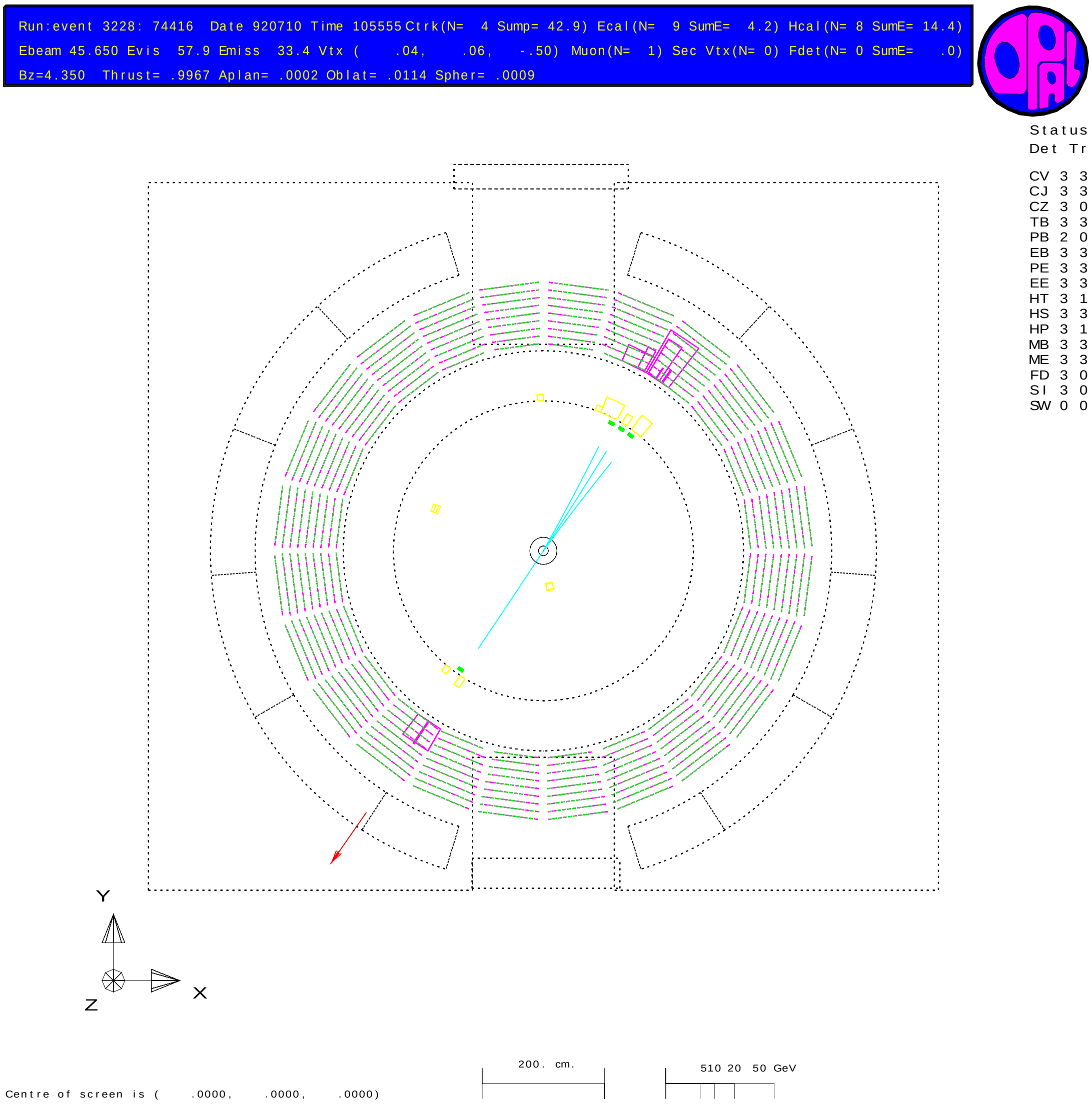

Figure 5.1: *A typical taupair event as seen by the OPAL detector. The arrow in the bottom left hand quadrant indicates a reconstructed muon segment inside MB and the tracks corresponding to the opposing hemisphere clearly indicate a three-prong tau decay.*

cuts were imposed to reject further multihadronic decays of the Z^0 such that:

- $2 \leq N_{\rm trk} \leq 6$ where $N_{\rm trk}$ is the total number of normal quality charged tracks in the event and
- $N_{\rm trk} + N_{\rm cls} \leq 15$ where $N_{\rm cls}$ is the total number of quality ECAL clusters.

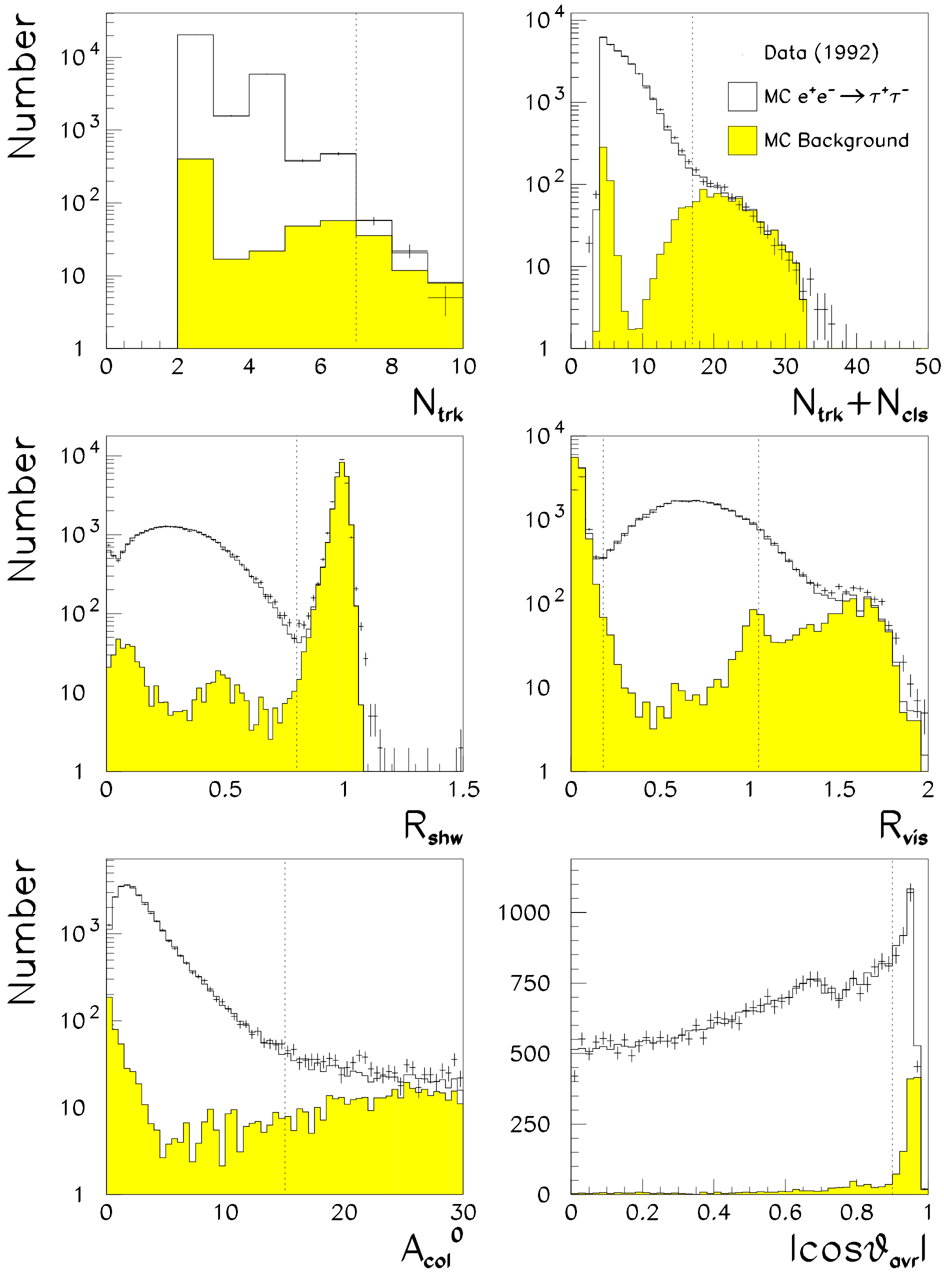

Figure 5.2: *Cut distributions for the selection of taupairs. Plots a) and b) show the multiplicity distributions with cuts used to reject Multihadronic events, plots c) and d) show the energy distributions with cuts used to reject Bhabha and two-photon events, plot e) shows the acolinearity distribution and plot f) the* $|\cos\theta_{\mathrm{avr}}|$ *distribution.*

$N_{\rm trk}$ is known as the 'track multiplicity' of the event and $N_{\rm trk} + N_{\rm cls}$ the 'total multiplicity' of the event. It should be noted that where cones containing only clusters or less than 1% of the beam energy do not contribute to the number of cones in the event, the tracks or clusters inside them do contribute to the total track and cluster multiplicities. Figure 5.2 shows the $N_{\rm trk}$ and $N_{\rm trk} + N_{\rm cls}$ distributions after all other taupair selection cuts have been applied, together with photon conversion and split track finding algorithms, these being described in chapter 7. Data are indicated by points, taupair Monte Carlo by open histogram, background Monte Carlo by shaded histogram and cut values by dotted lines which is the convention throughout the text. The $N_{\rm trk}$ distribution is discussed in section 7.3 and the total multiplicity distribution in section 8.6.1.

Figure 5.3 shows a smoothed Monte Carlo plot of $R_{\rm shw}$ versus $R_{\rm trk}$ for leptonic final states failing two or less taupair selection cuts, where $R_{\rm shw}$ is the event showering energy summed over quality lead glass clusters and $R_{\rm trk}$ the CT tracking energy summed over all normal quality tracks assigned to the event, both normalised to the centre of mass energy. The Monte Carlo samples here have been normalised to the MSM. Two-photon events seen here as the spike at low $R_{\rm shw}$ and $R_{\rm trk}$ were removed by the cut:

- $R_{\rm vis} > 0.18$ where $R_{\rm vis}$, the 'visible energy' is the sum of $R_{\rm trk}$ and $R_{\rm shw}$.

$e^+e^- \to e^+e^-(\gamma)$ events were rejected by the cuts:

- $R_{\rm shw} < 0.8$ and
- ($R_{\rm vis} < 1.05$ or $R_{\rm shw} < 0.25$) for the region $|\cos\theta_{\rm avr}| > 0.7$ where additional material is presented by the pressure bell [42].

Figure 5.2 shows the $R_{\rm shw}$ and $R_{\rm vis}$ distributions after all other taupair selection cuts have been applied. A small data excess is evident in the $R_{\rm shw}$ distribution at the cutting point. Also of note is the discrepancy between data and Monte Carlo in the high $R_{\rm vis}$ region above approximately 1.3 due to poor simulation of 'overlap region' material, this necessitating the endcap $R_{\rm vis}$ cut at 1.05.

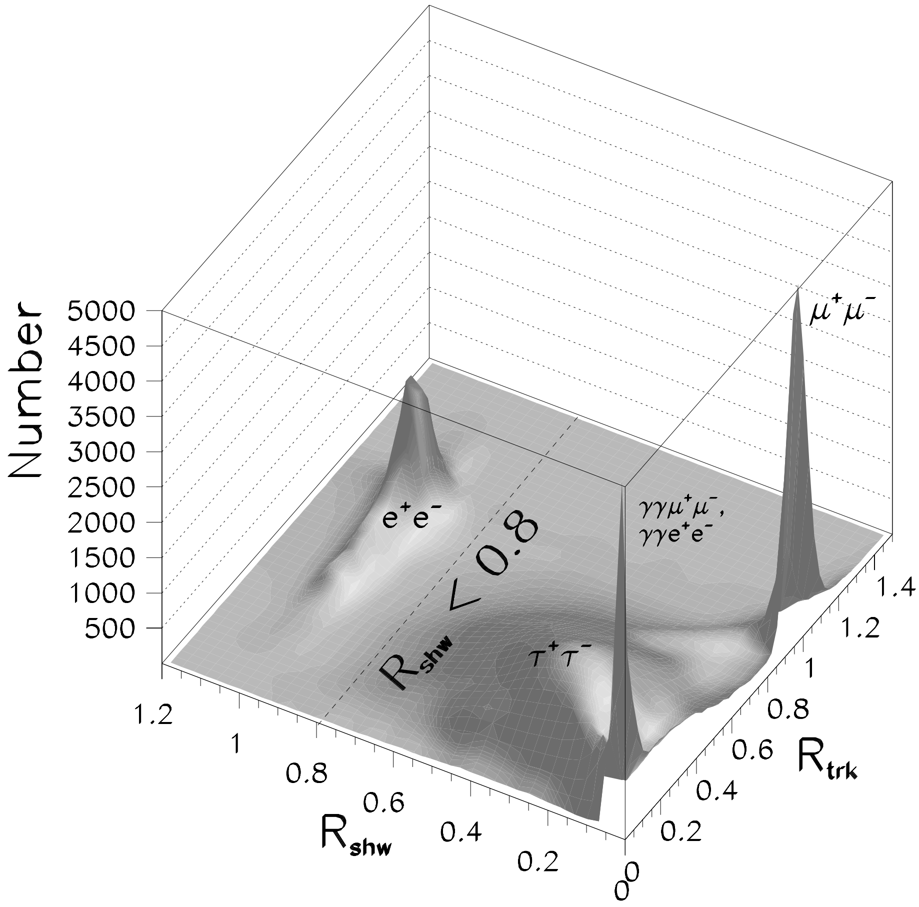

Figure 5.3: *Parameter space spanned by 'total normalised showering energy' R_{shw} and 'total normalised tracking energy' R_{trk} for leptonic final states (Monte Carlo) failing at most two taupair selection cuts. Samples were normalised to the MSM and each smoothed using a multiquadric radial basis function for visualisation purposes [65].*

Both distributions are discussed in detail together with the Monte Carlo simulation of Bhabha background in section 8.3. Further suppression of two-photon background and highly acolinear Bhabha events due to initial state radiation was effected by the cuts:

- $A_{\mathrm{col}} < 15^{\circ}$ where A_{col} is the acolinearity and
- $|\cos\theta_{\mathrm{avr}}| < 0.9$.

Figure 5.2 shows the $A_{\rm col}$ and $|\cos\theta_{\rm avr}|$ distributions with all other cuts applied, these distributions being described in detail in section 8.7.

Direct mupairs seen as the spike at $R_{\rm trk} \approx 1.0$ in figure 5.3 were rejected using the LL standard mupair ID as described in [66] and appendix A, ensuring complete anticorrelation between taupair and mupair samples for the combined leptonic fits. The simulation of mupair background is discussed in section 8.1.

Cosmic ray and beam gas events were rejected using vertex and TB information and are described in detail in chapter 9.

5.2.1 Monte Carlo samples

Peak taupair events were simulated using four vectors generated by KORALZ-38, subject to the full detector simulation GOPAL-129 using the production module GORO-07. Off-peak taupair events were simulated using Monte Carlo runs R1513 and R1516. On peak Bhabha background was simulated using four vectors generated by RADBAB-20 (BABAMC) passed through the production module GORO-07. Off peak Bhabha events were simulated using RADBAB-10 four vector generation and the production module GORO-12. Multihadronic background was simulated using JETSET-73 with GORO-07 and HERWIG-50 with GORO-4 whilst two photon background was simulated by VERMASEREN four vectors passed through GORO-04. ECAL clusters and CT tracks were additionally smeared by a small amount using parameters from the tau-platform package TP102 [63].

5.3 Cross section determination

The taupair production cross section σ_τ is determined by the relation:

$$\sigma_\tau = \frac{N_{\rm sel} - N_{\rm bg}}{\epsilon \int L {\rm dt}}$$

where $N_{\rm sel}$ is the number of selected events, $N_{\rm bg}$ is the number of background events in the sample and ϵ denotes the correction for the finite selection efficiency imposed by the geometrical acceptance cuts, the background reduction cuts and the trigger efficiency. $\int L\mathrm{d}t$ is the integrated luminosity for the sample as determined by FD or SiW. The background correction can be expressed in the form of a multiplicative correction factor f where:

$$N_{\mathrm{sel}} - N_{\mathrm{bg}} = f N_{\mathrm{sel}}$$

and provided that background fractions are low, f can be constructed by taking:

$$N_{\mathrm{sel}} - N^{i}_{\mathrm{bg}} = f^{i} N_{\mathrm{sel}}$$

with:

$$f = \Pi_{i=1}^{N_{\mathrm{B}}} f^{i} \ .$$

f^i indicates the correction factor for background number i and N_{B} is the number of backgrounds considered. Similarly, ϵ can be absorbed into f. For simplicity therefore, in the following chapters we quote correction f factors for individual backgrounds and efficiencies. The systematic errors associated with each correction factor are quoted in the form $\Delta f/f$.

The challenge of the analysis is motivated by the aim to match systematic errors associated with the background determination, selection efficiency and acceptance correction to that of the statistical error. This was carried out by the use of a multitude of systematic cross-checks, these being described in the following chapters. These checks allow second order corrections to be made to the first order Monte Carlo predictions for the correction factors with the exception of the cosmic ray background; no cosmic ray Monte Carlo exists so the full correction factor for this background was based upon careful analysis of the cosmic ray tagging algorithm and its corresponding distributions (chapter 9).

5.3.1 Determination of the absolute luminosity

The absolute luminosity was obtained using the forward luminometers situated in the far forward region of OPAL. Here, the low angle t-channel dominated Bhabha cross section is very high, a process driven by QED. The absolute luminosity can hence be determined by taking the ratio of the number of events of this type seen to the theoretical cross section within the finite acceptance.

Source of uncertainty	Uncertainty 1992
8 'telescope' study	0.17%
drift chamber survey of tubes	0.17%
simulation systematics	0.23%
locations of drift chamber sense wires	0.08%
distance to interaction point	0.04%
calorimeter coordinates	$< 0.01\%$
trigger efficiency	$< 0.02\%$
reconstruction efficiency	$< 0.01\%$
accidental background	$< 0.01\%$
data statistics	0.18%
Monte Carlo statistics	0.12%
overall	**0.41%**

Table 5.4: *The 1992 FD analysis systematic errors.*

At small angles, the 1st order Bhabha scattering differential cross section is given by:

$$\frac{d\sigma}{d\theta} \simeq \frac{32\pi\alpha^2}{s} . \frac{1}{\theta^3} ,$$

giving an integrated cross section of:

$$\sigma_{\text{Bhabha}} \simeq \frac{16\pi\alpha^2}{s} . \left(\frac{1}{\theta^2_{\text{min}}} - \frac{1}{\theta^2_{\text{max}}} \right) .$$

For FD, θ_{min} and θ_{max} are approximately 47 mrad and 120 mrad so it is the precise determination of the inner edge that systematically limits the precision of the luminosity determination. Measurement of the luminosity is in itself a highly demanding analysis, the full OPAL FD and SiW analyses being given in [67] and [68] respectively. In the following chapters we shall deal with 1992 data only, in order to outline the procedures used to determine the total taupair cross section systematic. In chapter 10.1 we shall outline the differences for the 1993 data set and the additional cross checks and changes to the systematics that are made possible due to increases in statistics and the existence of off-peak data.

For the 1992 data, SiW was unavailable so no further mention of it here will be made. Instead it is discussed in chapter 10.1.2 with reference to the 1993 data measurement. The limiting errors on the FD luminosity measurement for 1992 data are given in table 5.4 for completeness. The total systematic error of $\pm 0.41\%$ has to be added in quadrature to the theoretical uncertainty of 0.3% giving a total systematic/theory luminosity error for 1992 data of 0.51%.

5.3.2 LEP Energy calibration

The statistical error on the mass of the Z^0 and its width Γ_Z as determined by the combined LEP fit dictate the level of required accuracy for the uncertainty in the LEP energy calibration, this being handled by the LEP Energy Working Group. By making regular 'resonant depolarization' calibrations throughout the year, the model used to calculate E_{cm} for the 'uncalibrated' fills can be tested. The value of E_{cm} for uncalibrated fills is based upon measurement of the magnet dipole current and includes corrections for the magnet temperature, Moon-tide and RF. An orbit correction is also provided by beam orbit monitors. To date, the analysis is sufficiently understood so as to be able to determine the centre of mass energies of the off-peak points to ~ 2 parts in 10^5, resulting in systematic errors to the Z^0 mass and width of $\sim$1.4 MeV and $\sim$1.5 MeV respectively (1993 data). An error of $\pm$5.4 MeV was determined for the energy of the 1993 peak point. For 1992 data, resonant depolarisation studies were only achieved late in the year resulting in an error of $\pm$18 MeV for the peak centre of mass energy.

The spread in centre of mass energy due to the energy spread of particles within the beams ($\sim 50 \pm 5$ MeV) is standardly corrected for inside the fitting procedure.

Chapter 6

Branching Ratio Selection

Due to the large mass of the τ lepton ($1777.1^{+0.4}_{-0.5}$ MeV) [20], it can weakly decay via a multiplicity of decay modes. There have been many recent reviews regarding the state of knowledge as regards taupair branching ratios [22][69][70], however with current statistics, for a cross section measurement it is sufficient to model only the more significant mechanisms as many branching ratios are small and expected to have selection bias factors similar to the more dominant modes. KORALZ-38 generates τ leptons which decay via the 13 channels listed together with their raw decay branching fractions in table 6.1. The generator assumes a uniformly flat phase space for the decay of τ leptons into three and four meson states ignoring intermediate resonant structure, and the three charged hadron final state is assumed to be completely dominated by the $\tau^- \to {a_1}^- \nu_\tau ({a_1}^- \to \pi^-\pi^+\pi^-)$[1] decay chain where two of the final state pions originate from a ρ^0 decay. Generator level branching fractions were adjusted to PDG94 world average values [71] by producing scaling factors for each channel, TREE level information being used to map particles to their respective decays. The $\tau^- \to 3h^-\nu_\tau$ and $\tau^- \to h^-2\pi^0\nu_\tau$ channels were modelled by the a_1 resonance and decays to $3h^-\pi^0\nu_\tau$, $h^-3\pi^0\nu_\tau$, $5h^-\nu_\tau$, and $5h^-\pi^0\nu_\tau$ modelled completely by pions in the final state. Decays containing three charged mesons were scaled to the weighted average of the current OPAL [72], ALEPH and CLEOII [73] values listed

[1] wherever lepton or meson charge is quoted, the existence of the charge conjugate decay is always implied.

in table 6.2 rather than using the PDG94 values. The motivation for this was due to severe systematic effects present in earlier measurements which are still contained in the world average PDG94 values. For the OPAL value which contains asymmetric systematic errors, the largest error was used. Only recently have consistent values for these decays started to emerge due to improvements in state of the art tracking and calorimetry. The decay $\tau^- \to 3h^-2\pi^0$ is unmodelled by the Monte Carlo, and so was simulated by the $\tau^- \to 3\pi^-\pi^0$ channel (the branching ratio of this mode is listed by PDG94 as $(4.9 \pm 0.5) \times 10^{-3}$ and is therefore significant with current statistics.) Decay branching ratios for final states passing through the charged $K^*(892)^-$ resonance were derived using isospin symmetry arguments and a 50:50 branching fraction for the decays $K^*(892)^- \to K_L^0\pi^-$ and $K^*(892)^- \to K_S^0\pi^-$.

Decay Mode	Measured B.R. (B_n) [%]	KZ-38 B.R.[%]	Scaling Factor	R_n
$\tau^- \to \mu^-\nu_\mu\nu_\tau$	17.65 ± 0.24	17.72 ± 0.06	0.9938	09978
$\tau^- \to e^-\nu_e\nu_\tau$	18.01 ± 0.18	18.25 ± 0.06	0.9852	0.9984
$\tau^- \to \pi^-\nu_\tau$	11.7 ± 0.4	11.73 ± 0.05	0.9919	0.9944
$\tau^- \to \pi^-\pi^\circ\nu_\tau$ $[\rho^-]$	25.2 ± 0.4	24.16 ± 0.07	1.0403	0.9974
$\tau^- \to \pi^-\pi^+\pi^-\nu_\tau$ $[a_1^-]$	9.78 ± 0.21	8.44 ± 0.04	1.1547	0.9965
$\tau^- \to \pi^-\pi^\circ\pi^\circ\nu_\tau$ $[a_1^-]$	9.6 ± 0.4	9.84 ± 0.05	0.9690	0.9932
$\tau^- \to K^-\nu_\tau$	0.67 ± 0.23	0.84 ± 0.01	0.7529	0.9440
$\tau^- \to K^-\pi^\circ\nu_\tau$ $[K^*(892)^-]$	0.483 ± 0.06	0.59 ± 0.01	0.8020	0.9797
$\tau^- \to \pi^-K^\circ\nu_\tau$ $[K^*(892)^-]$	0.967 ± 0.12	1.17 ± 0.02	0.8098	0.9797
$\tau^- \to \pi^-\pi^+\pi^-\pi^\circ\nu_\tau^1$	5.00 ± 0.22	0.59 ± 0.04	0.8414	0.9928
$\tau^- \to \pi^-\pi^\circ\pi^\circ\pi^\circ\nu_\tau$	1.28 ± 0.24	1.22 ± 0.02	1.0171	0.9694
$\tau^- \to \pi^-\pi^+\pi^-\pi^+\pi^-\nu_\tau$	0.056 ± 0.016	0.07 ± 0.00	0.7627	0.9534
$\tau^- \to \pi^-\pi^+\pi^-\pi^+\pi^-\pi^\circ\nu_\tau$	0.051 ± 0.022	0.07 ± 0.00	0.6773	0.9296

Table 6.1: *Tau decay branching ratios used in the analysis together with the raw Monte Carlo generator branching fractions, the appropriate scaling factors and values R_n demonstrating the degree to which normalisation affects the chosen branching ratios.*

[1]channel has an increased branching ratio to model the $\tau^- \to 3h^-2\pi^0\nu_\tau$ decay.

As the PDG94 branching ratios are not normalised to exactly 100%, each branching ratio B_n was additionally scaled by an error dependent scaling factor R_n such that

$$\sum_{n=1}^{13}(R_n)B_n = 1.0 \tag{6.1}$$

where

$$R_n = 1.0 + a\left(\frac{\sigma_n}{B_n}\right),$$

a being the normalisation parameter and σ_n the error on branching ratio B_n. Values of R_n are shown in table 6.1 and adjust each branching ratio by a factor equal to 0.16 times the assigned experimental error. Scaling factors for KORALZ-38 tau decays are listed and were used to reweight events by producing re-weighting factors equal to the product of scaling factors for each hemisphere which could then be used in the binning of histograms.

$\tau^- \to 3h^-\nu_\tau$	
Measurement	B.R.[%]
CLEO II ('94 prelim)	$9.82 \pm 0.09 \pm 0.34$
ALEPH ('92 prelim)	$9.57 \pm 0.24 \pm 0.22$
OPAL ('94 prelim)	$10.07 \pm 0.20^{+0.21}_{-0.38}$

$\tau^- \to 3h^-\pi^0\nu_\tau$	
Measurement	B.R.[%]
CLEO II ('94 prelim)	$4.25 \pm 0.09 \pm 0.26$
ALEPH ('92 prelim)	$4.94 \pm 0.26 \pm 0.34$
OPAL ('94 prelim)	$4.79 \pm 0.20^{+0.45}_{-0.26}$

Table 6.2: *Tau decay branching ratios chosen for decays into three charged mesons. For the OPAL result, the extreme error was used.*

To investigate the effect upon the taupair selection acceptance due to decay mode bias in the sample and poor knowledge of branching ratios, each branching ratio was varied to a normal distribution with an RMS half width equal to σ_n. For each iteration, branching ratios were normalised to 100% using equation 6.1, scaling factors calculated and the ratio of the new acceptance to the acceptance for the chosen set of branching ratios binned. 10^6 iterations produced an RMS deviation of 0.04% in the fraction of accepted Monte Carlo taupair events. A more conservative estimate of the effect of branching ratio choice upon acceptance was determined by expanding the error on the $\tau^- \to 3h^-\nu_\tau$ channel to 7 times the quoted value of σ_n, thus covering the discrepancy between the chosen value and the DELPHI ('93 preliminary) result of $8.35 \pm 0.35 \pm 0.24\%$ [73]. Repeating the analysis with this modification yields an RMS deviation of 0.10% in the accepted taupair fraction; we thus assign a systematic correction factor to the acceptance of:

$$f = 1.0000 \qquad \Delta f/f = 0.0010 \; .$$

A difference of 0.07% exists in the ratio of selected data to Monte Carlo events if the raw Monte Carlo branching ratios are used instead of the chosen set. This uncertainty is lower and of the same order as the chosen one.

In summary, the choice of Monte Carlo branching ratios can be seen to have a small effect upon the taupair cross section systematic error.

Chapter 7

Photon conversion and Split Track rejection

In the past, various analyses have been carried out which require examination of photon conversions in OPAL events and their Monte Carlo simulation [75]. In particular, attempts to determine the $\tau^- \rightarrow h^- h^+ h^- \nu_\tau$ branching ratio [72] have demonstrated there to be a deficit in the number of Monte Carlo conversions in taupair events compared to data due to the poor simulation of material preceding the Jet Chamber. This material comprises two layers of silicon support structures between approximately 6 and 7 cm, the outer beam-pipe at approximately 8 cm, a layer of foil separating the CV axial and stereo wires and a layer of carbon fibre tube separating CV from CJ together with a layer of kapton foil with copper traces for field shaping. This constitutes approximately 0.05 radiation lengths of material. The taupair selection cut systematics on charged track and total multiplicity are seriously affected by the simulation of photon conversions.

Further, analysis of the direct mupair channel has shown there to exist a 'track splitting' effect for high energy tracks in close proximity to CJ anode and cathode planes not modelled by the Monte Carlo [76].

An attempt was therefore made to tag photon conversions and split tracks and to reduce the corresponding cones to their correct multiplicity so as to decrease the multiplicity cut systematic errors.

7.1 Photon conversions

A search was made for oppositely charged tracks with a θ difference $\Delta\theta$ less than 1 radian in each considered event using a modification of the ID package [61] conversion tagging algorithm IDGCON. All OD recorded tracks were considered as only one of the conversion tracks may have passed the normal track quality cuts (table 5.3). The conversion radius of the two candidate tracks was defined as the point where the tangents of the two tracks were parallel in the $r - \phi$ plane. The $x - y$ separation at this point Δ_{xy} was required to be less than 5 cm. A hit was then required on either track within 20 cm of the conversion radius if the conversion radius was greater than 27 cm and within 30 cm if the conversion radius was less than 27 cm. For all track pairs passing these 'loose' requirements a further set of 'tight' cuts were applied. A dimensionless quantity D was calculated where:

$$\begin{aligned} \mathrm{D} &= \sqrt{\left(\frac{\Delta xy}{xy_{90}}\right)^2 + \left(\frac{\Delta\theta}{\theta_{90}}\right)^2} \quad \text{for} \quad R_f < 27\text{cm} \quad \text{and} \\ &= \sqrt{\left(\frac{\Delta xy}{xy_{90}}\right)^2} \quad \text{for} \quad R_f > 27\text{cm}, \end{aligned}$$

R_f being the radius of the closest hit to the vertex out of the two candidate tracks. xy_{90} and θ_{90} are values within which 90% of photon conversions are expected to be contained. Their values have been estimated separately for data and Monte Carlo in three regions, namely $R_f < 22$ cm, 22 cm$< R_f < 27$ cm, and $R_f > 27$ cm. In the third region outside CV, θ is poorly measured and only $x - y$ information was used. For each cone, all track pair combinations were examined and the pair with the minimum value of D flagged. If this value lay between 0 and 2 and provided the signed conversion radius was greater than -2 cm and that the tracks formed a mutual pair, they were tagged as photon conversion tracks.

7.2 Split track removal

Split tracks were identified using a modification of the LLJOIN mupair track joining routine from LL156 [62]. Pairs of tracks (i and j) were flagged as split track candidates if they had an overlap $O_{\mathrm{LAP}} < 0.67$ where:

$$O_{\mathrm{LAP}} = \frac{\min(R_l^i, R_l^j) - \max(R_f^i, R_f^j)}{\max(R_l^i, R_l^j) - \min(R_f^i, R_f^j)}$$

and a separation angle θ_{ij} at the e^+e^- vertex satisfying $\cos\theta_{ij} > 0.999$. R_l is the radius in $r-\phi$ of the outermost hit assigned to the track.

Figure 7.1 shows the track anode-plane angle at the vertex for tracks tagged for deletion and various initial cone topologies. Data/Monte Carlo disagreement can be seen around the CJ anode and cathode planes. A further set of cuts were applied such that tracks were only deleted if they were within $\pm 1°$ of the anode or cathode to prevent a large number of genuine highly boosted 3-prong τ decays being incorrectly flagged as containing split tracks. The excesses of data compared to Monte Carlo for which split tracks were removed were $0.23 \pm 0.03\%$ and $0.06 \pm 0.02\%$ for initial topologies 2 and 4 respectively and $-0.01 \pm 0.03\%$ for initial topology 3 demonstrating good data/Monte Carlo agreement for the incorrectly tagged cones.

7.3 Application of the algorithms

To prevent an increase in multihadronic background due to conversions being removed from multihadronic events just outside the taupair multiplicity cuts, conversion tracks were only removed provided events had a topology consistent with that of taupair events. This was important as the low multiplicity tail of the multihadronic channel is not well simulated, JETSET and HERWIG predicting significantly different levels of multihadronic background. This will be further discussed in section 8.6.2. Conversion tracks assigned to the event were removed if events satisfied the following cuts:

- $P^2_{\mathrm{INV}}(\max) < 3\mathrm{GeV}^2$,
- $P^2_{\mathrm{INV}}(\min) < 1\mathrm{GeV}^2$,
- $\theta_{\mathrm{ISO}} > 2.85°$,

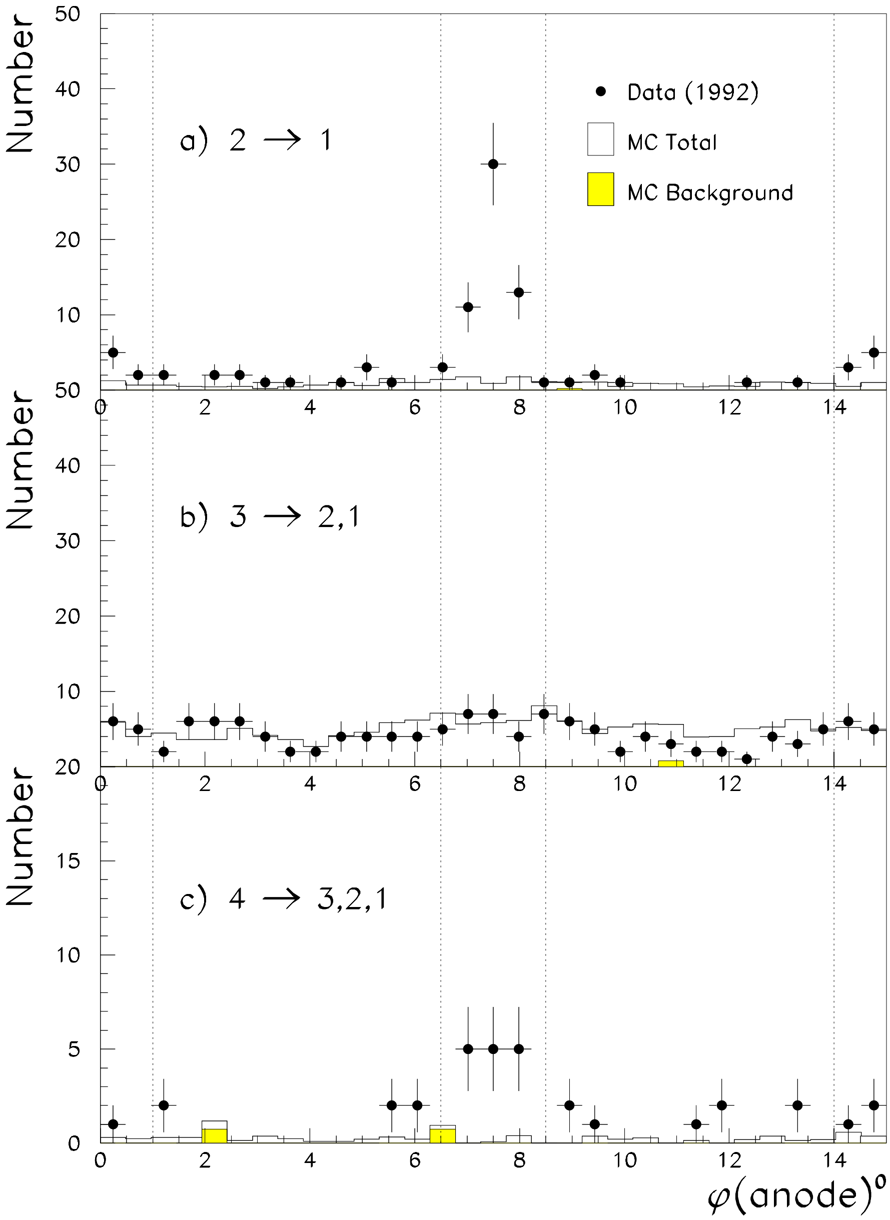

Figure 7.1: *Angle between track momentum vector at the e^+e^- vertex and the nearest CJ anode plane for tracks tagged by the split track finding algorithm. Plot a) is for τ cones reduced from multiplicity 2 to multiplicity 1, plot b) contains cones reduced from multiplicity 3 to multiplicity 2 or 1 and plot c) consists of cones reduced from multiplicity 4 to multiplicity 3,2 or 1. Dotted lines represent the cuts used to reduce the amount of genuine 3-prong decay track joining.*

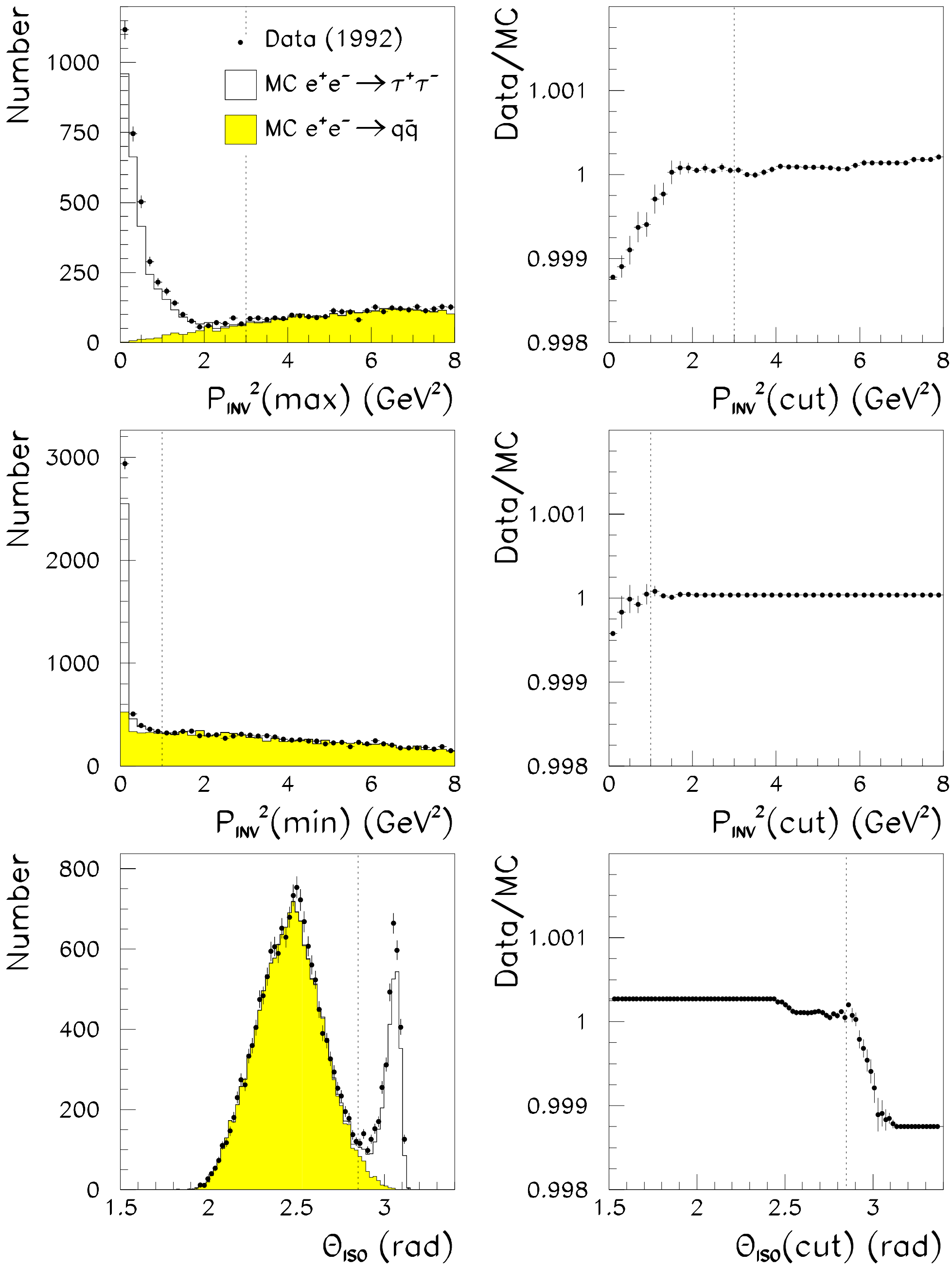

Figure 7.2: *Plots on the left show* $P_{\rm INV}^2$ *and* $\theta_{\rm ISO}$ *distributions for events with tagged photon conversions. Cutting at the points marked by arrows and then varying each cut individually produces the acceptance variation shown to the right of each plot.*

where $P_{\rm INV}$ is simply the invariant mass of the hemisphere constructed using charged tracks and assuming a photon hypothesis[1]. $\theta_{\rm ISO}$ is the minimum angle between tracks in opposing hemispheres (the isolation angle) and is used by the DELPHI collaboration in their taupair selection [78]. These cuts essentially exploit the fact that multihadronic decay jets are generally wider than jets from tau lepton decays. There is also a degree of redundancy in the cuts due to the correlation between the two jets caused by the $\theta_{\rm ISO}$ cut, meaning that cut values can be made loose to reduce systematics. In the case where a tau cone consisting of a single track was tagged as a conversion track due to poor conversion reconstruction with tracks in the hemisphere which had not passed the normal track quality cuts, conversion track deletion was over-ridden.

Distributions of $P^2_{\rm INV}(\rm max)$, $P^2_{\rm INV}(\rm min)$ and $\theta_{\rm ISO}$ for events with tagged photon conversions (inside and outside the taupair sample) are shown to the left of figure 7.2. As mentioned earlier, the aim of introducing conversion and split track finding algorithms into the analysis is to reduce the multiplicity cut systematics. It is also important however that conversion and split track finding algorithms do not in themselves introduce any systematic uncertainty. Each cut listed above was therefore varied with the other cuts applied and the ratio of selected data to Monte Carlo events examined, relevant plots being shown to the right of their respective distributions in figure 7.2 (the errors shown are due to variation in statistics from one bin to the next). The systematic effects seen in the $P^2_{\rm INV}$ distributions are simply due to conversion finding being gradually turned on as the cut is moved to the right, the data/Monte Carlo discrepancy in the taupair sample being evident from the plots to the left. Indeed, the cut redundancy means that one of the two plots could be removed (moving the cut to the right does not appreciably alter the taupair selection efficiency or the data to Monte Carlo ratio). This is not true however of the $\theta_{\rm ISO}$ cut, as moving it to the left does alter the data to Monte Carlo ratio slightly. We therefore take the discrepancy between the ratio at the chosen $\theta_{\rm ISO}$ value and the value with the cut turned off completely as a systematic error:

[1]'max' and 'min' refer to the maximum and minimum values out of the two cones.

$$f = 1.0000 \qquad \Delta f/f = 0.0003 \ .$$

An increase in the taupair selection efficiency of $0.40 \pm 0.01\%$ resulted due to application of conversion and split track finding algorithms and a corresponding increase to the multihadronic background of $0.03 \pm 0.01\%$. The final systematic error associated with the track multiplicity cut by varying the $N_{\rm trk}$ cut between $N_{\rm trk} < 4$ and $N_{\rm trk} < 9$ was found to be 0.11% compared with 0.66% for the raw multiplicity distribution, figure 7.3 showing the relevant plot of $N_{\rm DATA}/N_{\rm MC}$ versus the $N_{\rm trk}$ cut. For the corrected data, no variation outside that expected due to statistical fluctuation was observed; hence we quote a correction factor and systematic error of:

$$f = 1.0000 \qquad \Delta f/f = 0.0011.$$

Error bars are due to the variation in statistics from the cut value at $N_{\rm trk} < 7$.

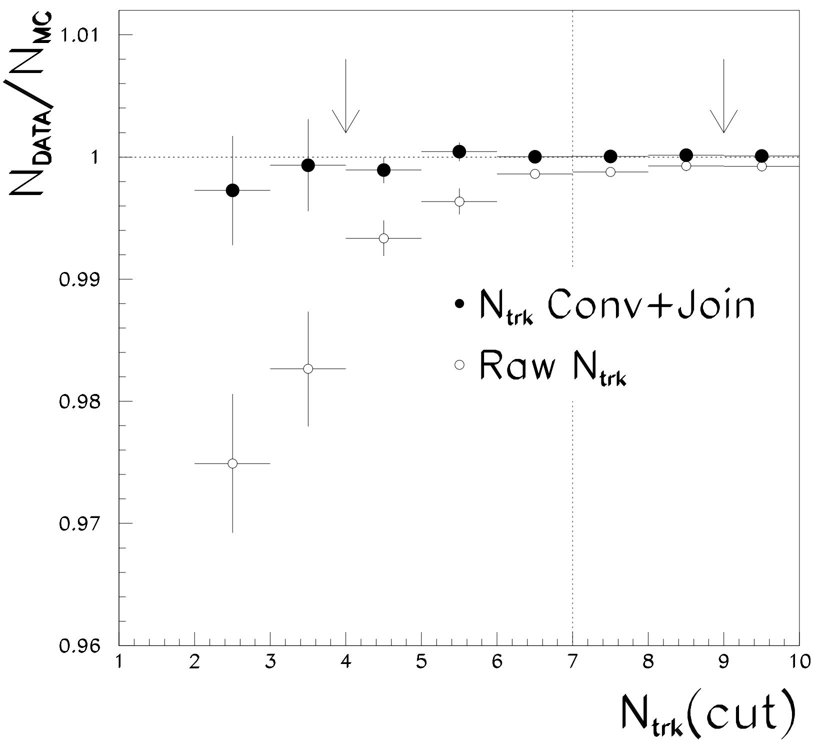

Figure 7.3: *Plots showing the ratio of selected data to Monte Carlo as a function of the choice of $N_{\rm trk}$ cut before and after conversion finding and split track algorithms have been applied.*

Chapter 8

Electroweak and Non-Resonant Background

The primary backgrounds which remain after taupair selection are listed with their respective raw Monte Carlo background fractions in table 8.1. Mupair events were normalised to the data assuming lepton universality, multihadronic events were normalised by taking the ratio of hadronic to leptonic widths as 20.95 and Bhabha and two-photon events were normalised using their respective Monte Carlo production cross sections. The total number of selected Monte Carlo events was then normalised to the total number of selected data. For Bhabha Monte Carlo, the cross section was calculated using ALIBABA [74].

Background Channel	Background fraction [%]	MC Uncertainty [%]
Mupairs	0.83	0.02
Multihadrons	0.47	0.04
Bhabhas	0.15	0.02
Two photon mupairs	0.11	0.01
Two photon electron pairs	0.34	0.03
4-Fermion events	0.07	0.00
Total background	**1.97**	**0.06**

Table 8.1: Raw Monte Carlo predictions for background fractions contained within the taupair sample.

Accurate determination of the taupair production cross section necessitates well understood systematic uncertainties and hence checks upon the Monte Carlo simulation. This was effected via the use of signal and background reduction cuts, background or selection efficiency respectively being kept as high as possible. The following sections describe the studies carried out on the backgrounds listed in table 8.1. Chapter 9 deals with the determination of cosmic ray and beam gas background which differs in the respect that the analysis does not benefit from the existence of Monte Carlo events.

8.1 Mupair background

Mupair events were rejected using the standard LL mupair ID flag [66], the full set of selection cuts being summarised in appendix A. Using the mupair flag to reject direct mupair events ensures complete anticorrelation between lepton pair samples for the lineshape fit assuming lepton universality. Mupair events enter as background via the processes of 'hard final state radiation', 'moderate final state radiation' and 'tracking losses', these being described in the following sections.

8.1.1 Hard final state radiation

Events which failed to be identified as direct mupairs due to the 6 GeV track energy requirement imposed on each track (see appendix A) where one muon underwent heavy final state radiation were selected as follows. One of the two hemispheres was required to consist of a single track having an associated MB/ME segment together with the requirement that it carry a tracking energy in excess of 40 GeV (the non radiative muon candidate). The opposing hemisphere was required to consist of one charged track of tracking energy less than 6 GeV and cluster energy greater than 20 GeV. Lastly, the whole event was required to have an acolinearity of less than 1°. Figure 8.1a) shows the momentum of the non radiative cone with all cuts except the 40 GeV track energy cut applied and similarly figure 8.1b) the acolinearity of selected events with all cuts except the acolinearity cut active. Throughout the text, enhancement cuts are marked by arrows and taupair selection cuts by dotted lines. The selection efficiency for this particular background source was determined to be $(77.9 \pm 2.6)\%$ and the Monte Carlo agreed excellently with data at the 0.4σ level corresponding to a $(0.01 \pm 0.03)\%$ data deficit as a fraction of the whole taupair sample. We therefore quote a conservative systematic error for this background source equal to 0.013% ie. the deficit of 0.010% expanded for the finite efficiency. There is no indication that a correction needs to be made to the acceptance due to poor Monte Carlo simulation and hence in summary, the correction and error for the existence of mupair background in the sample due to hard final state radiation were determined to be:

$$f = 1.0000 \qquad \Delta f/f = 0.0001 \ .$$

8.1.2 Moderate final state radiation

Outside the MB/ME active area, muon identification efficiency drops significantly, an effect compounded by poor HCAL acceptance in this region. $(67.7 \pm 1.3)\%$ of the mupair background in the sample consists of mupair events which have failed to be identified due to reliance upon ECAL/CT muon-ID cuts accompanied by final state radiation outside the MB/ME active area. Mupair background was enhanced by selecting events which failed to point to the MB/ME fiducial area. The radiative cone was required to have a cluster energy in excess of 3 GeV or a tracking momentum of no more that 15 GeV (see appendix A) and a tracking momentum in excess of 6 GeV to prevent double counting of the highly radiative mupair background. The non-radiative cone was required to have a tracking momentum in excess of 40 GeV and a cluster energy of no more than 3 GeV. Figure 8.2 shows the tracking momentum and calorimetric energy of the non-radiative hemisphere for selected mupair background candidates, each distribution being shown with all other cuts applied. The selection efficiency for this background source was $(92.4 \pm 0.9)\%$ and data agreed with Monte Carlo at the 0.3σ level corresponding to a data deficit of $(0.01 \pm 0.05)\%$. We therefore quote a correction to the taupair acceptance of:

$$f = 1.0000 \qquad \Delta f/f = 0.0001 \ .$$

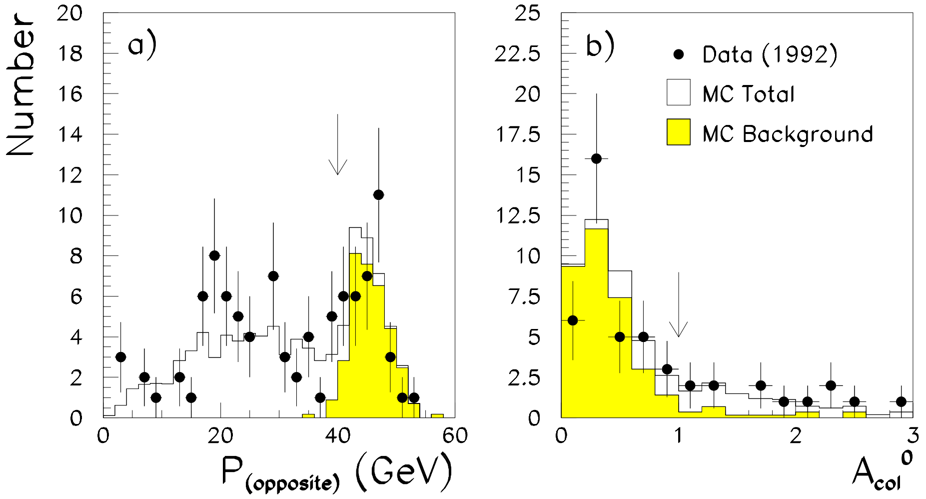

Figure 8.1: *Mupair selection cuts for events failing the mupair ID due to extremely hard final state radiation. The plot on the left shows the momenta of the non radiative muon cones in mupair candidates and the plot to the right the acolinearity.*

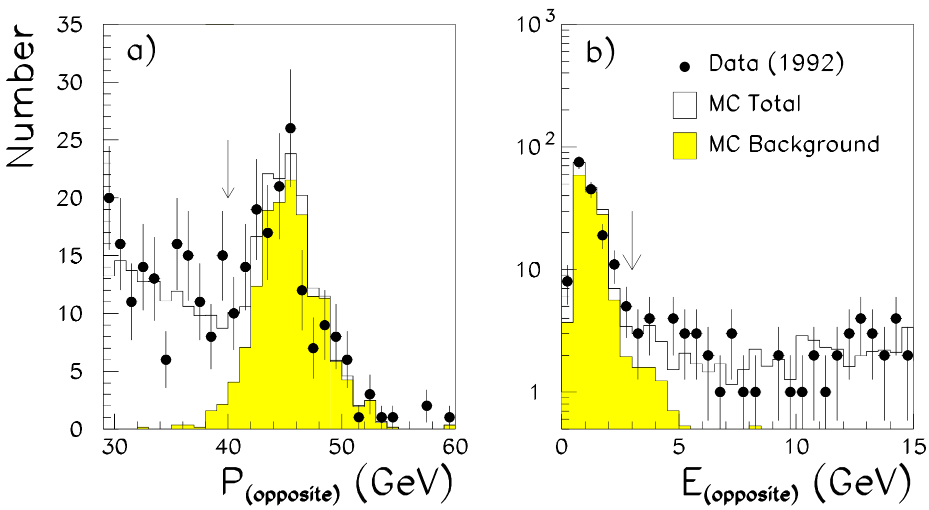

Figure 8.2: *The momentum and calorimetric energy of the non-radiative muon candidate for selected moderate final state radiation mupair background events. The tracking momentum is shown without the 40 GeV cut applied and the cluster energy without the 3 GeV energy cut.*

to account for the simulation of mupair background due to moderate final state radiation where the conservative error of 0.01% has been taken from the observed deficit expanded to account for the finite efficiency.

8.1.3 Tracking losses

After removing direct mupairs from the sample which failed to be identified due to either hard or moderate final state radiation, the remaining background was found to be due to mupairs with poorly reconstructed tracks. This causes mupair candidates to fail the $F_{\rm vis}$ cut[1] at 0.6 (see appendix A). Background was enhanced by making a selection which was almost completely independent of CT information. The acoplanarity of the event[2] was constructed using clusters only (only in the event of a cone containing no quality clusters was the tracking acoplanarity used) and required to be less than 2.2°. The total tracking energy was required to exceed 50% of the centre of mass energy and each hemisphere was required not to exceed 2 GeV in total calorimeter energy. The efficiency for selecting this background source was determined to be $(91.0 \pm 3.2)\%$. A data excess of $(0.20 \pm 0.04)\%$ was observed concentrated mainly around the CJ anode and cathode planes and in the highly forward region of the detector necessitating a correction to the taupair acceptance of:

$$f = 0.9980 \qquad \Delta f/f = 0.0005$$

where the error of 0.05% is the quadrature sum of the data and Monte Carlo statistics error and the error due to the fact that some excess background events may not have been identified due to the finite efficiency in the selection. The cut at $R_{\rm trk} > 0.5$ was varied and the excess found to be stable. Figure 8.3 shows the track to CJ anode plane angle for the selected excess, this being concentrated mainly around the anode plane at 7.5°.

Table 8.2 shows the correction factors together with the final correction factor associated with mupair background, corresponding to a total background of $(1.03 \pm 0.05)\%$ (conservatively including the Monte Carlo statistics error).

[1]the cut designed to separate double $\tau^- \to \mu^- \nu_\tau \overline{\nu_\mu}$ decays from genuine direct mupair events
[2]acoplanarity: the acolinearity projected into the $r - \phi$ plane.

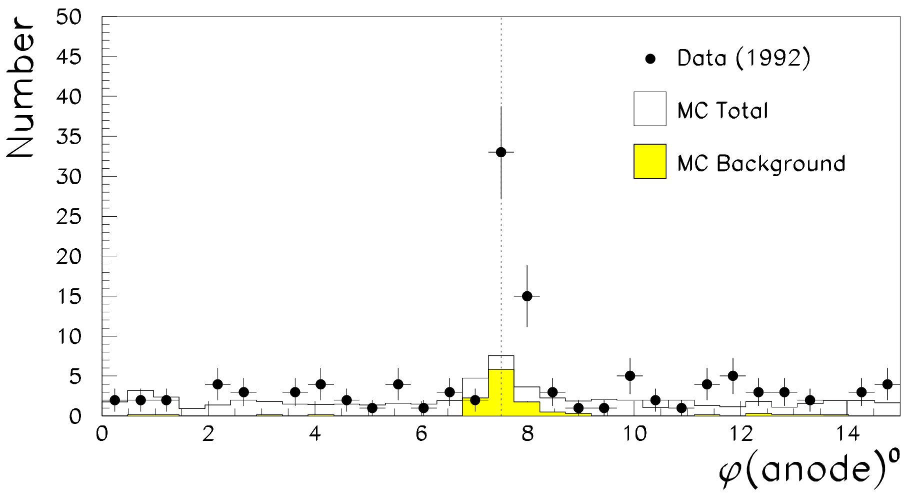

Figure 8.3: *the angle between selected mupair tracks and the nearest CJ anode plane for selected mupair tracking failure candidates. The anode plane is at 7.5°.*

Mupair Simulation Acceptance Correction		
Cause of Background	Correction Factor	Uncertainty [%]
Raw MC	0.9917	0.02
Hard FSR	1.0000	0.01
Moderate FSR	1.0000	0.01
Tracking losses	0.9980	0.05
Total correction factor	**0.9897**	**0.05**

Table 8.2: *Summary of the mupair background sources and their background correction factors together with the total mupair background correction factor.*

8.1.4 Misclassification of taupair events as direct mupair events

Not only is the direct mupair background simulation important for the measurement of the taupair cross section, the loss of taupair events to the mupair channel must also be examined to provide well understood tests of lepton universality and an accurate systematic error for the taupair cross section.

Events classified as mupairs by the standard LL mupair ID were selected provided they had a ϕ axis greater than 0.8° away from CJ anode planes and 0.5° away from cathode planes so as not to contaminate the sample with the poorly tracked mupairs described in section 8.1.3. The taupair to mupair ratio was increased by removing events from the sample if they possessed an acolinearity of less than 0.5° or the minimum cone momentum was greater than 36 GeV. The efficiency for selecting misidentified taupair events by this method was determined to be $(59.0 \pm 0.9)\%$. Figure 8.4 shows the visible energy distribution before and after the mupair rejection cuts for events satisfying the LL mupair ID. A data excess of $(0.10 \pm 0.06)\%$ (1.6σ) exists for events with a visible energy less than 0.8, hence we assign an efficiency corrected systematic error of 0.17% to the taupair acceptance:

$$f = 1.0000 \qquad \Delta f/f = 0.0017$$

This is believed to be a conservative over-estimate as the excess is most probably due to mupair tracking failure in the forward region of the detector.

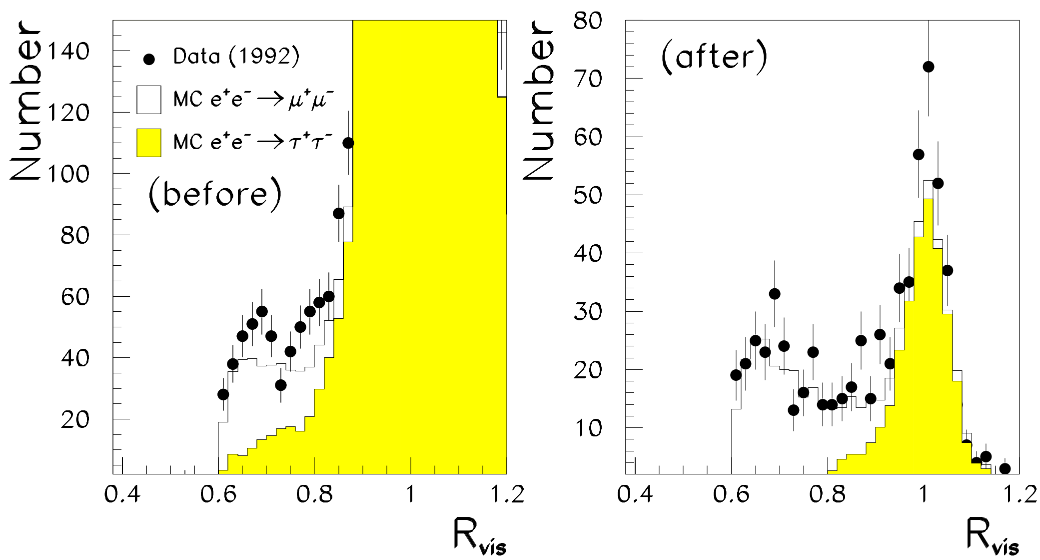

Figure 8.4: *The plot to the left shows the $R_{\rm vis}$ distribution for events passing the LL mupair ID and the plot to the right the remaining events after the mupair rejection cuts have been applied.*

8.2 $\gamma\gamma\mu^+\mu^-$ background

2-photon mupair background is characterised by low showering and tracking energy, low acoplanarity and high acolinearity. Events also have a missing momentum vector pointing along the beam pipe. To select this background, one or more of the two cones was required to have an associated MB/ME segment. The R_{vis} cut at 0.18 is sufficient to ensure that all $\gamma\gamma\mu^+\mu^-$ background events contain at least one muon with enough energy to reach the MB/ME chambers. R_{shw} was required to be less than 0.04 and R_{trk} less than 0.4. To remove a small amount of direct mupair background due to poor tracking in the highly forward region, events were required to have an acolinearity greater than 2°.

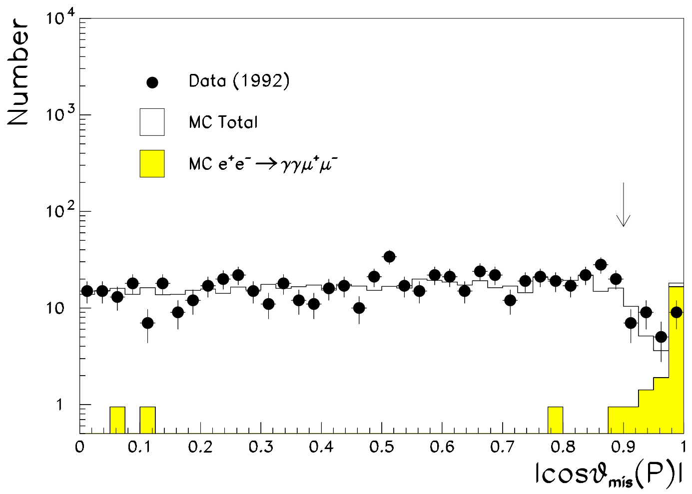

Figure 8.5: $|\cos\theta_{\text{mis}}|$ *for events with a single muon tag, tracking energy less than 0.4 and showering energy less than 0.04.*

Figure 8.5 shows the missing momentum vector $|\cos\theta_{\text{mis}}|$ distribution with all cuts applied. The data to Monte Carlo ratio in the region $|\cos\theta_{\text{mis}}| > 0.9$ agrees at the 1.1σ level corresponding to a data deficit of $(0.03\pm0.02)\%$. The selection efficiency for this background was found to be $(66.7 \pm 5.8)\%$, hence we quote a correction to the taupair acceptance to account for simulation of the $\gamma\gamma\mu^+\mu^-$ background of:

$$f = 1.0000 \qquad \Delta f/f = 0.0004$$

where the error of 0.04% was taken as the observed deficit expanded for the finite efficiency. The $\gamma\gamma\mu^+\mu^-$ background fraction was thus determined to be $(0.11\pm0.04)\%$ where we have conservatively included the Monte Carlo statistics error.

8.3 Bhabha background

Bhabha events enter the sample due to their tendency to shower in the $\sim 0.05\,X_0$ of material preceeding CJ or in the $\sim 0.1\,X_0$ of material that comprises the CJ anode and cathode planes.

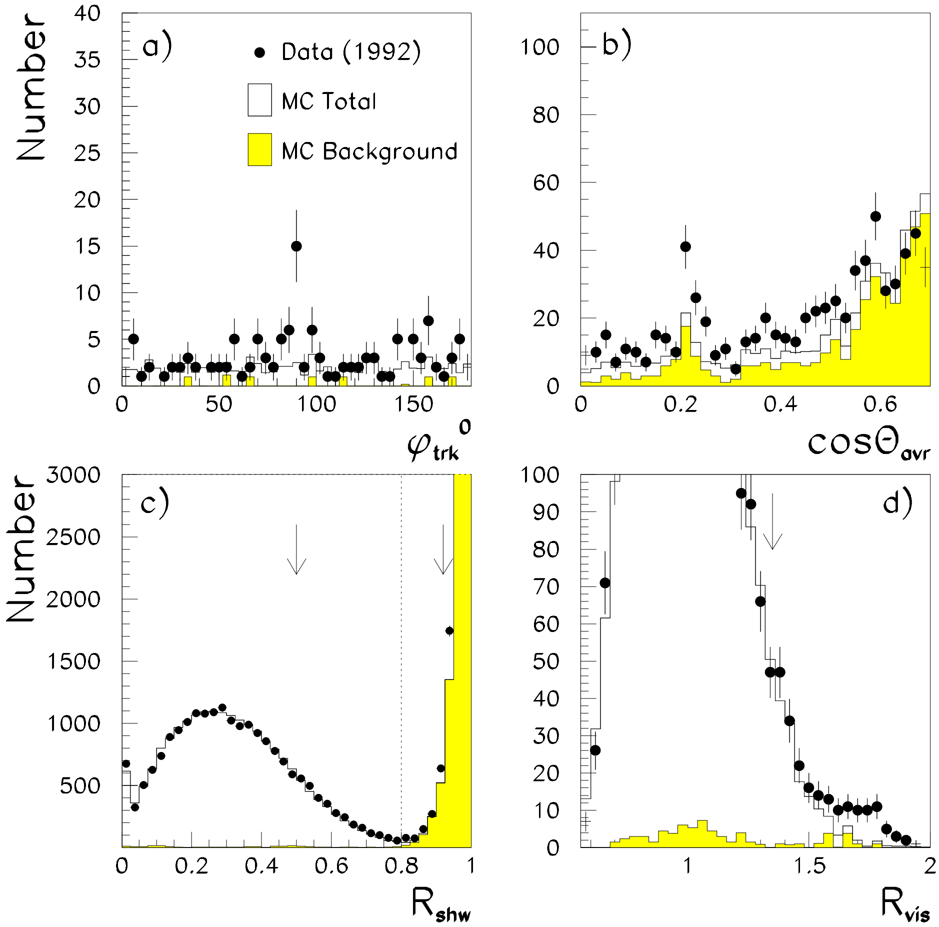

Figure 8.6: *Plot a) shows the $\phi_{\rm trk}$ distribution for events with $0.5 < R_{\rm shw} < 0.8$, plot b) the $|\cos\theta_{\rm avr}|$ distribution for events with $0.5 < R_{\rm shw} < 0.9$, plot c) the $R_{\rm shw}$ distribution and plot d) the $R_{\rm vis}$ distribution for selected taupair events with $R_{\rm shw} > 0.5$. All plots are for barrel events alone.*

8.3.1 Bhabha background in the Barrel

Bhabha events are removed from the taupair sample in the barrel by the $R_{\rm shw} < 0.8$ cut. To examine the Monte Carlo prediction for the amount of background present in the selection, events with $R_{\rm shw} > 0.5$ were examined. A data excess was seen at high visible energy, a cut of $R_{\rm vis} > 1.35$ being made to select these events.

Figures 8.6 c) and d) show the $R_{\rm shw}$ and $R_{\rm vis}$ distributions showing the selection cuts and highlighting the data excess past $R_{\rm vis} = 1.5$. Figure 8.6 a) shows the geometrical distribution in $\phi_{\rm trk}$ (ie. the track angle in the $r - \phi$ plane) for events with $R_{\rm shw} < 0.8$ and $R_{\rm vis} < 1.35$, events with $\phi_{\rm trk} > 180^\circ$ being folded into the top half of the detector. A clear spike at 90° can be seen due to gaps between EB modules, these being unsimulated by the Monte Carlo. Some of the excess away from the peak was found to be due to similar θ boundaries, this being shown in figure 8.7 b) where the cut at $R_{\rm shw} < 0.8$ has been relaxed to $R_{\rm shw} < 0.9$ to make the peaks at approximately $|\cos\theta_{\rm avr}| = 0.2$ and $|\cos\theta_{\rm avr}| = 0.6$ more statistically significant for visualisation purposes.

A data excess of $(0.26 \pm 0.06)\%$ was observed for events satisfying the above cuts necessitating a correction to the taupair acceptance of:

$$f = 0.9974 \qquad \Delta f / f = 0.0006$$

where the error of 0.06% assumes a 100% efficiency for selecting the EB module boundary background excess.

8.3.2 Bhabha background in the endcap

In the endcap, there are effectively three taupair selection cuts which remove $e^+e^- \to e^+e^-(\gamma)$ events from the signal, namely:

- $R_{\rm shw} < 0.8$ for $R_{\rm trk} < 0.25$,
- $R_{\rm vis} < 1.05$ for $0.25 < R_{\rm trk} < 0.8$ and

- $R_{\rm shw} < 0.25$ for $R_{\rm trk} > 0.8$.

The last cut ensures that mupair events undergoing moderate final state radiation outside the MB/ME acceptance appear as background in the taupair sample, any unchecked systematic effects in the level of this background hence cancelling in the lineshape fit assuming lepton universality.

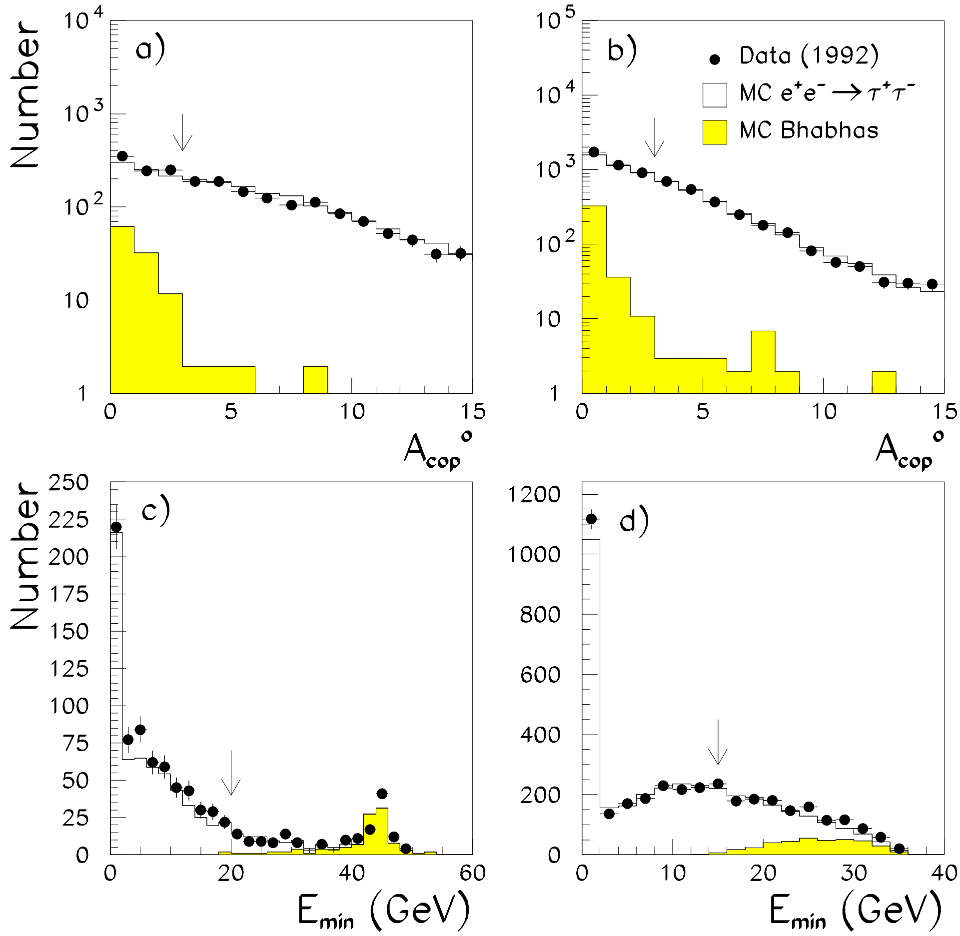

Figure 8.7: *a) and b) show the Acoplanarity distributions for the tracking regions* $0.0 < R_{\rm trk} < 0.25$ *and* $0.25 < R_{\rm trk} < 0.8$ *respectively with* $E_{\rm min}$ *cuts applied. c) and d) show the* $E_{\rm min}$ *distributions with the Acoplanarity cuts applied.*

Bhabha background entering the taupair sample via each of the three cuts was checked by examining each distribution for the appropriate tracking energy window. For events with $R_{\rm trk} < 0.25$, taupair events were removed from the sample by requiring the track acoplanarity of events to be less than 3° and both cones to have calorimetric energies in excess of 20 GeV. Figure 8.7 a) shows the acoplanarity distribution and figure 8.7 c) the $E_{\rm min}$ distribution with the acoplanarity cut applied for selected events with $R_{\rm trk} < 0.25$ and the $R_{\rm shw}$ cut removed. $E_{\rm min}$ is the calorimetric energy of the least energetic cone. $(75 \pm 15)\%$ of the MC Bhabha events below $R_{\rm shw} = 0.8$ were retained by the cuts whilst the signal was reduced to $(2.8 \pm 0.1)\%$ of the original amount.

Similarly for events with $0.25 < R_{\rm trk} < 0.8$, the background to signal ratio was increased by requiring the tracking acoplanarity to be less than 3° and $E_{\rm min}$ to be greater than 15 GeV. Figure 8.7 b) shows the acoplanarity distribution and figure 8.7 d) the $E_{\rm min}$ distribution with the acoplanarity cut applied for events with $R_{\rm shw} < 0.8$. $(85.7 \pm 7.6)\%$ of the background was retained by the application of these cuts whilst the signal was reduced to $(9.1 \pm 0.1)\%$ of its original value.

No signal reduction cuts were required for events with $R_{\rm trk} > 0.8$ as the signal was found to be sufficiently low close to the $R_{\rm shw} < 0.25$ cut, however only events inside the MB/ME acceptance were considered so as to remove the mupair background due to moderate final state radiation from the accepted events. This reduced the taupair signal in this region to approximately $(81.1 \pm 2.4)\%$ of its original value. No Monte Carlo Bhabha events were found to lie in this tracking energy window with $R_{\rm shw} < 0.25$.

Figure 8.8 shows the visible energy distributions for three regions of $|\cos\theta_{\rm avr}|$ for the tracking energy window $0.25 < R_{\rm trk} < 0.8$. The correction factors and uncertainties for each distribution are summarised in table 8.3, background selection efficiencies having been taken into account.

Monte Carlo simulation is excellent for the regions $0.7 < |\cos\theta_{\rm avr}| < 0.77$ and $0.77 < |\cos\theta_{\rm avr}| < 0.83$, data excess/deficit for the two regions being $(0.04 \pm 0.05)\%$ and $(0.00 \pm 0.05)\%$ respectively. For the highly forward region $0.83 < |\cos\theta_{\rm avr}| < 0.9$ however, an excess of $(0.11 \pm 0.05)\%$ (2.1σ) can be seen. An error of 0.14% was therefore applied to account for this discrepancy, the background acceptance of 85.7% being taken into account.

Figures 8.9 a) and b) show the $R_{\rm shw}$ distributions for selected events with $R_{\rm trk} < 0.25$ and $R_{\rm trk} > 0.8$ respectively. Data to Monte Carlo ratios for events inside the taupair acceptance are summarised in Table 8.3 and demonstrate excellent Monte Carlo simulation.

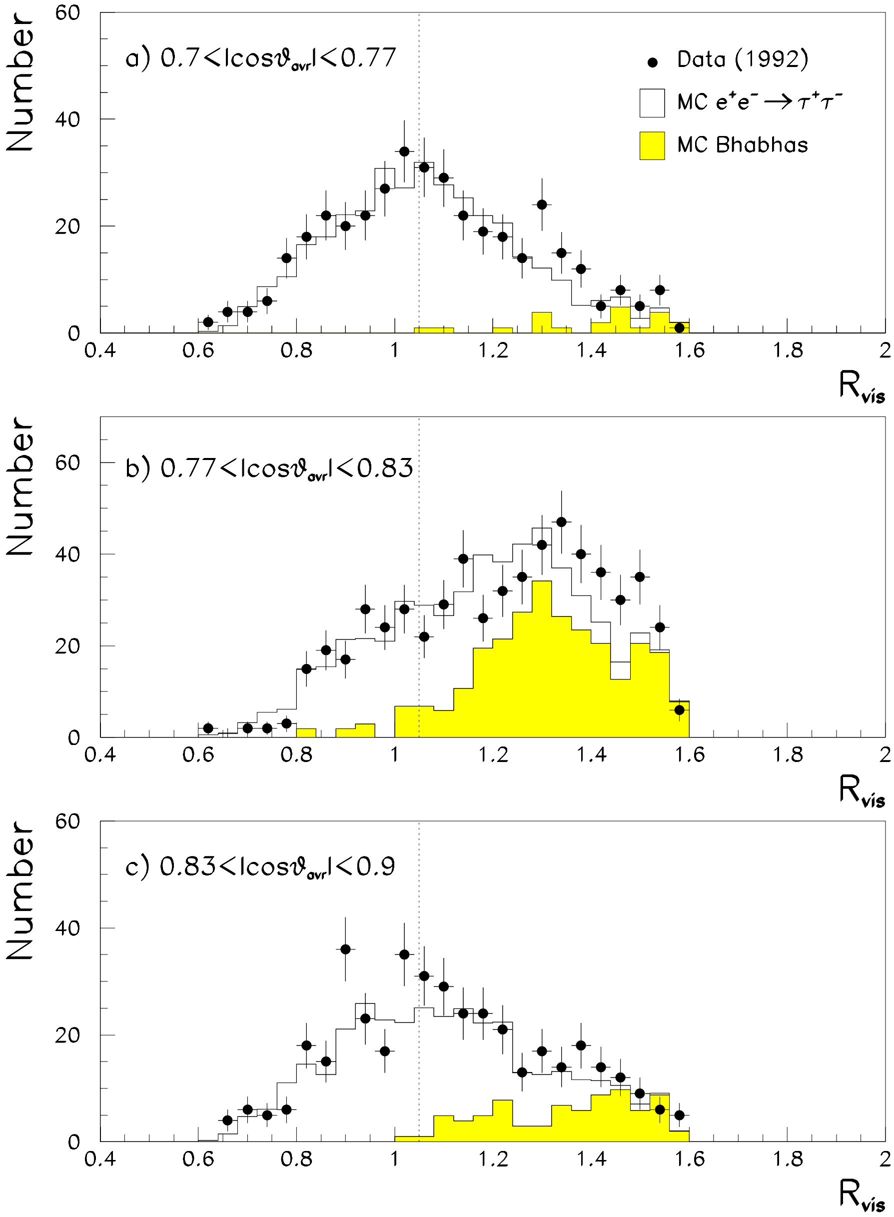

Figure 8.8: *Visible energy distributions for the Bhabha enhanced sample in the geometrical regions a) $0.7 < \cos\theta_{\rm avr} < 0.77$, b) $0.77 < \cos\theta_{\rm avr} < 0.83$ and c) $0.83 < \cos\theta_{\rm avr} < 0.9$ for the tracking region* $0.25 < R_{\rm trk} < 0.8$.

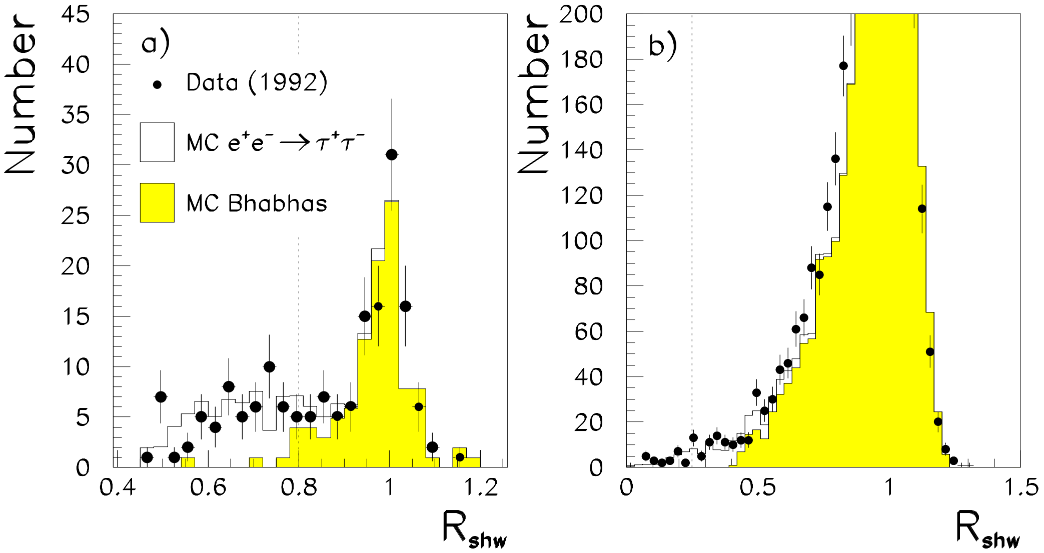

Figure 8.9: *$R_{\rm shw}$ plots for Bhabha background enhanced samples in the tracking energy windows a) $R_{\rm trk} < 0.25$ and b) $R_{\rm trk} > 0.8$.*

Bhabha Background Study		
$\tau^+\tau^-$ Selection Cut	Correction Factor	Uncertainty [%]
MC (Raw)	0.9985	0.024
Barrel $R_{\rm shw}$ cut	0.9974	0.056
Endcap $R_{\rm shw}$ cut ($R_{\rm trk} < 0.25$)	1.0000	0.014
Endcap $R_{\rm vis}$ cut ($0.25 < R_{\rm trk} < 0.8$)		
$0.70 < \lvert\cos\theta_{\rm avr}\rvert < 0.77$	1.0000	0.038
$0.77 < \lvert\cos\theta_{\rm avr}\rvert < 0.83$	1.0000	0.000
$0.83 < \lvert\cos\theta_{\rm avr}\rvert < 0.90$	1.0000	0.109
Endcap $R_{\rm shw}$ cut ($R_{\rm trk} > 0.8$)	1.0000	0.009
Total correction factor	**0.9959**	**0.132**

Table 8.3: *Correction factors and systematic errors associated with Bhabha background for different geometrical and cutting regions.*

8.3.3 Taupair loss

As with the mupair identification checks, the loss of taupair signal to the tracking and calorimetric energy cuts designed to reduce Bhabha background was examined by investigating the relevant distributions after application of background reduction cuts.

8.3.4 Taupair loss in the barrel

The high tail of the $R_{\rm shw}$ distribution is populated by Bhabha and taupair events where the tau leptons have decayed to electrons or ρ^- mesons where the ρ^- has subsequently decayed to one charged and one neutral pion, the π^0 decaying electromagnetically and carrying most of the tau lepton's energy in the lab frame.

Taupair signal loss to the $R_{\rm shw} > 0.8$ cut in the Barrel was investigated by removing the $R_{\rm shw}$ cut and requiring selected events to have a value of $E_{\rm min}$ less than 38 GeV, a tracking acoplanarity greater than 0.5°, and a value of $R_{\rm vis}$ less than 1.65. Figure 8.10 shows the Bhabha depletion cut distributions, each with the other cuts applied. $(61.6 \pm 2.1)\%$ of Monte Carlo taupair events outside the acceptance cut ($R_{\rm shw} > 0.8$) were retained whilst the Bhabha signal was reduced to $(0.03 \pm 0.01)\%$ of its original amount. Figure 8.10 d) shows the $R_{\rm shw}$ distribution highlighting a data excess of $(0.12 \pm 0.04)\%$ in the window $0.8 < R_{\rm shw} < 0.9$. It is not clear whether the excess is due to genuine excess taupair loss, to excess Bhabha events outside the cut or simply a statistical fluctuation, hence we quote the discrepancy as a conservative systematic error expanded for the finite selection efficiency:

$$f = 1.0000 \qquad \Delta f/f = 0.0019.$$

8.3.5 Taupair loss to the Endcap $R_{\rm shw}$ and $R_{\rm vis}$ Cuts

Bhabha signal was reduced for the tracking energy window $R_{\rm trk} < 0.25$ by requiring events to have an acoplanarity greater than 2° and a value of $E_{\rm min}$ less than 40 GeV, distributions being shown in figure 8.11. $(62.2 \pm 3.7)\%$ of the taupair signal outside the taupair selection cut of $R_{\rm shw} < 0.8$ was retained whilst Bhabha events

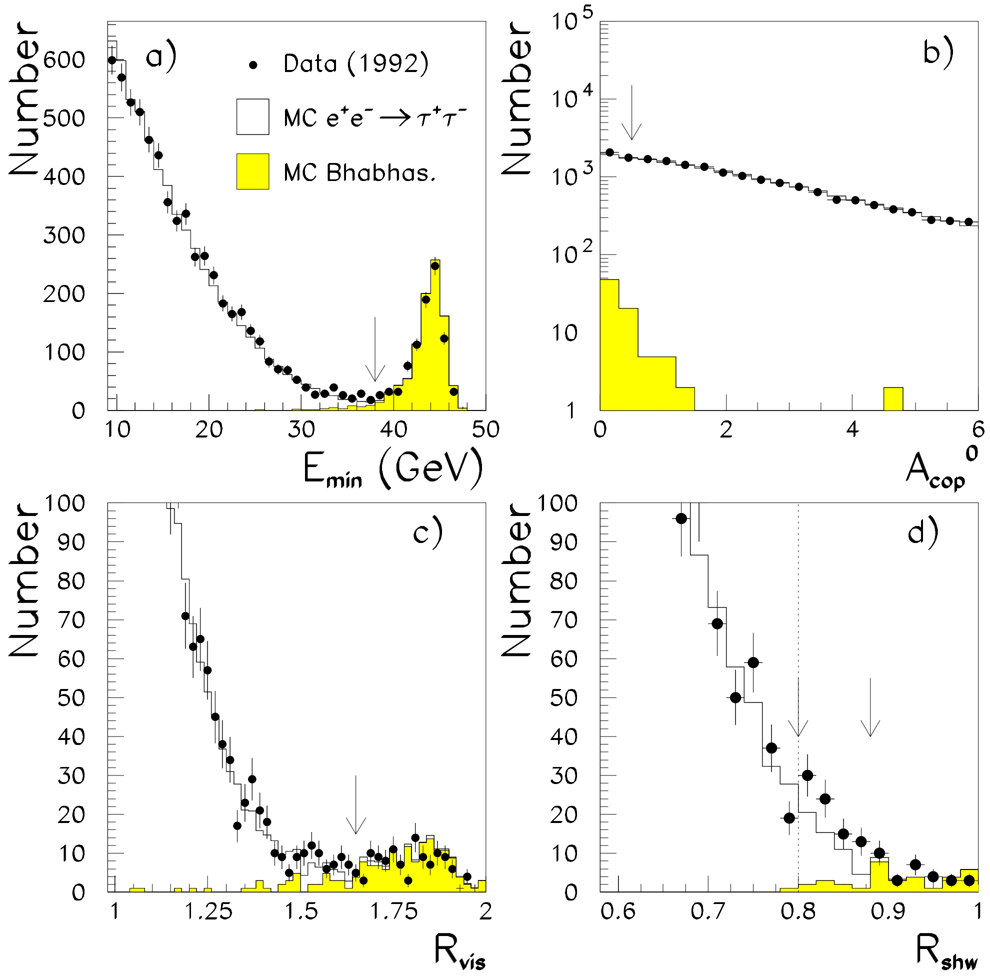

Figure 8.10: *Taupair loss to the R_{shw} cut in the Barrel. Plot a) shows the E_{min} distribution, plot b) the acoplanarity distribution and plot c) the R_{vis} distribution ,each with the other cuts applied. Plot d) shows the R_{shw} distribution after all cuts.*

were reduced to $(5.1 \pm 2.1)\%$ of their original amount. Bhabha events in the tracking energy window $0.25 < R_{\mathrm{trk}} < 0.8$ were reduced by requiring R_{shw} to be less than 0.75 and the acoplanarity to be greater than $1°$, cut distributions being shown in figure 8.12. $(60.2 \pm 0.6)\%$ of the taupair signal outside the taupair selection cut of $R_{\mathrm{vis}} < 1.05$ was retained whilst the Bhabha signal was reduced to $(0.35 \pm 0.08)\%$ of its original

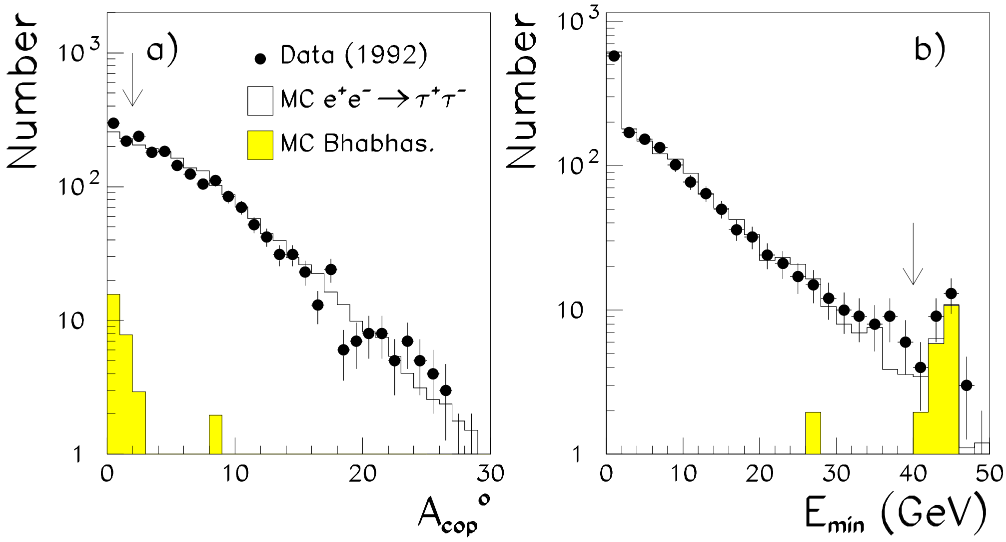

Figure 8.11: *Endcap cut distributions for Bhabha reduction in the region $R_{\rm trk} < 0.25$. The acoplanarity distribution is shown with the $E_{\rm min}$ cut applied and vice versa.*

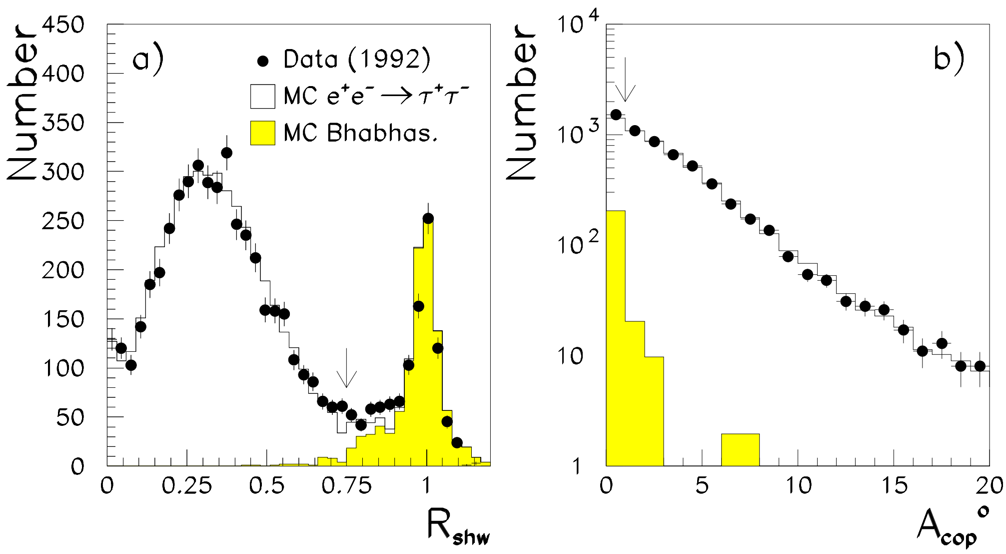

Figure 8.12: *Endcap cut distributions for Bhabha reduction in the region $0.25 < R_{\rm trk} < 0.8$. The $R_{\rm shw}$ distribution is shown with the acoplanarity cut applied and vice versa.*

amount. For events with $R_{\mathrm{trk}} > 0.8$, the Bhabha signal was reduced by requiring the event acoplanarity to be greater than 0.2° and E_{min} to be less than 20 GeV. Figure 8.13 shows the relevant distributions. $(53.2 \pm 1.4)\%$ of the signal was retained for $R_{\mathrm{shw}} > 0.25$ whilst the Bhabha peak was reduced to $(0.11 \pm 0.03)\%$ of its original value.

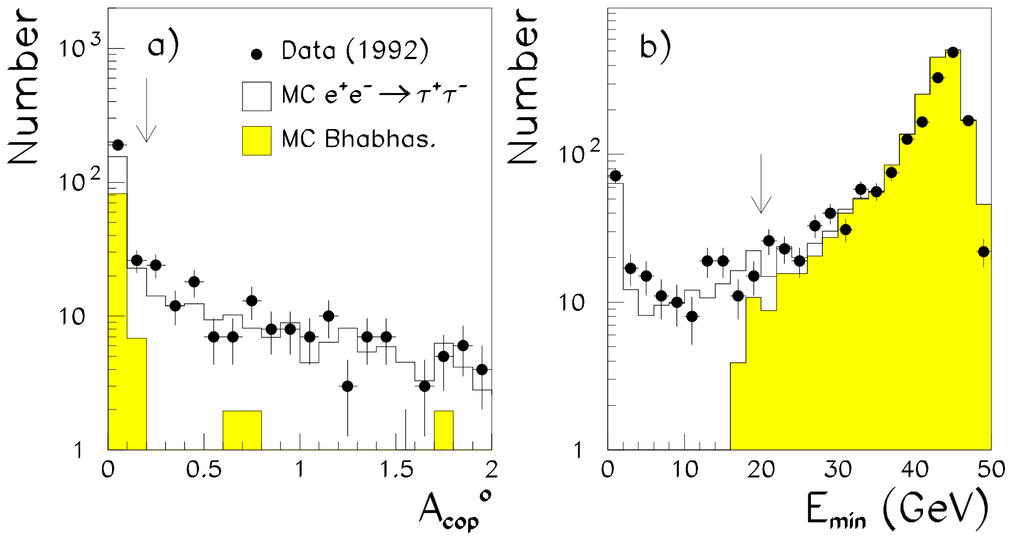

Figure 8.13: *Endcap cut distributions for Bhabha reduction in the region $R_{\mathrm{trk}} > 0.8$. The acoplanarity distribution is shown with the E_{min} applied and vice versa.*

R_{shw}, R_{vis} Cut Acceptance Correction		
$\tau^+\tau^-$ Selection Cut	Correction Factor	Uncertainty [%]
Barrel R_{shw} cut	1.0000	0.19
Endcap R_{shw} cut ($R_{\mathrm{trk}} < 0.25$)	1.0000	0.06
Endcap R_{vis} cut ($0.25 < R_{\mathrm{trk}} < 0.8$)	1.0000	0.09
Endcap R_{shw} cut ($R_{\mathrm{trk}} > 0.8$)	1.0000	0.03
Total correction factor	**1.0000**	**0.22**

Table 8.4: *Correction Factors and systematic errors associated with taupair loss to the Bhabha reduction cuts for various geometrical and cutting regions.*

No significant data excess or deficit was observed for events with tracking energy $R_{\rm trk} > 0.25$, values corrected for signal selection efficiency being shown in table 8.4 and the appropriate plots shown in figure 8.14.

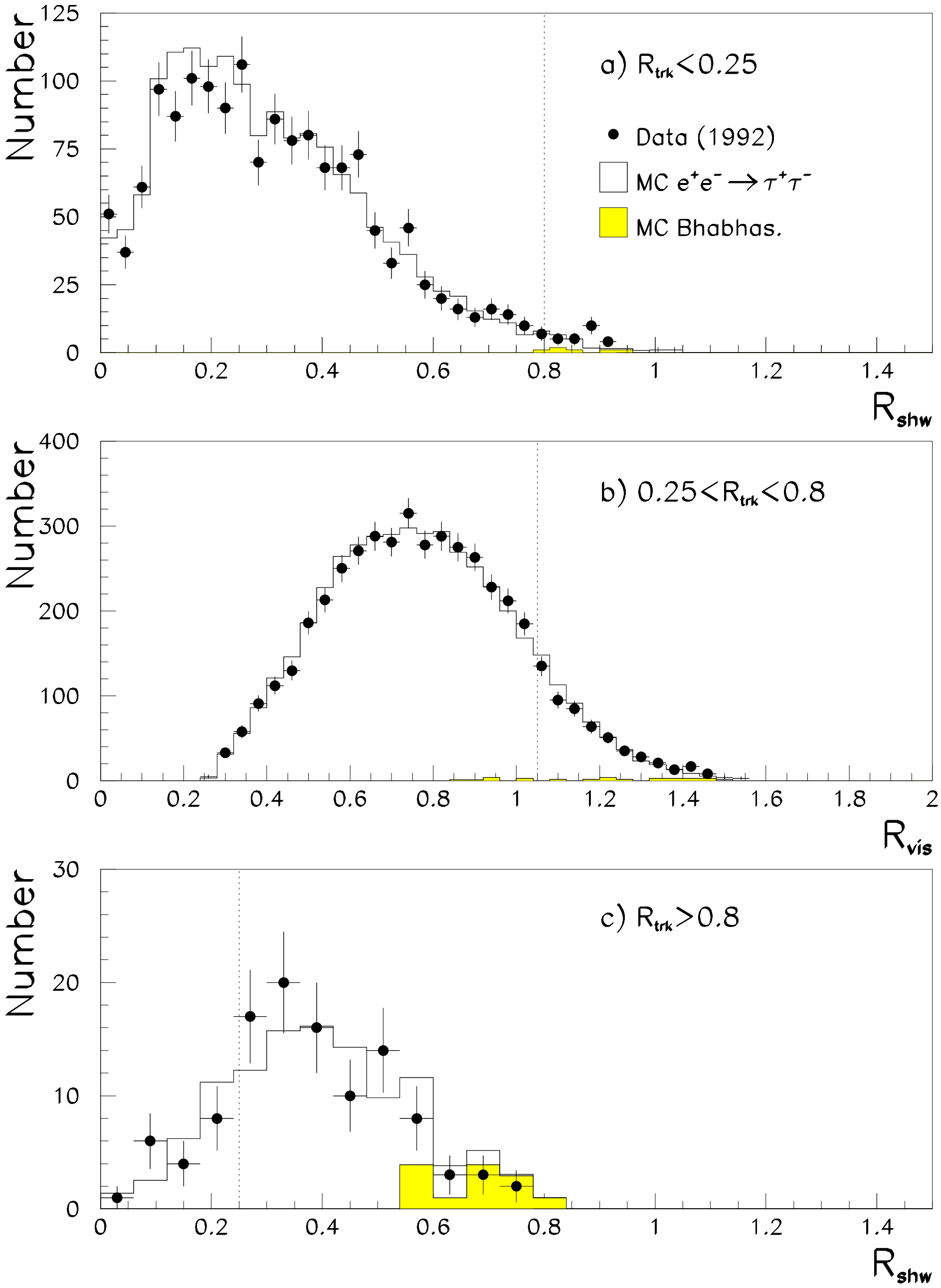

Figure 8.14: *Bhabha reduced cut distributions for the regions a) $0.0 < R_{\rm trk} < 0.25$, b) $0.25 < R_{\rm trk} < 0.8$ and c) $R_{\rm trk} > 0.8$. Dotted lines show the taupair selection cuts.*

A small excess of $(0.04 \pm 0.02)\%$ for the $R_{\text{trk}} < 0.25$ window is most likely to be due to Bhabha events as data/Monte Carlo agreement inside the taupair acceptance excellent. Nevertheless, we associate an efficiency corrected systematic error of 0.06% with this excess.

8.4 $\gamma\gamma e^+e^-$ Background

2-photon electron pair background, like 2-photon mupair background is characterised by low tracking and showering energy, low tracking acoplanarity, high acolinearity and a missing momentum vector pointing along the beam pipe. The fact that the electrons shower however means that this type of event has an increased chance compared with two-photon mupair events of passing the lower visible energy cut.

Events were selected if each cone had an E/P of no more than 1.3 and no less than 0.6 (where E is the associated ECAL energy and P the total tracking energy of the cone), a total tracking energy of no more than 0.25 and a tracking acoplanarity of less than 5°. Figure 8.15 shows the relevant cutting variables, each with all other cuts applied. Plot e) shows the missing momentum cosine after all cuts. Monte Carlo simulation for events with $|\cos\theta_{\text{mis}}| > 0.9$ is modelled to 0.006% (0.24σ) demonstrating excellent simulation. The efficiency for selecting this background was found to be $(38.7 \pm 3.8)\%$; we therefore quote an efficiency corrected systematic error of 0.02% associated with this background. The resulting 2-photon electron pair background was thus determined to be $(0.34 \pm 0.3)\%$.

8.5 4-Fermion Background

Background from 4-fermion (LLV) events was estimated using FERMISV Monte Carlo [77] for the channels listed in table 8.5. Shown are the generator cross sections, background fractions and uncertainties. The dominant modes were found to be the $ee\tau\tau$ channel contributing a background of $(0.036 \pm 0.002)\%$ and the $\mu\mu\tau\tau$ channel at the level of $(0.012 \pm 0.001)\%$. The total background level was predicted to be $(0.066 \pm 0.003)\%$ which was small enough to warrant no further

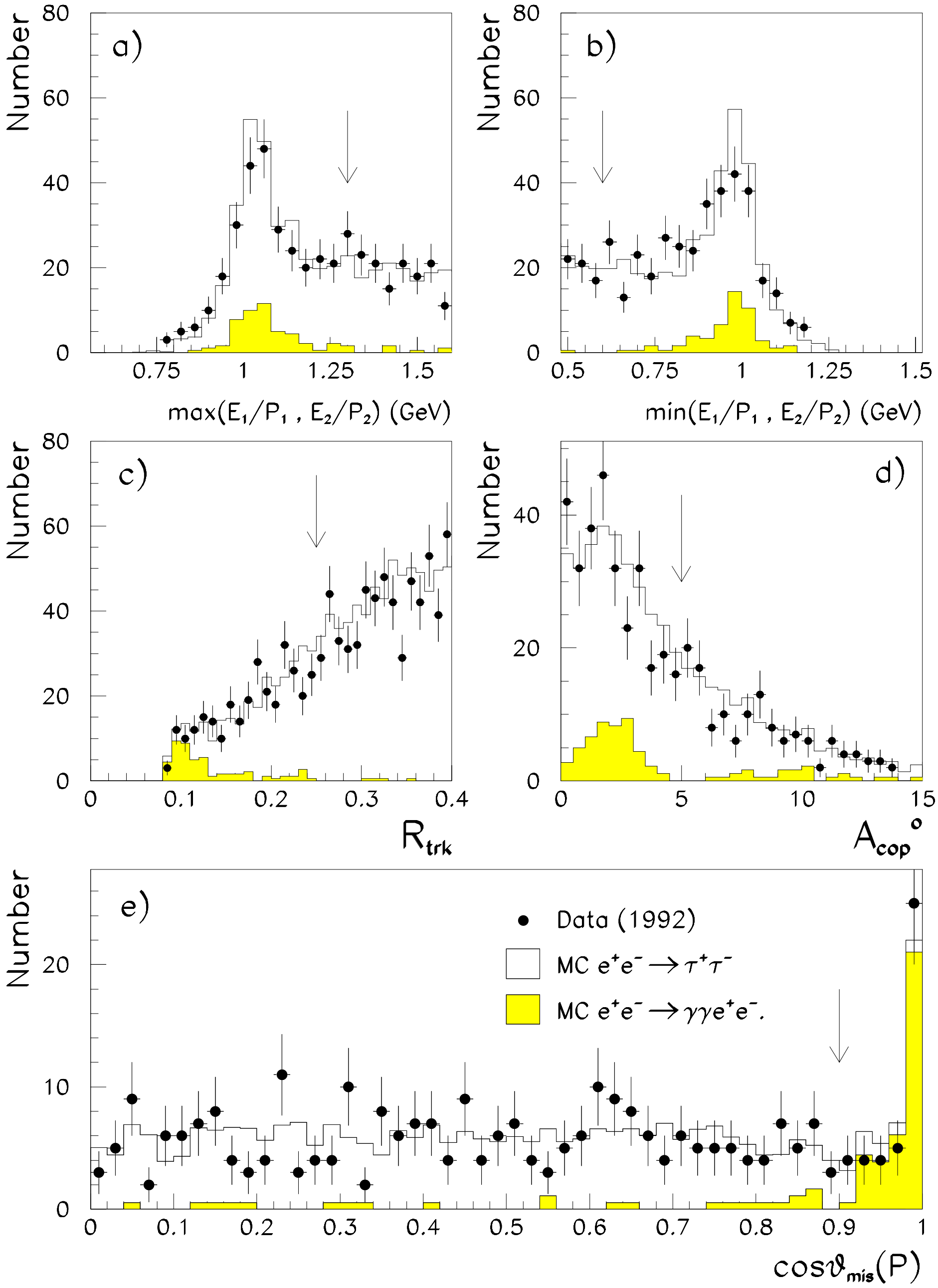

Figure 8.15: *Distributions for $\gamma\gamma e^+e^-$ enhancement. Plots a) to d) are shown with all other cuts applied and marked by arrows. Plot e) shows the cosine of the missing momentum vector for the selected events.*

investigation. To account for the LLV background we quote a correction factor and uncertainty to the taupair acceptance correction of:

$$f = 0.9993 \qquad \Delta f/f = 0.0007$$

where the error is conservatively quoted as the full LLV background fraction.

LLV Background Channels			
LLV Channel	Cross Section **(pb)**	MC Background Fraction [%]	Uncertainty [%]
$eeee$	5.97 ± 0.04	0.0028	0.0006
$ee\mu\mu$	3.99 ± 0.002	0.0072	0.0011
$ee\tau\tau$	1.706 ± 0.008	0.0358	0.0023
$eeu\overline{u}$	5.09 ± 0.01	0.0018	0.0006
$eed\overline{d}$	1.915 ± 0.02	0.0007	0.0003
$\mu\mu\mu\mu$	0.563 ± 0.001	0.0005	0.0003
$\mu\mu\tau\tau$	0.539 ± 0.009	0.0119	0.0011
$\mu\mu u\overline{u}$	1.571 ± 0.007	0.0012	0.0004
$\mu\mu d\overline{d}$	0.593 ± 0.002	0.0004	0.0001
$\tau\tau\tau\tau$	0.5186 ± 0.0001	0.0034	0.0006
$\tau\tau u\overline{u}$	0.673 ± 0.004	0.0001	0.0001
$\tau\tau d\overline{d}$	0.1732 ± 0.0007	0.0000	0.0000
Total Fraction		**0.0657** ±	**0.0030**

Table 8.5: *Raw Monte Carlo prediction for the LLV background fractions of individual LLV channels showing generator cross sections together with the individual background fraction and uncertainty.*

8.6 Multihadronic Background

Multihadronic events were removed from the taupair sample primarily by the cuts on track multiplicity, $N_{\rm trk}$ and total multiplicity, $N_{\rm trk} + N_{\rm cls}$. The low multiplicity tail of the multihadronic signal is therefore responsible for the multihadronic background.

8.6.1 Identification of Multihadronic background

To separate multihadronic events from taupairs both inside and outside the taupair acceptance, events were tagged as multihadronic decays if they had greater than 6 loose OD tracks, greater than 4 normal quality tracks , a value of $\theta_{\rm ISO}$ constructed from clusters of less than 2.9 radians and a value of Ω in excess of 4.5 GeV. Ω is a variable constructed in such a way as to provide a measurement of the fatness of the event, multihadronic events having a much more widely spread topology than taupair events. Ω is given by:

$$\Omega = \sum_{\text{cone } i=1}^{2} \left(\sqrt{(P^i_{\rm INV})^2 + (E^i_{\rm INV})^2}\right)$$

where $E_{\rm INV}$ is the invariant mass constructed from clusters alone. A small amount of taupair events were prevented from being vetoed as multihadronic events by also requiring tagged multihadronic events to have a $\theta_{\rm ISO}$ constructed from tracks of less than 3.05 radians and a value of $E_{\rm INV}$ for the cone with the least track multiplicity in excess of 0.2 GeV.

Figure 8.16 shows the total multiplicity distribution before a) and after b) application of the multihadronic event veto. For the raw distribution, data in the window $15 < N_{\rm trk} + N_{\rm cls} < 22$ is in excess by $(0.23 \pm 0.11)\%$ (2.0σ) as a fraction of the taupair sample for a Monte Carlo predicted multihadronic background of $(60.5 \pm 2.0)\%$ events and for the distribution with the veto turned on a $(0.26 \pm 0.07)\%$ (3.5σ) excess for a multihadronic background of $(29.8 \pm 2.6)\%$. This strongly suggests that the discrepancy is mainly due to poor simulation of the ECAL response for taupair events.

For the events in this region we can write:

$$\frac{\rm N_D - N_{MC}}{\rm N^{MH}_{MC}} = (S_{\rm MH} - 1) + (S_{\tau\tau} - 1)\frac{\rm N^{\tau\tau}_{MC}}{\rm N^{MH}_{MC}} \quad (8.1)$$

where $\rm N_D$ is the amount of selected data, $\rm N_{MC}$ the total amount of Monte Carlo, $\rm N^{\tau\tau}_{MC}$ is the amount of taupair Monte Carlo, $\rm N^{MH}_{MC}$ is the amount of Multihadron Monte Carlo and $S_{\tau\tau}$ and $S_{\rm MH}$ are the factors by which data taupairs and multihadronic events respectively are in excess or deficit.

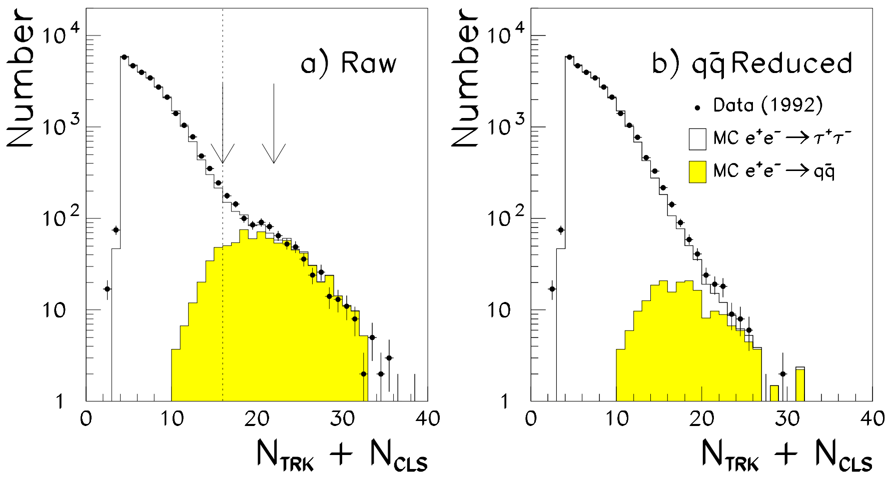

Figure 8.16: *The total multiplicity distribution $N_{TRK} + N_{CLS}$ before and after application of the multihadron veto. Events in the window $15 < N_{\rm trk} + N_{\rm cls} < 22$ were selected to examine the taupair loss due to the $N_{\rm trk} + N_{\rm cls}$ selection cut marked by the dotted line.*

If we now assume that the distributions used to remove multihadronic events from the total multiplicity distribution (figure 8.16 a)) are well simulated in shape by the Monte Carlo, we can apply the multihadronic event veto to events in the window, varying each multihadron selection cut in turn and thus varying the ratio of selected taupair events to multihadronic events. If the assumption is valid, data and Monte Carlo will obey the form of equation 8.1 and a value of $S_{\tau\tau}$ can be extracted. The relevant plots are shown in figure 8.17, each demonstrating linearity. Open points are the values with the multihadronic veto turned on and off using the cuts listed above. Plot e) shows the values of $S_{\tau\tau}$ derived from a least squares fit to each plot together with the simple average of 1.38 ± 0.03. A total error of $^{+0.044}_{-0.028}$ was assigned to $S_{\tau\tau}$ to account for the systematic variation of the derived value from each fit. No account was made for the correlation in the errors assigned to plots a) to d). The value of $S_{\tau\tau} = 1.38^{+0.044}_{-0.028}$ yields a taupair loss of $0.340^{+0.039}_{-0.025}\%$ and hence a correction to the taupair acceptance of:

$$f = 1.0034 \qquad \Delta f / f =^{+0.039\%}_{-0.025\%}$$

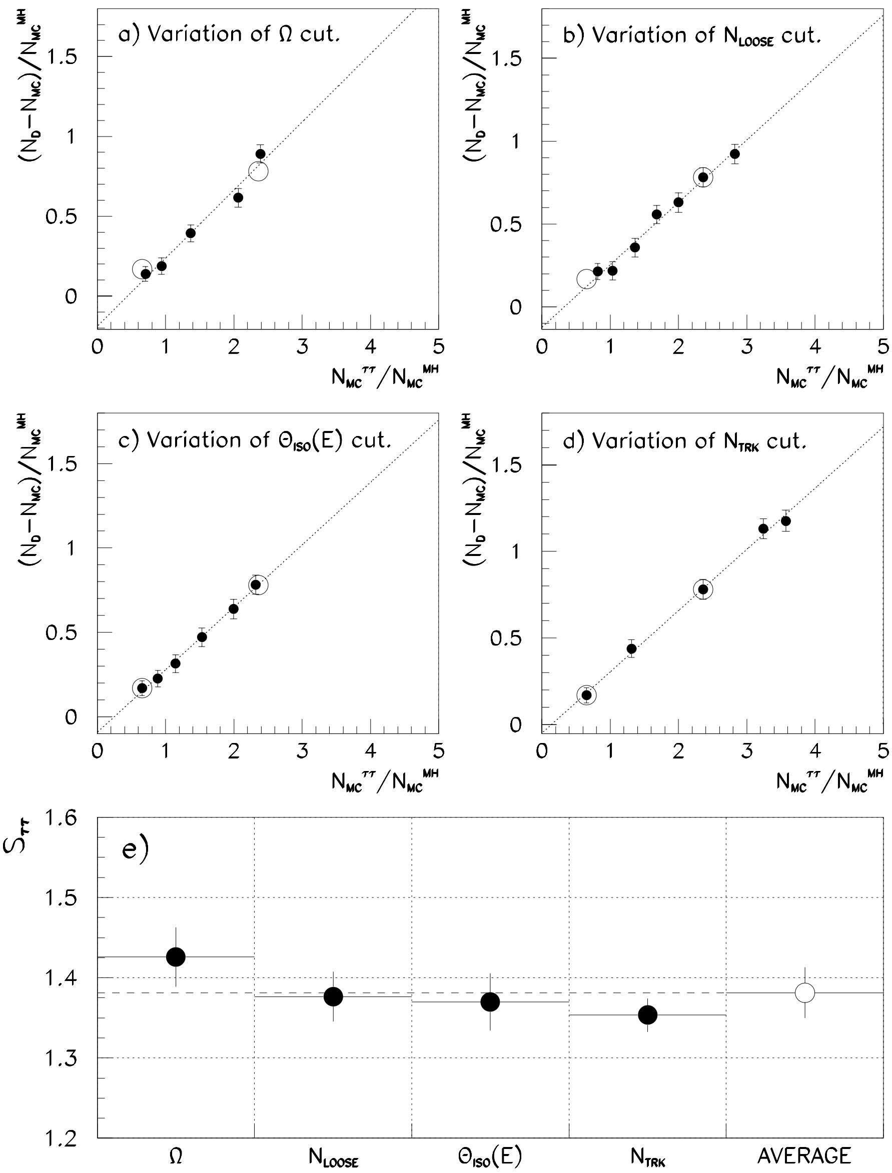

Figure 8.17: *Plots a) to d) show the variation of* $(\mathrm{N_D} - \mathrm{N_{MC}})/\mathrm{N^{MC}_{MH}}$ *versus* $\mathrm{N^{\tau\tau}_{MC}}/\mathrm{N^{MH}_{MC}}$ *for variation of the four multihadron selection cuts in the multiplicity window* $15 < N_{\mathrm{trk}} + N_{\mathrm{cls}} < 22$*. Plot e) shows the values of* $S_{\tau\tau}$ *derived from each plot and the simple average of those values. Open points in plots a) to d) represent the values derived with the multihadron selection turned on and off.*

8.6.2 Multihadronic Background Correction

Multihadronic background is particularly hard to extract from the genuine taupair signal, event signatures looking extremely similar. The simulation of multihadronic background was examined in exactly the same way as for the calculation of the taupair loss, this time by selecting events in the total multiplicity window $11 < N_{\rm trk} + N_{\rm cls} < 16$. JETSET-73 Monte Carlo yielded a value of $S_{\rm MH}$ equal to $0.89^{+0.22}_{-0.10}$ where the errors account for the systematic variation seen in the four fits. The JETSET-73 simulation can therefore be seen to agree well with the data, the difference between corrected and uncorrected background being 0.05%.

As an independent cross check, HERWIG-55 Monte Carlo was used to examine the multihadronic background fraction. HERWIG simulation was found to provide an extremely poor fit to the data in the low multiplicity tail and the background prediction was significantly different at $(0.85 \pm 0.09)\%$ (almost twice that predicted by JETSET-73). After application of the procedure described in section 8.6.1 however, the HERWIG-55 prediction for the level of multihadronic background was rescaled to a level of $(0.55 \pm 0.18)\%$, in good agreement with the JETSET-73 prediction after the same procedure.

The difference between the corrected HERWIG-55 and JETSET-73 predicted backgrounds was found to be 0.08% ie. of the same order as the systematic uncertainty from the four JETSET-73 fits. The JETSET-73 corrected value is therefore believed to be safe and we take the HERWIG-JETSET difference of 0.08% as the error on the multihadronic background fraction.

A similar check on the taupair loss using HERWIG gave a taupair loss correction factor $S_{\tau\tau} = 1.26 \pm 0.16$ in excellent agreement with the JETSET prediction.

8.7 Geometrical Acceptance Systematic Errors

Accurate determination of the geometrical acceptance for taupair events is vital in the calculation of the taupair production cross section. The choice of acolinearity, $|\cos\theta_{\rm avr}|$ and barrel edge cuts together with the choice of definition for

$|\cos\theta_{\rm avr}|$ were therefore all checked in detail.

8.7.1 The acolinearity cut

The acolinearity cut at 15° is effective at suppressing 2-photon and Bhabha background which has undergone heavy initial state radiation together with badly tracked multihadronic decays. To examine the systematic effect upon the taupair acceptance correction associated with the choice of acolinearity cut, the distribution was examined after removing events identified as $\gamma\gamma e^+e^-$ and $\gamma\gamma\mu^+\mu^-$ by the two-photon enhancement checks described in sections 8.2 and 8.4, the removal of events tagged as Bhabha background at the EB module boundaries (section 8.3.1) and the removal of mupair background due to poor tracking (section 8.1.3). Monte Carlo was used to calculate a sensible amount by which the acolinearity cut should be varied by calculating an acolinearity resolution based upon the difference between the measured event acolinearity and the acolinearity determined from the TREE momenta of the tau primary decay particles ie. the ρ^-,a_1^-,μ^-,e^-,π^-,K^- or $K^*(892)$ momenta. The Monte Carlo resolution was found to be 1.334°. This value can be considered a strict upper bound to the acolinearity resolution as final state radiation was not taken into account. The acolinearity cut was varied by $\pm 1.35°$ and the maximum change in the ratio of data to Monte Carlo found to be 0.05%, no significant variation being seen outside of that expected due to variation in statistics.. We therefore quote a correction to the taupair acceptance of:

$$f = 1.0000 \qquad \Delta f/f = 0.0005$$

to account for the choice of acolinearity cut.

8.7.2 The $|\cos\theta_{\rm avr}|$ acceptance edge cut

Similarly, a resolution for the $|\cos\theta_{\rm avr}|$ parameter was determined using Monte Carlo and found to be 0.012. Again, this can be considered an upper bound. The $|\cos\theta_{\rm avr}|$ cut was varied by $\pm 4\sigma$ yielding a maximum change in the ratio of data to Monte Carlo of 0.17%; hence we quote an acceptance correction of:

$$f = 1.0000 \qquad \Delta f/f = 0.0017 \ .$$

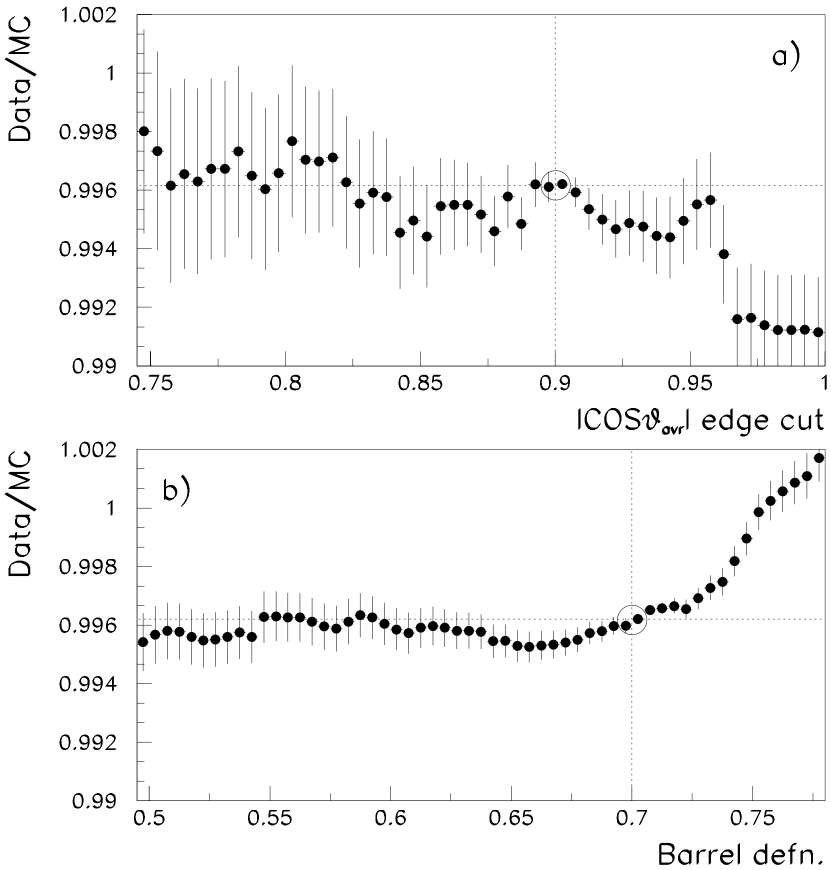

Figure 8.18: *Plot a) shows the variation of N_{data}/N_{MC} for variation of the barrel edge definition and plot b) variation of the acceptance edge cut.*

Figure 8.18 a) shows the variation with cut value of the ratio of selected data to Monte Carlo. Only above approximately $|\cos\theta_{\rm avr}| = 0.95$ did a significant departure from the Monte Carlo prediction occur due to degradation of tracking and track trigger efficiency in that region. Error bars represent the statistical error due to variation in statistics from the cutting point.

8.7.3 Definition of $|\cos\theta_{\rm avr}|$

When defining the geometrical acceptance for taupair events the direction of the taupair was reconstructed using the vectoral difference of the two cone vectors. To examine whether a systematic bias exists due to this method of reconstruction, the ratio of accepted taupair events to Monte Carlo was examined for three other definitions, namely the thrust axis, the vectoral difference of the two cone tracking momentum vectors and the vectoral difference of the two cone ECAL cluster momentum vectors. Results are shown in table 8.6. Only the acceptance using clusters shows a variation outside 1σ of the statistical error, having a data to Monte Carlo ratio 0.07% below that for the chosen definition of $|\cos\theta_{\rm avr}|$. We therefore quote a correction to the taupair acceptance of:

$$f = 1.0000 \qquad \Delta f/f = 0.0007 \; .$$

$\|\cos\theta_{\rm avr}\|$ Definition Systematics		
Method	$\|1-{\rm Data/MC}\|\times 100$	Δ(Data/MC) [%]
Average of clusters and tracks	0.000	0.000
Thrust axis	0.013	0.005
CT tracks only	0.018	0.020
ECAL clusters only	0.066	0.044

Table 8.6: *Systematic errors associated with the choice of definition for* $|\cos\theta_{\rm avr}|$.

8.7.4 Barrel edge definition

Definition of the barrel edge is required by the endcap $R_{\rm vis}$ cut to reduce Bhabha background in that region. The Monte Carlo estimate of the $|\cos\theta_{\rm avr}|$ resolution in the region of the cut was found to be 0.021. The cut at 0.7 was chosen so as to provide maximum statistics whilst rejecting events in the pressure vessel region of the detector as the Monte Carlo simulation was found to be poor for this region. Simulation of the acceptance was found to be stable for values of the barrel edge below 0.7, however for values above 0.7, Bhabha events in the data were found to shower more than the Monte Carlo prediction causing the steep rise in figure 8.18 b).

As this effect was understood, the cut was only varied between the values 0.616 and 0.721 (-4σ and $+1\sigma$). The maximum change in the ratio of data to Monte Carlo yielded a systematic error of 0.10%:

$$f = 1.0000 \qquad \Delta f/f = 0.0010 \ .$$

8.7.5 Choice of cone angle

Events can fail the cone multiplicity cut due to widely spread toplogies (characteristic of multihadronic events) or because of highly isolated high energy clusters which carry most of the hemispheres energy. The cone angle was thus varied by $\pm 5^{\circ}$ from its nominal 35° setting. The maximum variation in the ratio of data to Monte Carlo yielded a systematic error of 0.11%:

$$f = 1.0000 \qquad \Delta f/f = 0.0011 \ .$$

which was marginally greater than that expected due to variation in statistics.

8.7.6 Lower $R_{\rm vis}$ cut

To examine the loss of taupair events to the lower $R_{\rm vis}$ cut at 0.18 after removing events tagged as 2-photons, events were additionally removed from the sample if they had a maximum P_T for the two hemispheres of less than 4 GeV and if the maximum visible energy of the two cones was less than 0.2. These cuts were instrumental in removing $99.33 \pm 0.08\%$ of the remaining two-photon mupair background below an $R_{\rm vis}$ of 0.18 and $99.74 \pm 0.05\%$ of the 2-photon electron pair events. Figure 8.19 a) shows the $R_{\rm vis}$ distribution before application of the cuts with the $R_{\rm vis}$ cut inactive. Figure 8.19 b) shows the distribution if only events with a track multiplicity of 2 are removed. An excess of $2.13 \pm 0.11\%$ exists below the cut. These events had vertex parameters consistent with production at the beam spot and are 2-photon multihadronic events. Currently, there is no 2-photon multihadron Monte Carlo available for general use in the OPAL DST farm, however as the excess is below an $R_{\rm vis}$ of 0.14, the taupair cross section analysis is safe. Any events remaining with a track

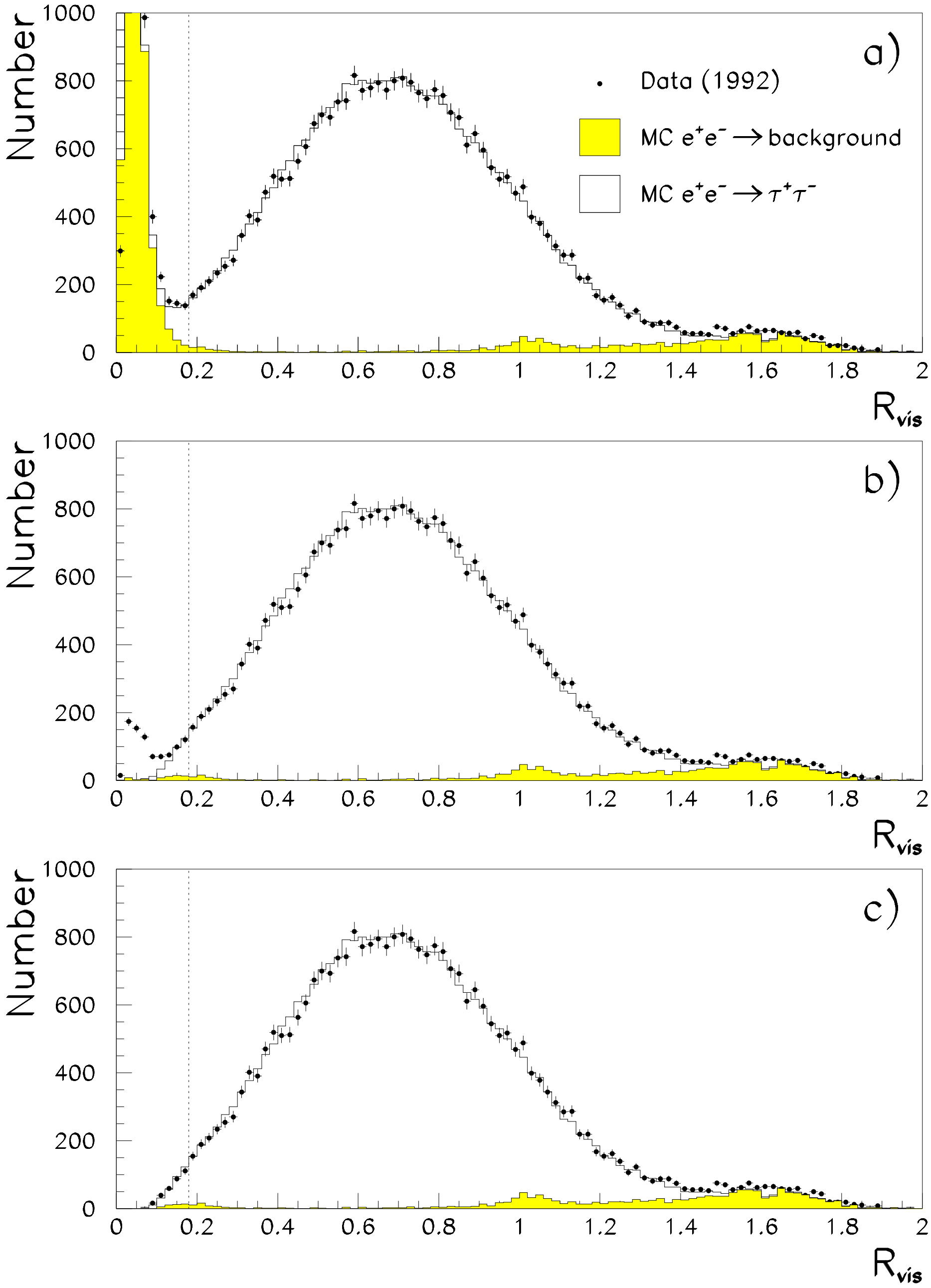

Figure 8.19: *Plot a) shows the visible energy distribution after initially selected 2-photon events have been removed. Plot b) shows the distribution after removal of further 2-photon background with track multiplicity 2. Plot c) shows the distribution after removal of background regardless of multiplicity.*

multiplicity in excess of 2 after application of the R_{vis} and P_T cuts were removed from the sample below an R_{vis} of 0.18 corresponding to two-photon multihadron events not caught by the P_T and maximum visible energy cuts. The data to Monte Carlo ratio below the R_{vis} cut was found to be $0.002 \pm 0.071\%$ (0.03σ) with a taupair selection efficiency of $68.5 \pm 0.8\%$, Monte Carlo agreeing admirably with data. We associate an efficiency corrected systematic error of 0.003% with the taupair acceptance due to this cut:

$$f = 1.0000 \qquad \Delta f/f = 0.0000 \ . \tag{8.2}$$

In the following chapter we shall discuss the determination of the cosmic ray and beam gas background.

Chapter 9

Cosmic Ray, Beam Gas and Beam Wall Interactions

9.1 The cosmic ray veto

Cosmic ray events originate high up in the atmosphere and consist mainly of highly energetic muons. They are screened to some extent by the 100 or so metres of rock above the OPAL detector however the higher energy fraction of the cosmic ray spectrum can, when coincidental with the LEP bunch crossing and OPAL event vertex cause an appreciable background if not dealt with correctly.

Beam gas events occur when an electron within a bunch interacts with a gas particle. These events are hence highly acolinear in nature, do not necessarily have a z-vertex position at zero and are generally low in visible energy.

Cosmic ray events were rejected using a cosmic ray veto which utilised both time of flight and tracking information. TB was used in the barrel to determine whether pairs of tracks in the event were consistent with particles emanating from the beam spot and were in time with the beam crossing. TB hits were required to either have pulse readout at both ends or in the case where only one end was read out, the hit was required to be matched to EB. This insured the suppression of noise hits and the reliable measurement of z for time of flight calculation.

An event was flagged as a TB cosmic if it satisfied any one of the following conditions:

- $10\,\mathrm{ns} < \Delta t < 30\,\mathrm{ns}$ where Δt is the time difference given by taking all TB hits separated in azimuth by more than 165°, subtracting the time of TB hits above the horizontal from hits below the horizontal and finding the pair which gives the minimum modulus of that time difference, hence distinguishing between tracks emanating from the e^+e^- interaction point and cosmic rays passing down through the detector from the upper atmosphere.

- A cosmic ray may only fire one TB counter because it passes through a gap between TB bars, passes through an inefficient counter or because it passes through one of the two TB counters outside the 50 ns TB trigger gate. Hence a cut was made on the minimum absolute firing time t° out of all TB hits in the event (corrected for flight time from the vertex of a $\beta = 1$ particle). t° here was chosen to be positive if it was consistent with the hypothesis that the TB counter that did not fire was struck by a cosmic ray outside the 50 ns gate. This is the case if a TB counter above the horizontal measures a large positive time or a counter below the horizontal a large negative time for a cosmic ray originating in the upper atmosphere. t° was hence multiplied by -1 if it belonged to a TB counter in the lower half of the detector. The event was flagged as a TB cosmic if t° exceeded 10 ns.

- A cosmic ray event may lie completely outside the 50 ns TB gate and hence contain no TB hits at all. Events therefore with no TB hits were automatically flagged as TB cosmic events.

Tracking information was used to examine whether tracks in the event emanated from the beam spot. Tracks satisfying the cosmic ray track quality cuts (table 5.3) were paired up and minimum values of $\mathrm{d0_{min}}$ and $\mathrm{Z0_{min}}$ were found for tracks with an acolinearity angle θ_A such that $\cos\theta_A > 0.95$ where:

$$\begin{aligned}
\mathrm{d0_{min}} &= \min(|\mathrm{d0}|_i + |\mathrm{d0}|_j), \\
\mathrm{Z0_{min}} &= \min(\mathrm{Z0}_k + \mathrm{Z0}_l)
\end{aligned}$$

and i, j, k and l refer to the tracks, d0 is the minimum approach distance of the fitted track to the vertex in the $r-\phi$ plane and Z0 is the unconstrained distance in z of the track at that point.

The cosmic ray veto classifies the event as being in the barrel or endcap using tracking information derived using either CT tracks or CJ tracks without rotation correction if CZ hits were not matched to the track. If both tracks satisfied $\cos\theta < 0.8$ then the event was classified as being in the barrel.

TB and Tracking information were then combined to produce a total cosmic ray veto such that the event was vetoed as a cosmic ray event if it was classified as being in the barrel, classified as a TB cosmic and was classified as a tracking cosmic by:

$$|\mathrm{d0_{min}}| > 0.08\,\mathrm{cm} \quad \mathrm{or} \quad |\mathrm{Z0_{min}}| > 10\,\mathrm{cm}$$

or if it lay in the endcap, was classified as a TB cosmic and satisfied:

$$|\mathrm{d0_{min}}| > 0.6\,\mathrm{cm} \quad \mathrm{or} \quad |\mathrm{Z0_{min}}| > 50\,\mathrm{cm}.$$

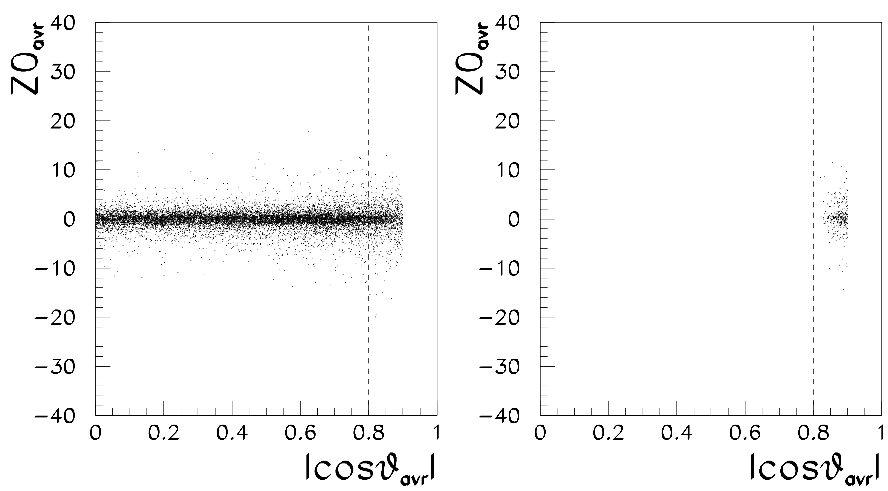

Figure 9.1: $|\cos\theta_{\mathrm{avr}}|$ *Vs.* $Z0_{\mathrm{avr}}$ *for events with and without associated TB hits. The barrel cut at 0.8 can be seen to be safe.*

The cosmic ray veto was only applied to taupair candidates inside the region $|\cos\theta_{\rm avr}| < 0.8$ where TB information is available, hence due to the taupair selection and cosmic ray algorithm definitions of barrel acceptance being almost identical the endcap cosmic ray veto is essentially redundant. [1]

To reject cosmic ray events with $|\cos\theta_{\rm avr}| > 0.8$ together with beam gas events throughout the acceptance, an additional vertex cut was applied using all tracks which pass the track quality cuts (table 5.3). The event was rejected by this additional vertex cut if:

$$|{\rm d0}'_{\rm min}| > 0.5\,{\rm cm} \quad {\rm or} \quad |Z0_{\rm avr}| > 20\,{\rm cm}$$

where $\rm d0'_{min}$ is the minimum approach distance to the vertex of all considered tracks and $\rm Z0_{avr}$ is the weighted average of track Z0's.

Figure 9.1 shows distributions of $|\cos\theta_{\rm avr}|$ versus $Z0_{\rm min}$ for $N_{\rm TB} = 0$ and $N_{\rm TB} > 0$ respectively demonstrating that the definition of the Barrel TB acceptance at 0.8 is sensible.

Tagged cosmic ray events were examined in detail. Their visible energy spectrum was found to be consistent with that expected and the division of events classified as taupair and mupair events as well as being tagged as cosmic rays found to be well defined by the mupair F_{vis} cut at 0.6, hence no cosmic ray background is expected to exist in the taupair sample with visible energies in excess of this amount.

9.2 Estimation of cosmic ray background in the barrel

Barrel cosmic ray candidates were selected by requiring events to have a value of $|\cos\theta_{\rm avr}| < 0.8$ and at least two tracks which had passed the cosmic ray track quality cuts. The cosmic ray background and taupair loss to the cosmic ray veto were

[1] This cut was primarily designed for the mupair analysis to catch events where only one track had traversed TB or a radiated photon was caught. The wider vertex cut was chosen because of poor tracking resolution in the forward region of the detector.

then examined for three possible scenarios; no TB hits, one TB hit and more than one TB hit per event.

9.2.1 Events with no TB hits

Firstly we consider the case for events containing no quality TB hits. Figure 9.2 shows the $d0_{min}$ versus $Z0_{min}$ distribution for such events. Due to the fact that cosmic ray events can be recorded at any time during the TB gate, cosmic ray tracks are displaced in the tracking chambers. By adding the moduli of track d0 values when constructing $d0_{min}$, this leads to an increased separation between cosmic ray events and taupair events. This 'out of time effect' can clearly be seen, only two events from run 3449 lying within the tight vertex cut corresponding to taupair events with poorly reconstructed TB assignment. This low number of events meant that no correction to the taupair loss or level of cosmic ray background due to events with no TB hits was necessary, this observation not being entirely unexpected as TB detector status was required to be 3 for the selected events (table 5.1).

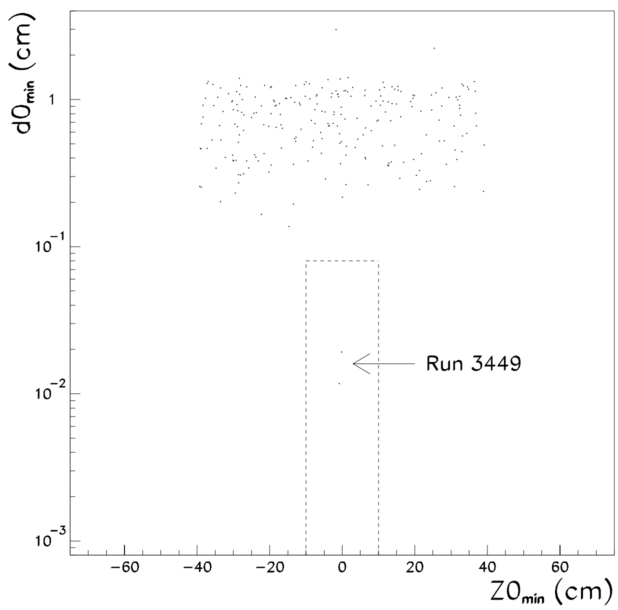

Figure 9.2: *Vertex plot for $N_{\mathrm{TB}} = 0$. The dotted line shows the cosmic ray vertex cut. Only two events lie inside the vertex corresponding to taupair events with inefficient TB assignment.*

9.2.2 Events with one TB hit

Next we consider events containing only one quality TB hit. Figure 9.3 shows the t° distribution of such events together with the vertex distribution. Rejected cosmic ray events (shaded) lie well away from the vertex cut and have t° values consistent with cosmic rays traversing the detector close to the 50 ns gate. One cosmic ray event at high t° fell within the vertex necessitating a negligible correction to the taupair acceptance.

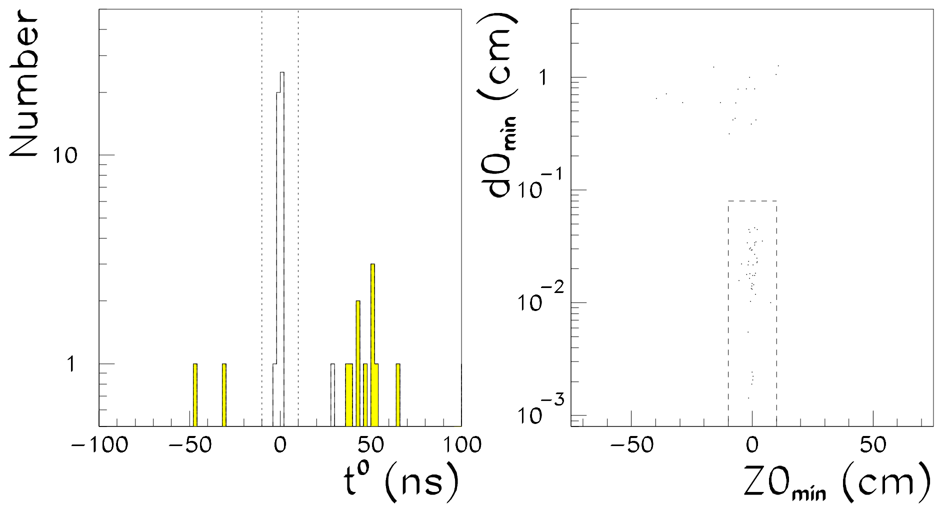

Figure 9.3: *Vertex and t° Plots for $N_{\mathrm{TB}} = 1$. Cosmic ray events lie well separated in the vertex distribution due to the 'out of time effect' as well as the signed t° distribution.*

9.2.3 Events with two or more TB hits

Fig 9.4 shows the Δt distribution for events with $N_{\mathrm{TB}} > 1$ where a pair of back to back TB hits have been found. Shaded events are those that have been vetoed as cosmic rays, the bulk of which lie between the cuts at 10 ns and 30 ns. Figure 9.4 also shows the equivalent distribution for t°. Both sets of cuts are loose, their redundancy meaning that their position is not crucial. Some events in the range $10\,\mathrm{ns} < \Delta t < 30\,\mathrm{ns}$ lay inside the event vertex but can be seen to have t° values consistent with zero. These were found to consist of events with TB inefficiency localised in ϕ. Any taupair events being lost to the cosmic ray veto due to this effect combined with poor vertex measurement would show up as an increased number of rejected events in the zero bin of the t° distribution. No such excess was observed. One cosmic ray event classed as a taupair event was found to lie just to the left of the zero peak in the t° distribution and just at the edge of the vertex cut. This necessitated a minor correction to the taupair acceptance.

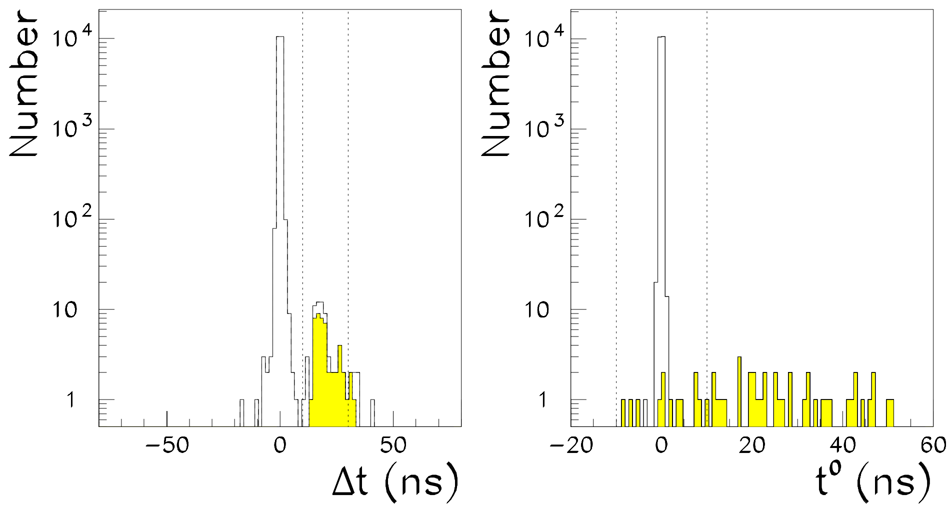

Figure 9.4: *Δt and t° distributions for events with a measured Δt. Events not classified as cosmic rays but having a Δt in the range $10\,\mathrm{ns} < \Delta t < 30\,\mathrm{ns}$ all lie in the vertex and have t° values consistent with zero.*

The redundancy of the Δt and t° distributions highlight the fact that in the absence of TB faults, no significant corrections need to be made to the taupair acceptance due to the effect of the cosmic ray veto in the barrel.

9.2.4 Taupair loss to the additional vertex cut

In the barrel, the additional vertex cut was responsible for rejecting three taupair events and no cosmic ray events, these events all being tagged by the cosmic ray finding algorithm.

For the 1992 data therefore, the cosmic ray background correction was determined to be:

$$f = 0.9999 \qquad \Delta f/f = 0.0001$$

and the taupair loss correction to the additional vertex cut:

$$f = 1.0001 \qquad \Delta f/f = 0.0001,$$

hence the corrections can be seen to be negligible and indeed, cancel each other out. The errors in each case have been taken to be 100% of the observed correction.

Problems can obviously occur if either the vertex finding or the TB chambers are not operating optimally which indeed was found to be the case for a 1993 data run. This will be discussed in chapter 10.1.1.

9.3 Estimation of cosmic ray background in the endcap

Only four cosmic ray/beam gas events in 1992 were found to be rejected by the additional vertex cut on its own in the endcap, however 40 events failed up to two taupair selection cuts including the additional vertex cut. The additional cuts which these events failed included the acolinearity cut, the lower visible energy cut the mupair veto and the $\cos\theta_{\rm avr}$ cut. For taupair events therefore, the additional vertex cut can be seen to be extremely loose, much of the undesirable beam gas and cosmic ray events in the endcap being rejected by the mupair veto and geometry cuts.

Detailed checks showed however that simply extrapolating the event density outside the vertex into the vertex cut underestimated the cosmic ray background as a considerable number of cosmic rays lay inside the vertex. By examining in detail the number of muon chamber segments assigned to tracks, the event acolinearity, visible energy etc. of events lying in the tails of the vertex, 13 cosmic ray events were identified. This number was then corrected for the fraction of the vertex area examined giving a total background of 0.06%. This gave a correction factor of

$$f = 0.9994 \qquad \Delta f/f = 0.0006$$

where the error has conservatively been taken as the full correction. We also conservatively take the four events found outside the vertex as an error for a possible taupair loss giving an acceptance error of 0.02%.

The following chapter summarises the 1992 cross section result together with the 1993 result and the additional checks made possible by combining event samples and the existence of off-peak data.

Chapter 10

Summary and extension to 1993 data

Table 10.2 contains a summary of the correction factors and systematic uncertainties outlined in chapters 6 to 9 for 1992 data. The luminosity corresponding to the selected 1992 data set of 27343 events was 23.913pb^{-1} yielding a peak cross section of:

$$\sigma_\tau = 1.4789 \pm 0.0137 \text{ nb}$$

for the centre of mass energy (91.299 ± 0.018) GeV. The error is the quadrature sum of the data statistics, luminosity statistics, luminosity systematic (including the theory error) and the selection cut systematic errors. The fourth column of table 10.2 attempts to group the uncertainties which make up the total selection cut systematic error into different types. A '$\star$' symbol indicates that the resulting uncertainty was less than 1.5σ away from the expected discrepancy due to statistical fluctuations hence constituting a conservative error. A '$\times$' symbol indicates that the discrepancy seen was greater than 1.5σ away from the expected statistical fluctuation and was of unknown origin. Such a discrepancy was thus deemed a possible source of systematic uncertainty. A '$\bullet$' symbol indicates that the origin of the observed discrepancy has been identified and can therefore be corrected for, the uncertainty here lying in the fact that low statistics limit the accuracy of the correction. A '-' symbol indicates that the associated error is due to Monte Carlo statistics. Where backgrounds were studied using enhancement checks, these errors constitute a contribution to the conservativeness of the associated total systematic error.

In all checks, errors were expanded to account for the finite efficiency in the enhancement procedure, this also contributing to the conservativeness of the final error.

Tables 10.3 and 10.4 show the results for the 1993 pre-scan and scan points and tables 10.5 and 10.6 for the 1993 $\pm 2\,\mathrm{GeV}$ points. It is clear from the tables that many of the associated uncertainties from the individual analyses result from low statistics. It was therefore decided to combine the peak data sets for uncertainties that were mutually less than 1.5σ away from the expected statistical fluctuation in an attempt to reduce the peak cross section uncertainties. By doing this it was also hoped that real effects (of type '$\times$' or '$\bullet$') hidden by low statistics (and hence of type '$\star$') might also start to become visible.

The following section describes the necessary modifications for the 1993 cross section calculation and sections 10.3 to 10.4 summarise the 'combined data set' peak point results, briefly outlining the major sources of uncertainty together with the final quoted cross sections.

10.1 Modifications for 1993 data

10.1.1 The pre-scan

The first four periods of data taking in 1993 were at the peak, having a centre of mass energy equal to $(91.319 \pm 0.005)\,\mathrm{GeV}$. At this time, SiW was unavailable, necessitating an FD measurement of the luminosity. In 1993, no detailed study was carried out upon the FD acceptance/systematic; this meant that the FD luminosity had to be scaled by a factor $f_{\mathrm{SiW|FD}}$ where $f_{\mathrm{SiW|FD}}$ is the ratio of the measured SiW luminosity to the measured FD luminosity for runs in the scan where both FD and SiW were at status 3. The correlation that this introduces between the pre-scan point and the scan-peak point taking into account the relative acceptance of FD and SiW has a correlation coefficient of 0.51, however in light of the fact that the error due to

SiW statistics is negligible for the taupair cross section calculation, the correlation too is negligible.

The scaling factor determined using peak data, peak−2 data and peak+2 data was found to be 1.008 ± 0.003, 1.012 ± 0.003, and 1.013 ± 0.002 respectively, giving a combined result of 1.011 ± 0.001. For each value, the factor was found to be uniform in time over the full 1993 scan with χ^2 values of 1.06, 0.99, and 1.42 respectively. The uncertainty in the pre-scan cross section due to this scaling procedure was thus determined to be 0.14% and was added in quadrature with the other systematic errors.

As the pre-scan luminosity was scaled to the SiW luminosity, the luminosity theory error for the pre-scan is equal to the SiW theory error and is 100% correlated with the scan-peak point uncertainty.

An additional uncertainty of 0.6% was added to the pre-scan cross section to account for the fact that the FD acceptance varies throughout the year due to fluctuations in the energy calibration and movement of the beam spot.

For the 1993 pre-scan, one run (4269) was found where TB was operating inefficiently but still labelled as status 3. This caused a considerable number of taupairs to have no TB hits and hence a corresponding loss to the cosmic ray veto due to poor vertex measurement. This necessitated a correction of $f = 1.0024$, $\Delta f/f = 0.132\%$.

10.1.2 The scan-peak point

The peak point for the 1993 scan was recorded at an energy of 91.208 ± 0.005 GeV and the luminosity was determined using SiW. The cross section error due to luminosity statistics was determined to be 0.14%, the error due to uncertainty in the SiW acceptance determined to be 0.07% and the uncertainty due to the QED theory error on the low angle Bhabha cross section determined to be 0.16%, giving a total luminosity error of 0.23%. Section 10.3.1 describes improvements to the standalone determination of the selection cut systematics and discusses the final cross sections.

10.1.3 Peak+2 and peak−2 points

The Monte Carlo samples used in the determination of the off-peak cross sections at energies of 89.453 GeV and 93.036 GeV are listed in section 5.2.1. The final systematic errors associated with the acceptance correction are 1.26% and 1.22% for the peak+2 and peak−2 points respectively and are larger than for the peak points due to low statistics and the fact that the two samples cannot be combined. Final cross sections are listed in table 10.7 and are in perfect agreement with the preliminary 1993 ALEPH results of 0.499 ± 0.009 nb and 0.705 ± 0.010 nb for the peak−2 and peak+2 points respectively.

The existence of off-peak data collected in 1993 allows a further study to be made upon the non-resonant background resulting from 2-photon electron pair and 2-photon mupair channels this being described in the following section.

10.2 Direct non-resonant background check

As 2-photon background is non-resonant, the existence of off-peak data allows a further check upon its Monte Carlo simulation. The cross section of background 2-photon events should be identical for both off-peak and on-peak data, provided that no significant bias for such events exists at different energy points. Table 10.1 shows the Monte Carlo background cross sections and the background cross sections determined from the enhancement checks described in sections 8.2 and 8.4.

Event sample	$\sigma(e^+e^- \to \gamma\gamma\mu^+\mu^-)$ pb	$\sigma(e^+e^- \to \gamma\gamma e^+e^-)$ pb
MC	1.3 ± 0.2	3.9 ± 0.3
Data (1992)	0.9 ± 0.3	4.0 ± 0.7
Data (1993 pre-scan)	0.6 ± 0.7	1.9 ± 1.2
Data (1993 scan-peak)	0.9 ± 0.6	1.4 ± 0.8
Data (1993 peak+2 GeV)	1.8 ± 0.6	2.9 ± 1.0
Data (1993 peak−2 GeV)	0.6 ± 0.5	2.3 ± 1.1

Table 10.1: Monte Carlo and data cross sections for 2-photon background recorded on and off the Z^0 peak.

Acceptance Corrections (1992)			
$\tau^+\tau^-$ **Selection cut/background**	f	$\Delta f/f$ [%]	$<1.5\sigma$
Bhabha background (raw MC)	0.9985	0.02	-
Barrel $R_{\rm shw}$ cut (ECAL module boundaries)	0.9974	0.06	•
Endcap $R_{\rm shw}$ cut ($R_{\rm trk} < 0.25$)	1.0000	0.01	⋆
Endcap $R_{\rm vis}$ cut ($0.25 < R_{\rm trk} < 0.8$)			
$0.70 < \cos\theta_{\rm avr} < 0.77$	1.0000	0.04	⋆
$0.77 < \cos\theta_{\rm avr} < 0.83$	1.0000	0.00	⋆
$0.83 < \cos\theta_{\rm avr} < 0.90$	1.0000	0.11	×
Endcap $R_{\rm shw}$ cut ($R_{\rm trk} > 0.8$)	1.0000	0.01	⋆
Definition of Barrel edge	1.0000	0.10	⋆
Taupair loss to Bhabha channel (Barrel)	1.0000	0.19	×
Taupair loss to Bhabha channel (Endcap)			
$R_{\rm trk} < 0.25$	1.0000	0.06	×
$0.25 < R_{\rm trk} < 0.80$	1.0000	0.09	⋆
$R_{\rm trk} > 0.80$	1.0000	0.03	⋆
Mupair background (Raw MC)	0.9917	0.02	-
Moderate FSR mupair background	1.0000	0.01	⋆
Hard FSR mupair background	1.0000	0.01	⋆
Mupair tracking failure	0.9980	0.05	•
Misclasification as $\mu^+\mu^-$	1.0000	0.17	×
$q\bar{q}$ background (Raw MC) (JETSET73)	0.9953	0.04	-
$q\bar{q}$ background (syst)	1.0000	0.08	⋆
$N_{\rm trk}$ cut	1.0000	0.11	⋆
$N_{\rm trk} + N_{\rm cls}$ (loss) cut	1.0034	0.04	×
Treatment of conversions	1.0000	0.03	×
Choice of cone angle	1.0000	0.11	×
$e^+e^- \to \gamma\gamma \to e^+e^-$ background(raw MC)	0.9966	0.03	-
$e^+e^- \to \gamma\gamma \to e^+e^-$ background(syst)	1.0000	0.02	⋆
$e^+e^- \to \gamma\gamma \to \mu^+\mu^-$ background(raw MC)	0.9989	0.01	-
$e^+e^- \to \gamma\gamma \to \mu^+\mu^-$ background(syst)	1.0000	0.04	⋆
Acolinearity cut	1.0000	0.05	⋆
Acceptance edge	1.0000	0.17	⋆
Low $R_{\rm vis}$ cut	1.0000	0.00	⋆
TB inefficiency	1.0000	0.00	•
Cosmic ray background (Barrel)	0.9999	0.01	×
Vertex cut (Barrel)	1.0001	0.01	×
Cosmic Ray background (EC)	0.9994	0.06	×
Vertex cut (EC)	1.0000	0.02	×
LLV background	0.9994	0.06	-
Choice of tau branching ratios	1.0000	0.10	×
Trigger efficiency	1.0000	0.01	×
Definition of $\vert\cos\theta\vert$	1.0000	0.07	×
$e^+e^- \to \tau^+\tau^-$ Monte Carlo acceptance	1.3215	0.10	-
Total correction factor	**1.2934**	**0.46**	

Table 10.2: Summary of the stand-alone 1992 peak acceptance corrections and systematic errors. The symbols in column three are explained in section 10.

Acceptance Corrections (1993 pre-scan)			
$\tau^+\tau^-$ **Selection cut/background**	f	$\Delta f/f$ [%]	$<1.5\sigma$
Bhabha background (raw MC)	0.9985	0.02	-
Barrel $R_{\rm shw}$ cut (ECAL module boundaries)	0.9968	0.13	$\bullet$
Endcap $R_{\rm shw}$ cut ($R_{\rm trk} < 0.25$)	1.0000	0.18	$\times$
Endcap $R_{\rm vis}$ cut ($0.25 < R_{\rm trk} < 0.8$)			
$0.70 < \cos\theta_{\rm avr} < 0.77$	1.0000	0.18	$\star$
$0.77 < \cos\theta_{\rm avr} < 0.83$	1.0000	0.04	$\star$
$0.83 < \cos\theta_{\rm avr} < 0.90$	1.0000	0.05	$\star$
Endcap $R_{\rm shw}$ cut ($R_{\rm trk} > 0.8$)	1.0000	0.03	$\star$
Definition of Barrel edge	1.0000	0.16	$\star$
Taupair loss to Bhabha channel (Barrel)	1.0000	0.06	$\star$
Taupair loss to Bhabha channel (Endcap)			
$R_{\rm trk} < 0.25$	1.0000	0.04	$\star$
$0.25 < R_{\rm trk} < 0.80$	1.0000	0.00	$\star$
$R_{\rm trk} > 0.80$	1.0000	0.13	$\star$
Mupair background (Raw MC)	0.9917	0.02	-
Moderate FSR mupair background	1.0000	0.01	$\star$
Hard FSR mupair background	1.0000	0.02	$\star$
Mupair tracking failure	0.9960	0.12	$\bullet$
Misclasification as $\mu^+\mu^-$	1.0000	0.29	$\star$
$q\bar{q}$ background (Raw MC) (JETSET73)	0.9953	0.04	-
$q\bar{q}$ background (syst)	1.0000	0.13	$\star$
$N_{\rm trk}$ cut	1.0000	0.07	$\star$
$N_{\rm trk} + N_{\rm cls}$ (loss) cut	1.0001	0.03	$\star$
Treatment of conversions	1.0000	0.05	$\star$
Choice of cone angle	1.0000	0.02	$\star$
$e^+e^- \to \gamma\gamma \to e^+e^-$ background(raw MC)	0.9966	0.03	-
$e^+e^- \to \gamma\gamma \to e^+e^-$ background(syst)	1.0000	0.18	$\star$
$e^+e^- \to \gamma\gamma \to \mu^+\mu^-$ background(raw MC)	0.9988	0.01	-
$e^+e^- \to \gamma\gamma \to \mu^+\mu^-$ background(syst)	1.0000	0.06	$\star$
Acolinearity cut	1.0000	0.06	$\star$
Acceptance edge	1.0000	0.47	$\star$
Low $R_{\rm vis}$ cut	1.0000	0.17	$\star$
TB inefficiency	1.0024	0.13	$\times$
Cosmic ray background (Barrel)	1.0000	0.00	$\times$
Vertex cut (Barrel)	1.0002	0.02	$\times$
Cosmic Ray background (EC)	0.9998	0.02	$\times$
Vertex cut (EC)	1.0000	0.02	$\times$
LLV background	0.9994	0.06	-
Choice of tau branching ratios	1.0000	0.10	$\times$
Trigger efficiency	1.0000	0.01	$\times$
Definition of $\lvert\cos\theta\rvert$	1.0000	0.13	$\star$
$e^+e^- \to \tau^+\tau^-$ Monte Carlo acceptance	1.3215	0.10	-
Total correction factor	**1.2896**	**0.78**	

Table 10.3: Summary of the stand-alone 1993 pre-scan acceptance corrections and systematic errors. The symbols in column three are explained in section 10.

Acceptance Corrections (1993 scan peak)			
$\tau^+\tau^-$ **Selection cut/background**	f	$\Delta f/f$ [%]	$<1.5\sigma$
Bhabha background (raw MC)	0.9985	0.02	-
Barrel $R_{\rm shw}$ cut (ECAL module boundaries)	0.9952	0.10	$\bullet$
Endcap $R_{\rm shw}$ cut ($R_{\rm trk} < 0.25$)	1.0000	0.11	$\star$
Endcap $R_{\rm vis}$ cut ($0.25 < R_{\rm trk} < 0.8$)			
$0.70 < \cos\theta_{\rm avr} < 0.77$	1.0000	0.08	$\star$
$0.77 < \cos\theta_{\rm avr} < 0.83$	1.0000	0.19	$\times$
$0.83 < \cos\theta_{\rm avr} < 0.90$	1.0000	0.11	$\star$
Endcap $R_{\rm shw}$ cut ($R_{\rm trk} > 0.8$)	1.0000	0.01	$\star$
Definition of Barrel edge	1.0000	0.13	$\star$
Taupair loss to Bhabha channel (Barrel)	1.0000	0.22	$\times$
Taupair loss to Bhabha channel (Endcap)			
$R_{\rm trk} < 0.25$	1.0000	0.02	$\star$
$0.25 < R_{\rm trk} < 0.80$	1.0000	0.17	$\star$
$R_{\rm trk} > 0.80$	1.0000	0.05	$\star$
Mupair background (Raw MC)	0.9917	0.02	-
Moderate FSR mupair background	1.0000	0.14	$\times$
Hard FSR mupair background	1.0000	0.03	$\star$
Mupair tracking failure	0.9996	0.05	$\bullet$
Misclasification as $\mu^+\mu^-$	1.0000	0.12	$\star$
$q\overline{q}$ background (Raw MC) (JETSET73)	0.9953	0.04	-
$q\overline{q}$ background (syst)	1.0023	0.09	$\times$
$N_{\rm trk}$ cut	1.0000	0.05	$\star$
$N_{\rm trk} + N_{\rm cls}$ (loss) cut	1.0037	0.07	$\times$
Treatment of conversions	1.0000	0.02	$\times$
Choice of cone angle	1.0000	0.03	$\star$
$e^+e^- \to \gamma\gamma \to e^+e^-$ background(raw MC)	0.9967	0.03	-
$e^+e^- \to \gamma\gamma \to e^+e^-$ background(syst)	1.0000	0.21	$\times$
$e^+e^- \to \gamma\gamma \to \mu^+\mu^-$ background(raw MC)	0.9989	0.01	-
$e^+e^- \to \gamma\gamma \to \mu^+\mu^-$ background(syst)	1.0000	0.03	$\star$
Acolinearity cut	1.0000	0.04	$\star$
Acceptance edge	1.0000	0.34	$\star$
Low $R_{\rm vis}$ cut	1.0000	0.14	$\star$
TB inefficiency	1.0008	0.06	$\bullet$
Cosmic ray background (Barrel)	1.0000	0.03	$\times$
Vertex cut (Barrel)	1.0001	0.01	$\times$
Cosmic Ray background (EC)	0.9995	0.05	$\times$
Vertex cut (EC)	1.0000	0.04	$\times$
LLV background	0.9994	0.06	-
Choice of tau branching ratios	1.0000	0.10	$\times$
Trigger efficiency	1.0000	0.01	$\times$
Definition of $\lvert\cos\theta\rvert$	1.0000	0.10	$\star$
$e^+e^- \to \tau^+\tau^-$ Monte Carlo acceptance	1.3215	0.10	-
Total correction factor	**1.2974**	**0.68**	

Table 10.4: Summary of the stand-alone 1993 scan-peak acceptance corrections and systematic errors. The symbols in column three are explained in section 10.

Acceptance Corrections (1993 +2 GeV)			
$\tau^+\tau^-$ **Selection cut/background**	f	$\Delta f/f$ [%]	$<1.5\sigma$
Bhabha background (raw MC)	0.9970	0.04	-
Barrel $R_{\rm shw}$ cut (ECAL module boundaries)	1.0000	0.00	$\star$
Endcap $R_{\rm shw}$ cut ($R_{\rm trk} < 0.25$)	1.0000	0.07	$\star$
Endcap $R_{\rm vis}$ cut ($0.25 < R_{\rm trk} < 0.8$)			
$0.70 < \cos\theta_{\rm avr} < 0.77$	1.0000	0.18	$\star$
$0.77 < \cos\theta_{\rm avr} < 0.83$	1.0000	0.06	$\star$
$0.83 < \cos\theta_{\rm avr} < 0.90$	1.0000	0.12	$\star$
Endcap $R_{\rm shw}$ cut ($R_{\rm trk} > 0.8$)	1.0000	0.00	$\star$
Definition of Barrel edge	1.0000	0.41	$\times$
Taupair loss to Bhabha channel (Barrel)	1.0000	0.04	$\times$
Taupair loss to Bhabha channel (Endcap)			
$R_{\rm trk} < 0.25$	1.0000	0.00	$\star$
$0.25 < R_{\rm trk} < 0.80$	1.0000	0.84	$\times$
$R_{\rm trk} > 0.80$	1.0000	0.04	$\star$
Mupair background (Raw MC)	0.9917	0.02	-
Moderate FSR mupair background	1.0000	0.07	$\star$
Hard FSR mupair background	1.0000	0.05	$\star$
Mupair tracking failure	0.9969	0.11	$\bullet$
Misclasification as $\mu^+\mu^-$	1.0000	0.10	$\star$
$q\bar{q}$ background (Raw MC) (JETSET73)	0.9953	0.04	-
$q\bar{q}$ background (syst)	1.0029	0.17	
$N_{\rm trk}$ cut	1.0000	0.45	$\star$
$N_{\rm trk} + N_{\rm cls}$ (loss) cut	1.0045	0.07	$\times$
Treatment of conversions	1.0000	0.02	$\times$
Choice of cone angle	1.0000	0.01	$\star$
$e^+e^- \to \gamma\gamma \to e^+e^-$ background(raw MC)	0.9924	0.06	-
$e^+e^- \to \gamma\gamma \to e^+e^-$ background(syst)	1.0000	0.19	$\star$
$e^+e^- \to \gamma\gamma \to \mu^+\mu^-$ background(raw MC)	0.9974	0.03	-
$e^+e^- \to \gamma\gamma \to \mu^+\mu^-$ background(syst)	1.0000	0.03	$\star$
Acolinearity cut	1.0000	0.08	$\star$
Acceptance edge	1.0000	0.47	$\star$
Low $R_{\rm vis}$ cut	1.0000	0.14	$\star$
TB inefficiency	1.0000	0.00	$\star$
Cosmic ray background (Barrel)	1.0000	0.00	$\times$
Vertex cut (Barrel)	1.0000	0.00	$\times$
Cosmic Ray background (EC)	0.9989	0.06	$\times$
Vertex cut (EC)	1.0000	0.06	$\times$
LLV background	0.9994	0.06	-
Choice of tau branching ratios	1.0000	0.10	$\times$
Trigger efficiency	1.0000	0.01	$\times$
Definition of $\lvert\cos\theta\rvert$	1.0000	0.22	$\times$
$e^+e^- \to \tau^+\tau^-$ Monte Carlo acceptance	1.3305	0.18	-
Total correction factor	**1.2994**	**1.26**	

Table 10.5: Summary of the 1993 +2 GeV point acceptance corrections and systematic errors. The symbols in column three are explained in section 10.

Acceptance Corrections (1993 -2 GeV)			
$\tau^+\tau^-$ **Selection cut/background**	f	$\Delta f/f$ [%]	$<1.5\sigma$
Bhabha background (raw MC)	0.9956	0.06	-
Barrel $R_{\rm shw}$ cut (ECAL module boundaries)	0.9956	0.18	•
Endcap $R_{\rm shw}$ cut ($R_{\rm trk} < 0.25$)	1.0000	0.02	⋆
Endcap $R_{\rm vis}$ cut ($0.25 < R_{\rm trk} < 0.8$)			
$0.70 < \cos\theta_{\rm avr} < 0.77$	1.0000	0.03	⋆
$0.77 < \cos\theta_{\rm avr} < 0.83$	1.0000	0.05	⋆
$0.83 < \cos\theta_{\rm avr} < 0.90$	1.0000	0.16	⋆
Endcap $R_{\rm shw}$ cut ($R_{\rm trk} > 0.8$)	1.0000	0.05	⋆
Definition of Barrel edge	1.0000	0.23	⋆
Taupair loss to Bhabha channel (Barrel)	1.0000	0.23	×
Taupair loss to Bhabha channel (Endcap)			
$R_{\rm trk} < 0.25$	1.0000	0.15	⋆
$0.25 < R_{\rm trk} < 0.80$	1.0000	0.26	×
$R_{\rm trk} > 0.80$	1.0000	0.30	⋆
Mupair background (Raw MC)	0.9917	0.02	-
Moderate FSR mupair background	1.0000	0.08	⋆
Hard FSR mupair background	1.0000	0.01	⋆
Mupair tracking failure	0.9963	0.12	•
Misclasification as $\mu^+\mu^-$	1.0000	0.20	⋆
$q\overline{q}$ background (Raw MC) (JETSET73)	0.9953	0.04	-
$q\overline{q}$ background (syst)	1.0000	0.24	
$N_{\rm trk}$ cut	1.0000	0.16	⋆
$N_{\rm trk} + N_{\rm cls}$ (loss) cut	1.0047	0.18	×
Treatment of conversions	1.0000	0.05	×
Choice of cone angle	1.0000	0.04	⋆
$e^+e^- \to \gamma\gamma \to e^+e^-$ background(raw MC)	0.9899	0.08	-
$e^+e^- \to \gamma\gamma \to e^+e^-$ background(syst)	1.0000	0.42	⋆
$e^+e^- \to \gamma\gamma \to \mu^+\mu^-$ background(raw MC)	0.9966	0.04	-
$e^+e^- \to \gamma\gamma \to \mu^+\mu^-$ background(syst)	1.0000	0.19	⋆
Acolinearity cut	1.0000	0.39	×
Acceptance edge	1.0000	0.22	×
Low $R_{\rm vis}$ cut	1.0000	0.42	⋆
TB inefficiency	1.0000	0.00	⋆
Cosmic ray background (Barrel)	1.0000	0.09	×
Vertex cut (Barrel)	1.0000	0.00	×
Cosmic Ray background (EC)	0.9994	0.06	×
Vertex cut (EC)	1.0000	0.09	×
LLV background	0.9994	0.06	-
Choice of tau branching ratios	1.0000	0.10	×
Trigger efficiency	1.0000	0.01	×
Definition of $\vert\cos\theta\vert$	1.0000	0.56	×
$e^+e^- \to \tau^+\tau^-$ Monte Carlo acceptance	1.3315	0.18	-
Total correction factor	**1.2848**	**1.22**	

Table 10.6: Summary of the 1993 -2 GeV point acceptance corrections and systematic errors. The symbols in column three are explained in section 10.

The 1992 cross sections agree well with the Monte Carlo prediction at the 1.1σ and 0.2σ level for 2-photon mupair and 2-photon electron pair background respectively. Combining the 1993 points produces background cross sections of 1.0 ± 0.3 nb with a χ^2 of 0.9 and 2.0 ± 0.5 nb with a χ^2 of 0.5 for the 2-photon mupair and 2-photon electron pair backgrounds respectively. These values agree at the 0.8σ and 3.2σ level respectively. The 2-photon electron pair background hence seems a little low for the data collected in 1993, however statistics are too low for any correction studies to easily be made. The discrepancy is in any case contained within the systematic checks and contributes a minor fraction to the total error assigned to all points in 1993.

10.3 Summary of final 1992 cross section

The standalone determination of the 1992 selection cut systematic error was reduced from 0.46% to 0.44% by combining the three peak point data sets. The uncertainties contributing to the 1992 measurement alone can be summarised as follows.

Dominant uncertainties which can still be considered conservative were the loss of taupair events to the Bhabha channel contributing 0.19% and loss of events to the mupair channel contributing 0.17% as the observed excesses are highly likely to be due to poorly reconstructed Bhabha and mupair events and not to genuine taupair loss. Their expansion for finite selection efficiency is also believed to add to the conservative nature of the measurement. A small data excess was observed in the Bhabha enhanced endcap sample for events with $0.83 < |\cos\theta_{\rm avr}| < 0.90$, contributing an error of 0.11%. It is believed to be a conservative estimate as it was expanded for the finite selection efficiency.

An error of 0.06% was also assigned to account for the possible loss of taupair events to the $R_{\rm shw} < 0.8$ cut for $R_{\rm trk} < 0.25$ in the endcap. The excess is likely to be due to Bhabha background and thus the error deemed conservative. In any case, it contributes a negligible fraction to the total systematic uncertainty. Excess background due to mupair tracking failure and ECAL module boundary gaps was corrected for, the combined error from the two correction procedures contributing a negligible fraction to the final error. An uncertainty of 0.07% resulted from the method by which the θ axis was reconstructed (resulting from defining the acceptance using clusters alone) which also contributes a negligible amount to the final uncertainty.

Associated errors from sources where discrepancies lay within 1.5σ of the expected statistical fluctuation together with errors due to Monte Carlo statistics where direct background checks were carried out contribute conservatively to 0.15% of the final error. Remaining dominant uncertainties were due to those common between points in the combined analysis.

The final result for the 1992 peak point is:

$$\sigma_\tau = 1.479 \pm 0.009(\mathrm{stat}) \pm 0.007(\mathrm{syst}) \pm 0.008(\mathrm{lumi\ syst})\ \mathrm{nb},$$

giving a final cross section to a precision of $< 1\%$. The 0.463% selection cut systematic error is somewhat larger than the 1992 ALEPH quoted systematic error of 0.3% and considerably less than the 1992 DELPHI and L3 quoted errors of 0.63% and 0.7% respectively [79]. The result agrees excellently with the DELPHI value of:

$$1.491 \pm 0.012(\mathrm{stat}) \pm 0.009(\mathrm{syst})\ \mathrm{nb}\ ,$$

with the ALEPH value of:

$$1.494 \pm 0.015(\mathrm{stat}) \pm 0.007(\mathrm{syst})\ \mathrm{nb}$$

and with the L3 value of:

$$1.472 \pm 0.012(\mathrm{stat}) \pm 0.010(\mathrm{syst})\ \mathrm{nb}\ .$$

The final cross section is also in perfect agreement with the OPAL 1992 determination of the mupair production cross section [80]:

$$\sigma_\mu = 1.4846 \pm 0.008(\mathrm{stat}) \pm 0.003(\mathrm{syst}) \pm 0.008(\mathrm{lumi\ syst})\ \mathrm{nb},$$

demonstrating agreement with the MSM prediction of lepton universality. When combined with the other LEP observables in the lineshape multi-parameter fit, the result is in perfect agreement with the Minimal Standard Model.

10.3.1 Summary of final 1993 cross section

Both the 1993 pre-scan and 1993 scan-peak points benefited significantly from the combined peak point analysis, corresponding systematic errors reducing from 0.78% to 0.46% and from 0.68% to 0.54% respectively. The errors which lay outside 1.5σ of that expected due to statistical fluctuations which were individual to the pre-scan point were as follows.

A 0.18% discrepancy in the endcap for $R_{\rm trk} < 0.25$, a 0.1% uncertainty in the multihadronic background, a 0.13% error associated with the ECAL module boundary Bhabha excess and a 0.12% uncertainty due to an excess of events seen in the mupair channel just above $F_{\rm vis} = 0.16$ (as seen in 1992).

0.21% of the final systematic in the combined peak point analysis for the 1993 pre-scan results from uncertainties which are within 1.5σ of that expected from statistical fluctuations or from Monte Carlo statistics where enhancement checks were carried out, hence contributing to the conservativeness of the measurement. Remaining uncertainties are due to those common with the other points in the combined analysis.

All uncertainties are believed to be conservative in nature as with the 1992 analysis. The resulting cross section is shown in table 10.7 and is in perfect agreement with the 1992 measurement. The final error contains the uncertainty from the FD to SiW scaling factor together with a luminosity systematic error of 0.6% to account for variations in the FD acceptance unchecked in 1993 due to variations in the energy calibration and movement of the beam spot. The SW theoretical error is common with the 1993 scan-peak point error.

Dominant errors due to discrepancies which were in excess of 1.5σ of that expected due to statistical fluctuations individual to the 1993 scan-peak point were a 0.190% discrepancy for the endcap region $0.77 < |\cos\theta_{\rm avr}| < 0.83$ in the tracking energy window $0.25 < R_{\rm trk} < 0.8$, a 0.10% uncertainty resulting from the ECAL module boundary excess correction, an uncertainty of 0.22% resulting from loss to the Bhabha channel as in 1992 which is for the same reason thought to be a conservative estimate, an uncertainty of 0.14% due to an unexplained discrepancy in the mupair background due to moderate final state radiation, a 0.09% error due to uncertainty in the level of multihadronic background and an uncertainty of 0.21% due to an unexplained discrepancy in the level of two photon electron pair background which is believed to be highly conservative due to the efficiency expansion and is most probably a statistical fluctuation.

The final systematic error for the 1993 scan point contains a contribution of 0.17% of the final uncertainty attributed to errors which were within 1.5σ of that expected due to statistical fluctuations or to Monte Carlo statistics where enhancement checks were carried out.

The remaining contributions to the uncertainty were common to the other peak point samples. The final cross section is shown in table 10.7 and is in excellent agreement with the 1992 point, the preliminary ALEPH 1993 numbers of 1.487 ± 0.020 nb and 1.483 ± 0.015 nb for pre-scan and scan peak respectively and the MSM prediction.

Data Period	E_{cm} GeV	σ_τ nb
1992	91.299	1.479 ± 0.009(stat) $\pm$ 0.007(syst) $\pm$ 0.008(lumi syst)
1993 (pre-scan)	91.319	1.483 ± 0.021(stat) $\pm$ 0.007(syst) $\pm$ 0.009(lumi syst)
1993 (scan)	91.208	1.480 ± 0.018(stat) $\pm$ 0.008(syst) $\pm$ 0.003(lumi syst)
1993 +2 GeV	93.036	0.681 ± 0.009(stat) $\pm$ 0.008(syst) $\pm$ 0.001(lumi syst)
1993 −2 GeV	89.453	0.499 ± 0.006(stat) $\pm$ 0.009(syst) $\pm$ 0.001(lumi syst)

Table 10.7: Final cross sections including statistical and systematic errors for the 1992 and 1993 energy points.

Section 10.4 describes the systematic errors common between the energy points and the resulting correlations therefore between the final on and off peak cross sections.

10.4 Dominant common systematic errors

A dominant source of error common to all three peak points is the 0.187% error attributed to the choice of acceptance edge cut. It is however still believed to be conservative as the cut was varied by $\pm 4\sigma$ where σ in itself is a conservative upper bound to the $|\cos\theta_{\rm avr}|$ resolution at the cutting point.

The error of 0.10% common to all three points associated with the choice of tau lepton branching ratios is highly conservative in light of the new tau 3-prong branching ratio studies.

A 0.06% excess in the endcap region $0.70 < |\cos\theta_{\rm avr}| < 0.77$ for the tracking energy window $0.25 < R_{\rm trk} < 0.8$ when combining all three samples is believed to be conservative due to the efficiency expansion and in any case contributes a negligible amount to the final systematic uncertainties.

All other systematics calculated by combining the event samples were within 1.5σ of that expected due to statistics. Together with the background Monte Carlo statistics errors they contribute to the conservativeness of the measurements.

The correlations introduced between the three peak point cross sections due to the combining of event samples for enhancement checks and due to the fact that the same Monte Carlo samples were used throughout are expressed in the correlation matrix in table 10.8. The luminosity theory and acceptance error is 100% correlated between all the 1993 measurements and is common also with all other 1993 LEP cross sections.

σ_τ (run) $\rightarrow$ $\downarrow$	1993 pre-scan	1993 scan-peak	1993 +2	1993 -2
1992 peak	0.42	0.35	0.01	0.01
1993 pre-scan	1.00	0.42	0.01	0.01
1993 scan-peak	-	1.00	0.01	0.01
1993 +2	-	-	1.00	0.00

Table 10.8: Correlation matrix for the 1992 and 1993 cross section selection cut systematic errors.

10.5 Conclusion

We have presented a measurement of the taupair production cross section using 1992 and 1993 LEP data collected at OPAL. All measurements are in complete agreement with the Minimal Standard Model and those values released by the other LEP experiments.

Appendix A

Mupair ID cuts

Mupair background was removed using the LL mupair selection flag. A detailed description of the mupair analysis is given in [66] however for completeness, we briefly describe the mupair selection cuts here.

A.1 Muon track identification

Tracks satisfying the high P_T track quality cuts listed in table 5.3 were identified as muons if they satisfied any one of the following cuts:

- ≥ 2 associated muon chamber hits (MB+ME),
- ≥ 4 associated hadron calorimeter strips with an average number of strip hits per layer of less than 2.0. For $|\cos\theta| < 0.65$ at least one hit is required in the last three layers or
- $P > 15$ GeV provided the sum of all associated electromagnetic clusters did not exceed 3.0 GeV. Clusters were associated if the lay within 63 mrad in azimuth.

A.2 Mupair classification

Mupair events were classed as such if they contained at least two tracks with $|\cos\theta| < 0.95$, that were identified as muons by the cuts listed above and were separated in azimuth by at least 320 mrad. If more than one pair of tracks satisfied these criteria then the pair for which the summed momenta was the greatest were chosen.

To separate mupairs from taupairs consisting of two muonic decays where the muons carry most of the cone energy (the tail of the taupair $R_{\rm trk}$ distribution), the mupair visible energy $F_{\rm vis}$ was required to exceed 60% of the centre of mass energy (hence $F_{\rm vis} \approx R_{\rm vis}$ for mupairs). $F_{\rm vis}$ is defined as the momentum sum of the candidate pair[1] plus the energy of the largest unassociated electromagnetic cluster in the event. Lastly, both tracks were required to have a momentum in excess of 6 GeV.

[1]tracks having their momentum constrained to the beam energy.

Bibliography

[1] I.J.R. Aitcheson and A.J.G. Hey: "Gauge Theories in Particle Physics", 2^{nd} Edition, Adam Hilger, (1989).

[2] F.Abe et al., CDF Collaboration: FERMILAB-PUB-95/022-E.

[3] S.Abachi et al., D0 Collaboration: FERMILAB-PUB-95/028-E.

[4] H.Fritzsch and M. Gell-Mann: Proc. 16^{th} Int. HEP Conf. Chicago (Batavia: National Accelerator Laboratory) (1972) 135.

[5] S.Weinberg: Phys. Rev. Lett. 19, (1967) 1264.

[6] S.Glashow: Nucl. Phys. 22, (1961) 579.

[7] S.Glashow: Phys. Rev. Lett. D2, (1970) 1285.

[8] A.Salam: "Elementary Particle Theory", Ed. N. Svartholm, Almqvist, (1968) 367.

[9] "Review of Particle Properties", Phys. Rev. **D50**, Volume 40 Number 3, (1994) Ch.25.

[10] F.Halzen and A.D.Martin: "Quarks and Leptons: An Introductory Course in Modern Particle Physics", John Wiley & Sons, Inc. (1984) 344.

[11] R.Akers et al., OPAL Collaboration: Z.Phys. **C61**, (1994) 19.

[12] F.Halzen and A.D.Martin: "Quarks and Leptons: An Introductory Course in Modern Particle Physics", John Wiley & Sons, Inc. (1984) 344-354.

[13] R.P.Feynman: "The Theory of Fundamental Processes", Benjamin, (1962) Ch.5.

[14] E.Fermi: Z.Phys. 88, (1934) 161.

[15] "Review of Particle Properties", Phys. Rev. **D50**, Volume 40 Number 3, (1994) Ch.28.

[16] "Review of Particle Properties", Phys. Rev. **D50**, Volume 40 Number 3, (1994) Ch.25.

[17] R.Akers et al., OPAL Collaboration: Z.Phys. **C61** (1994) 19.

[18] The LEP Electroweak Working Group and The LEP Collaborations: CERN-PPE/94-187, (25^{th} November 1994).

[19] M.L.Perl et al.: Phys. Rev. Lett. (1975) 1489.

[20] "Review of Particle Properties", Phys. Rev. **D50**, Volume 40 Number 3, (1994) 1173.

[21] T.N.Truong: Phys. rev. D **30**, (1984) 1509.

[22] A.Schwarz: "Tau Physics", XVI International Symposium on Lepton Photon Interactions, Ithaca, New York, (10-15 August 1993).

[23] Altarelli, Kleiss, Verzegnassi: "Z Physics at LEP I" Volume 1, CERN 89-08, (21^{st} September 1989).

[24] M.Voloshin: TPI-MINN-89/33-T unpublished, (1989).

[25] F.A.Berends and R.Kleiss: Nucl.Phys. **B177**, (1981) 237.

[26] F.A.Berends and A.Böhm: "High Energy Electron-Positron Physics", eds A.Ali and P.Söding (Singapore: World Scientific) (1988) 7.

[27] S.L.Wu: Phys. Rep. **107**, (1984) 59.

[28] W.Rückstuhl: Proc. SLAC Summer Inst. Particle Physics ed P.McDonough (SLAC, Stanford) (1984) 466.

[29] K.K.Gan: Proc. Annual Meeting Div. Particles and Fields ed R.C.Hwa (New York:AIP) (1985) 248.

[30] S.Ozaki: Proc. Int. Symp. Lepton and Photon Interactions at High Energies eds. W.Bartel and R.Rückel (Amsterdam: North Holland) (1987) 3.

[31] K.Abe: Proc. XXV Int. Conf. High Energy Physics eds. K.K.Phua and Y.Yamaguchi (Singapore: World Scientific) (1990).

[32] R.Marshall: RAL-89-012, (May 1989).

[33] B.C.Barish and R.Stroynowski: Phys. Rep. **157** ,(1988) 1.

[34] R.P.Feynman: Phys. Rev. **76**, (1949) 769.

[35] S.D.Drell: Ann. Phys. **4**, (1958) 75.

[36] E.Eichten, K.Lane and M.Peskin: Phys. Rev. Lett., **50**, (1983) 811.

[37] J.Ellis and M.K.Gaillard: CERN 76-18, (1976) 21.

[38] D.H.Perkins: "Introduction to High Energy Physics", 3^{rd} Edition, Addison-Wesley, (1987) 32.

[39] F.Halzen and A.D.Martin: "Quarks and Leptons: An Introductory Course in Modern Particle Physics", John Wiley & Sons, Inc. (1984) 301.

[40] H.burkhardt et al.: Z. Phys. **C43**, (1989) 497.

[41] S.Myers: CERN SL-95-066

[42] K.Ahmet et al., OPAL Collaboration: Nucl. Instr. and Meth. **A305**, (1991) 275-319.

[43] D.Decamp et al., ALEPH Collaboration: Nucl. Instr. and Meth. **A294**, (1990) 121-178.

[44] P.Aarnio et al., DELPHI Collaboration: Nucl. Instr. and Meth. **A303**, (1991)

[45] B.Adeva et al., L3 Collaboration: Nucl. Instr. and Meth. **289**, (1990) 35.

[46] P.P.Allport et al.: Nucl. Instr. and Meth. **A346**, (1994) 476.

[47] J.R.Carter et al.: Nucl. Instr. and Meth. **A286**, (1990) 99.

[48] H.M.Fischer et al.: Nucl. Instr. and Meth. **A283**, (1989) 492.

[49] P.Bock et al.: Nucl. Instr. and Meth. **A314**, (1992) 74.

[50] R.Akers et al.: **A357**, (1995) 253-273.

[51] G.T.J.Arnison et al.: Nucl. Instr. and Meth. **A294**, (1990) 431-438.

[52] B.E.Anderson et al.: CERN/ECP 93-20.

[53] N.Arignon et al.: Nucl. Instr. and Meth. **A313**, (1992) 103-125.

[54] D.Charlton et al.: Nucl. Instr. and Meth. **A325**, (1993) 129-141.

[55] E.H.Vokurka: "Calculating Overall Muon Pair and Tau Pair Trigger Efficiencies at OPAL.", University of Manchester internal note (31^{st} May 1995).

[56] M.Arignon et al.: Nucl. Instr. and Meth. **A333**, (1993) 330-341.

[57] S.Weisz: "The ROPE Primer", OPAL internal note, (1991).

[58] A.Buijs: "The OPAL DST (OD) processor in ROPE", OPAL internal note, (2^{nd} November 1993).

[59] D.Ward and P.Ward: "A GOPAL Primer.", OPAL internal note (August 1993).

[60] S.Giani: "GEANT Detector Description and Simulation Tool", CERN Program Library Long Writeup W5013, (March 1994)

[61] J.F. Kral, R. Van Kooten, P.Wells: "ID Users Guide", OPAL internal note, (13^{th} February 1995).

[62] T.Wyatt et al.: "The LL processor in ROPE", OPAL internal note, (25^{th} March 1992).

[63] M.Sasaki et al.: "The Tau Platform (TP)", OPAL internal note, (11^{th} February 1993).

[64] R.Akers et al., OPAL Collaboration: Z. Phys. **C65** (1995) 47.

[65] J.Allison, Comp. Phys. Comm. 77 (1993) 377-395.

[66] R.Barlow et al.:OPAL Technical Note **TN109**, (23^{rd} July 1992).

[67] P.D.Acton et al., OPAL Collaboration: Z. Phys. **C58** (1993) 219.

[68] R.Akers et al., OPAL Collaboration: OPAL **PN142**, (2^{nd} December 1994).

[69] J.R.Patterson: Proceedings of the XXVII International Conference on High Energy Physics, Glasgow, (20^{th}-27^{th} July 1994) 149.

[70] J.C.Clayton: "Measurement of the Leptonic Branching Ratios of the τ Lepton using the OPAL Detector at LEP.", Ph.D., The University of Birmingham, (January 1995).

[71] Particle Data Group: "Review of Particle Properties", Phys. Rev. **D50**, (1994).

[72] M.Tecchio: OPAL Physics Note **PN158**, (30^{th} June 1994)

[73] B.Barish et al., CLEO II Collaboration: CLEO CONF 94-22, (19^{th} July 1994).

[74] W.Beenakker et al.: Nucl. Phys. **B349** (1991) 323.

[75] P.Routenberg: OPAL Technical Note **TN162**, (20^{th} April 1993).

[76] P.Phillips: "Towards the Ultimate Tight Multiplicity Cut.", University of Manchester internal note (1^{st} June 1993).

[77] K.Hilgart and L.Diberder, Comp. Phys. Comm. **75**:191, (1993).

[78] P.Abreu et al., DELPHI Collaboration: CERN-PPE/94-08, (12^{th} January 1994).

[79] The LEP Electroweak Working Group: CERN-PPE/94-197, (25^{th} November 1994).

[80] R.Akers et al., OPAL Collaboration: Z. Phys. **C61** (1994) 19.

Acknowledgements

"Any man whose errors take 10 years to correct, is quite a man."

J. Robert Oppenheimer

"It wasn't a dark and stormy night. It should have been, but there's the weather for you. For every mad scientist who's had a convenient thunderstorm just on the night his Great Work is complete and lying on the slab, there have been dozens who've sat around aimlessly under the peaceful stars while Igor clocks up the overtime."

Terry Pratchett
& Neil Gaiman, Good Omens

"Nice Guys Finish Last."

Leo Durocher

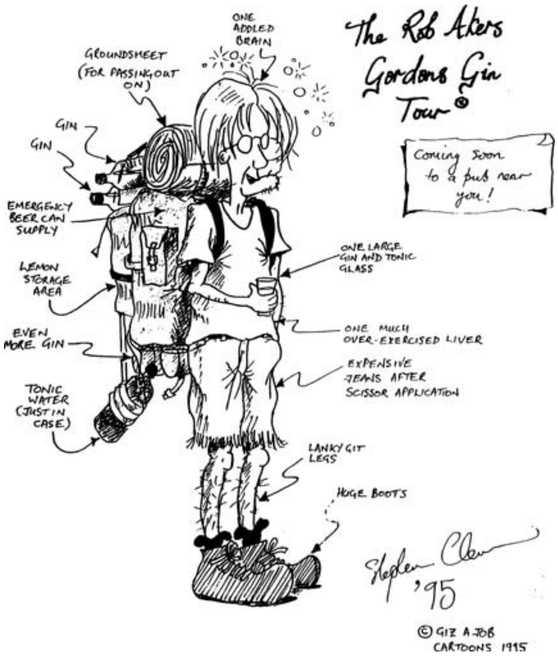

Well here I go, this is my chance to wax lyrical about my life over the last few years, to say how wonderful it's been and to thank all the people who've affected me and made me the bitter and twisted whinging West Midlander that I am. I'm not going to say how wonderful it's been because it hasn't. Some of it was funny, hilarious even. Some of it made me feel like a pig had taken it upon itself to carefully deposit something warm and steaming in my head for safe keeping. But that's the roller coaster ride of life and somehow I'm going to have to learn to love it for all its

ups and downs and not just through amber tinted glasses.

And so, first of all I'd like to thank my Mom for all her love and support. Sometimes it's hard to show how much you care for those closest to you so I'd just like to say that I'd have found the last few years of my life a lot more difficult without your caring advice and wisdom - you're the greatest. Thankyou to my little Bruv Jon too - I don't see much of you these days - I hope that will change in the future. Thanks for all the help with buying a car - I owe you one. Hi to Tracy and all her pandas too.

Next, to the bit where I create some fascinating prose to assassinate the characters of all my friends and colleagues. Sally - without you I'd certainly be a different person - thanks for the happy times, for pushing me into doing a HEP Ph.D. and for growing up with me. I wish you happiness and success in life and hope that one day we'll be best friends again. Matt - what a star. Thanks for being a top drinking partner - and remember, there are worse things in life than having to wear blue plastic shoes. Good luck with the job Nottingham. My drinking partner and house mate, the only West Midlander rock star I know, Stu Barnett. I'd have found it a lot more difficult to get through what I've been through recently without your friendship and support. Let's drink to our future careers, memories of Tequila and Coke bottles and to the pub that rides a horse. Let's hope that our livers don't drop out. Hi to Vad and Colin too. 'Even sillier' Steven Hillier. Errr. What can I say? We've lost touch over the last year or so, separated by distance and by my terrible habit of not being able to keep in touch with people. Thanks for teaching me to ski and more importantly for being a great friend. You helped me through a lot - I'll never forget that. Thanks for all the whisky, for letting me drive your BMW and teaching me that sometimes 'length is important?!?!'. Devans 'no turns, Tory-B' - thanks for all the whisky, for taking me walking and skiing, for not being too upset at awaking to Bob Dylan and your loving skis and for being an excellent friend you old scrote. At some point we're going to have to drink all that wine. Dr. 'Beardy' Lehto - thanks for letting me wear your silly hat. Mark Thompson - a severely missed drinking partner - I'll never forget watching you 'down' that pint of Cardinal - I've never seen anything so disgusting in my life - apart from watching you skid down that ski slope with Steve's crotchless salopettes of course. Thanks for all the help with my Ph.D., for introducing me to Bush beer and for teaching me how to mix a quality G&T. Tara the Chocolate Queen - a great friend and someone to lean on in times of stress and distress - all the best for your future career and have fun in Manchester - I certainly did. Oh no! It's the Birmingham drinking team (or 'Friends of the Syrian Golden Hamster') - we are the **(x)**[1] sad-losers^{TM}, huh, huh, HUH! Most of my memories associated with you lot are somewhat masked by the unusual effect of a certain hydrocarbon. So Jim 'buy us a pint' Clayton, AKA Brassic, the Yorkshire man with the big stick. To memories of 8am beer in Poland, nearly getting run over staring at the Milky Way and sleeping in foreign graveyards. Without you I'd be a healthier person (well, probably not). The Boy Bayes or table dancing, headless superchicken. Keep exericising your liver and keep in touch you bugger. Steve 'condom foot, Welsh trampolining git, oooh look at those beautiful girls' Clewer. Thanks for literally hours of debauched singing and drinking. Thanks for the curries and all the laughs and for being as inept as me at discerning the difference between a G and a G&T. Also, thanks to everyone down the Nelson, Post and anyone in the vicinity of the Pont de Mont Blanc for not thumping/reporting/arresting us. Wam Carling, thanks for being the most reliable hardened drinking partner in the world - good luck with the thesis, marriage and future job hunting. Chris 'pyromaniac, hairbear, baskets' Doddenhof - here's to many an unmemorable 'front-loading' session. Thanks for hours of base entertainment (suits you sir!) and for not burning down Rue de L'Athénée. Keep up the crass humour (suits you sir!), scaffolding scaling and drinking in excess exercises (suits you sir!) you dirty little man. Thanks are also well overdue to Rich 'du-nu-nuuuh, du-nu-nuuuh, nu nu nu nu nuuuh nu nu nuuh nuuuuuu....Ba'....rnes for letting me crash on his floor, for making my ruck-sack smell like a Mexican drug barons den and together with Dr. Doddenhof for showing me some of the more 'interesting?' London sights. I'm looking forward to moving to Oxford and all the imminent future sessions - we're all going to die. Oh yes, a big thankyou to the Egyptians for inventing beer. Christine Beeston - thanks for introducing me to Alpine walking and for being a top boss. Paul 'packed-

[1]insert yourself in **x** if you feel that you are indeed a 'sad-loser^{TM}'

lunch, ice-axe, dancing queen' Phillips - thanks for all the home brew and for being a tolerant house mate. PBT 'International Bright young Thomas', thanks for all the help with my Ph.D., for ski sessions and for being a bit more imaginative than the rest of us when devising things to do. Balj the Dance Queen - thanks for listening to my whinging over the last few years and for not smacking me for spilling baked-beans on your carpet. Anthony 'Okaaay?' Fitzpatrick, thanks for being as stupid as me and for some hilarious memories - thanks for teaching me how to mix a N_2 G&T. Hi to my buds from Durham Group 'J' - Matt, Ali and Jim - it's nice to know that there are people out there who think like myself - let's hope we're all disciplined enough to keep in touch. Thanks to Gareth 'Mr. Shit, QITA' Richards, Colum, Gabbs-MC and Lihp Nosniknah for some rather entertaining memories. Thanks to Jason for his accuracy in targeting my toilet in L'Athénée and not my carpet (I still fail to see how 'Veeeenus' can have that effect on you) - and for those greasy sausage breakfasts. Thanks are also due to Spoony Pearce for lending me his ice-axe. Thanks to Jim 'just the one' Edwards for not being a rude man. Thanks Ronan the Barbarian for inviting me to Bridge & Raclette sessions etc. Stuart 'how's it going' Robertson, thanks for all the sessions down the Guild, for all the unmemorable Baltis in true 'Groundhog day style' and thanks for finishing your Ph.D. after me. Good luck with your job at Cumulus and well done for persuading your bank manager and employer that you do have transferable skills that extend outside of being able to project 10 pints of lager 10 yards at 10 yards per second. I'm glad you chose to work down South with the rest of the sad-losers™. John 'user support' Banks, thanks for the parties and computing help. Cathy Dunwoody, thanks for looking after Plant. Also thanks to Dave 'f-pig' Rigby, Paul 'mushroom' Davies and more recently Mark 'tight-arse' Burton and Pete 'Scouser' Bispham for various head melting sessions of late. So how are we going to manufacture a latex tongue? Also thanks Robert-E-Waugh for the parties etc. Thanks must certainly also be given to Paul Sutton for being a nutter comedian. Andy and Julian, thanks for various 1st year sessions and Alison for feeding me and putting me up in Oxford. Thanks Claire Hessiltine, Rachael Bray and Sto the Stirge for the old times and thanks to Simon Robins for reminding me that not all scientists grow old. Hi to the other 1st years, Beth, Max, Molly, Michael, Gareth, Gareth and Andrew. Hi to Kevin Berwick, Dave and Surrinder - thanks for making my 1st year more bearable. Thanks to Zöe for not playing cello too early in the morning and for all the free Camerata tickets etc. Thankyou Tewy for the old times you old horse. Thanks to Kev Thompson for some pleasant times down the Rampant of late and thanks to Olly Ragg for introducing some 'calmness' in the States. I must say thankyou to Allister Dann for all his help with job applications and amusing anecdotes and to Mango Shaw for being a wonderful friend when I badly needed one. Just make sure you keep in touch. Thankyou Dave Rees for all the help with my Ph.D. - just make sure that Rees Jr. doesn't turn out like Doddenhof, Barnes, Robertson, Clueless or myself. I must say thanks to Paula Collins too for various chats and her recent advice as regards house hunting and to Pete Chang for introducing me to the Chorlton Comedy Club. Stu 'Hotlist' Clowes - keep up the drinking - you know it's good for you. Also, thanks Allan for the odd bit of computer help. A thousand thanks are due to Nigel Watson and Tim Smith - two of the friendliest, most tolerant and most helpful people on OPAL. Without your help I think I'd have had a nervous breakdown. I also owe a huge amount to Matthias Schröder and Guenter Duckeck for their unbelievable tolerance regarding all my **shift -f** problems. Special thanks also to Terry Wyatt for sacrificing large quantities of his time in helping me find my feet out at CERN and to Toshio Tsukamoto and Monica Tecchio for replying to my obscure E-mails. Thanks Fred for being a quality friend and supervisor, thanks Roger Barlow, George, Roger 'Mexican' Jones and the rest of the OPAL group for all their physics help and tolerance, and to the rest of the Manchester group and the SERC/EPSRC for letting me spend what I can say have been a most 'interesting' three or so years.

Lastly, I'd like to say thankyou Susanne for giving me a reason to return from Genève and for a beautiful year....one that I'll never forget and for some memories that I will treasure until the day I pop my Docs. I'll always be thinking of you and I'll always be here for you if you ever need a friend. Take care of yourself and good luck with your Ph.D.

There are lots of other people I can thank but I don't want to dredge up the past too much as I think it's time to move on. You know who you all are and you'll

probably never read this anyway - thanks and good luck for the future.

Rob, July 1995

rob@h2.ph.man.ac.uk

rob.akers@aea.orgn.uk

http://h2.ph.man.ac.uk/~rob/home.html